THE EFFECTS OF ANNULAR AND CONICAL INHOMOGENEITIES UPON THE CENTRAL-AXIS SCATTER DOSE IN A COBALT 60 PHOTON BEAM

by

BRIAN JAMES McPARLAND

B.A.Sc., University of British Columbia, 1979

A THESIS SUBMITTED IN PARTIAL FULFILMENT OF THE REQUIREMENTS FOR THE DEGREE OF MASTER OF SCIENCE

in

THE FACULTY OF GRADUATE STUDIES

Department of Physics

We accept this thesis as conforming to the required standard

THE UNIVERSITY OF BRITISH COLUMBIA

August, 1981

In presenting this thesis in partial fulfilment of the requirements for an advanced degree at the University of British Columbia, I agree that the Library shall make it freely available for reference and study. I further agree that permission for extensive copying of this thesis for scholarly purposes may be granted by the head of my department or by his or her representatives. It is understood that copying or publication of this thesis for financial gain shall not be allowed without my written permission.

Department of Physics

The University of British Columbia
2075 Wesbrook Place
Vancouver, Canada
V6T 1W5

Date Sept. 9, 1981

Abstract

Tissue inhomogeneities can significantly alter the radiation dose delivered to a tumor. In the past, the accuracy of dose calculations has been limited by a lack of precise knowledge of the inhomogeneities within the patient's anatomy. Such anatomical information is now available in much greater detail due to the widespread use of computed tomography (CT) in radiotherapy treatment planning. Consequently, the potential for more accurate dosimetry has grown. The difficulty now resides in being able to efficiently handle this CT data.

The effect of an inhomogeneity upon the primary dose is well known. That upon the scatter is not. Therefore, we have limited our study to that of the alteration in the scatter dose. The perturbation is a complicated function of the density and position of the inhomogeneity, information which is available from CT data.

A method, known as the differential Batho method, has been developed to estimate the scatter dose change. It provides a calculation of the effects due to an inhomogeneity in the shape of an annulus, or a cone's frustum, concentric about the central axis. This method allows the effects of multiple inhomogeneities to be estimated.

Several series of experiments were performed to measure the effects of such inhomogeneities, in a ^{60}Co beam, as functions of density and geometry. It was found that for many of the geometries tested, the differential Batho method gave a good account of the changes measured. The deviations that occurred were readily accounted for.

The differential Batho method provides a good measure of the scatter effects for simple symmetric geometries. In this thesis, it is recommended that further studies be made with phantoms simulating the human anatomy to test the method for specific treatment techniques.

Table of Contents

Abstract....ii
List of Tables....vii
List of Figures....viii
Acknowledgements....xii
1 INTRODUCTION....1
2 THEORY....4
2.1 Effects of inhomogeneities upon the photon fluence....4
2.1.1 Definition of primary and scatter components....4
2.1.2 Relative importance of the scatter component....6
2.1.3 Effects of an inhomogeneity upon the primary component....8
2.1.4 Effects of an inhomogeneity upon the scatter component....8
2.2 Correction schemes....12
2.2.1 Homogeneous medium with $\rho \neq 1$....12
2.2.2 Semi-infinite slab inhomogeneity normal to the beam axis....13
2.2.3 General geometries....16
2.2.3.1 Differential scatter-air ratio method....17
2.2.3.2 Equivalent tissue-air ratio method....19
2.3 Inhomogeneity in the form of an annulus or a cone....21
2.3.1 Differential Batho method....24
2.3.2 van de Geijn-PoCheng method....25

3 APPARATUS AND EXPERIMENTAL PROCEDURES.....27

3.1 Apparatus.....27

3.2 Measurement methods.....32

3.2.1 Method A.....32

3.2.2 Method B.....33

3.3 Sources of error.....38

3.3.1 Annulus experiments.....38

3.3.2 Cone experiments.....38

3.4 Experiment procedures.....40

3.4.1 Annulus experiments.....40

3.4.1.1 Field size slightly smaller than the annulus.....40

3.4.1.2 Field size larger than the annulus.....41

3.4.1.3 Variable field size.....41

3.4.2 Cone experiments.....42

3.4.2.1 Corrections for conical inhomogeneity experiments 43

4 RESULTS AND DISCUSSION.....47

4.1 Results from annulus experiments.....47

4.1.1 Field size slightly smaller than the annulus.....47

4.1.2 Field size slightly larger than the annulus.....47

4.1.3 Variable field size.....53

4.1.4 Discussion of annulus experiments.....53

4.1.4.1 Dependence of scatter changes upon density and depth.....53

4.1.4.2 Dependence of scatter changes upon field size.....54

4.2 Results from cone experiments.....57

4.2.1 Discussion of cone experiments.....62

4.2.1.1 Differential Batho method calculations.....76

4.2.1.2 van de Geijn-PoCheng calculations.....86

4.3 Further considerations.....90

5 CONCLUSIONS.....94

References.....96

Appendix A.....100

Appendix B.....111

Appendix C.....119

List of Tables

I ANNULUS EXPERIMENT PARAMETERS I.....41

II ANNULUS EXPERIMENT PARAMETERS II.....42

III ANNULUS EXPERIMENT PARAMETERS III.....43

IV PERCENTAGE DOSE CHANGE DUE TO CONE APPARATUS.....45

V INHOMOGENEITIES.....46

VIa PERCENTAGE DOSE CHANGE (SMOOTHED) @ 5 CM.....60

VIb PERCENTAGE DOSE CHANGE (SMOOTHED) @ 8 CM.....60

VIc PERCENTAGE DOSE CHANGE (SMOOTHED) @ 10 CM.....61

VId PERCENTAGE DOSE CHANGE (SMOOTHED) @ 15 CM.....61

VIe PERCENTAGE DOSE CHANGE (SMOOTHED) @ 20 CM.....62

VIIa RATIO OF CORRECTION FACTORS FOR INCREASING OUTER CONE DENSITY.....64

VIIb RATIO OF CORRECTION FACTORS FOR INCREASING INNER CONE DENSITY.....65

VIIc RATIO OF CORRECTION FACTORS FOR DECREASING OUTER CONE DENSITY.....66

VIId RATIO OF CORRECTION FACTORS FOR DECREASING INNER CONE DENSITY.....67

VIII COMPARISON OF ADDED EFFECTS TO NET EFFECT.....72

List of Figures

1 PRIMARY AND SCATTERED PHOTONS.....5

2 MONTE CARLO SIMULATION OF THE BEAM COMPONENTS OF A ^{60}Co FIELD 10 cm IN DIAMETER @ 90 cm SSD.....7

3 INHOMOGENEITY AFFECTING ONLY PRIMARY DOSE.....9

4 INHOMOGENEITY AFFECTING ONLY SCATTER DOSE.....9

5a EFFECTS OF MULTIPLE INHOMOGENEITIES I.....11

5b EFFECTS OF MULITPLE INHOMOGENEITIES II.....11

6a HOMOGENEOUS MEDIUM WITH $\rho \neq 1$.....14

6b EQUIVALENT UNIT-DENSITY MEDIUM.....14

7 SEMI-INFINITE INHOMOGENEOUS SLAB EXTENDING ACROSS THE FIELD.....15

8 IRREGULAR INHOMOGENEITY AFFECTING ONLY SCATTER DOSE.....18

9 ANNULAR INHOMOGENEITY.....23

10 PERSPEX CONE STRUCTURE.....29

11 CONE EXPERIMENT APPARATUS.....31

12 SAMPLE DIFFERENTIAL SIGNAL.....34

13a RECORDED NOISE SIGNAL FROM CHAMBER EXPOSED TO ^{60}Co SOURCE.....35

13b RECORDED ELECTRONICS NOISE.....35

14a PERCENTAGE DOSE CHANGE VS. DISTANCE FOR FIELD SLIGHTLY SMALLER THAN THE ANNULUS (ρ = 0.352).....48

14b PERCENTAGE DOSE CHANGE VS. DISTANCE FOR FIELD SLIGHTLY SMALLER THAN THE ANNULUS (ρ = 2.33).....49

15a PERCENTAGE DOSE CHANGE VS. DISTANCE FOR FIELD LARGER THAN THE ANNULUS (ρ = 0.352).....50

15b PERCENTAGE DOSE CHANGE VS. DISTANCE FOR FIELD LARGER THAN THE ANNULUS (ρ = 2.33).....51

16 PERCENTAGE DOSE CHANGE VS. EQUIVALENT FIELD RADIUS (ρ = 0.028).....52

17a PERCENTAGE DOSE CHANGE VS. INNER CONE DENSITY.....58

17b PERCENTAGE DOSE CHANGE VS. OUTER CONE DENSITY.....59

18a COMPARISON OF SUMMED AND NET EFFECTS FOR $\rho_{in} = \rho_{out} = 0$.....69

18b COMPARISON OF SUMMED AND NET EFFECTS FOR $\rho_{in} = \rho_{out} = 1.58$.....70

18c COMPARISON OF SUMMED AND NET EFFECTS FOR $\rho_{in} = 0$ AND $\rho_{out} = 1.58$.....71

19 MULTIPLE INHOMOGENEITIES VARYING RADIALLY.....75

20a dBM AND MEASURED RESULTS ($\rho_{in}=0, \rho_{out}=1$).....78

20b dBM AND MEASURED RESULTS ($\rho_{in}=1, \rho_{out}=0$).....78

20c dBM AND MEASURED RESULTS ($\rho_{in}=\rho_{out}=0$).....79

20d dBM AND MEASURED RESULTS ($\rho_{in}=1, \rho_{out}=0.86$).....79

20e dBM AND MEASURED RESULTS (ρ_{in}=0.86,ρ_{out}=1).....80

20f dBM AND MEASURED RESULTS (ρ_{in}=ρ_{out}=0.86).....80

20g dBM AND MEASURED RESULTS (ρ_{in}=1,ρ_{out}=1.58).....81

20h dBM AND MEASURED RESULTS (ρ_{in}=1.58,ρ_{out}=1).....81

20i dBM AND MEASURED RESULTS (ρ_{in}=ρ_{out}=1.58).....82

20j dBM AND MEASURED RESULTS (ρ_{in}=0,ρ_{out}=0.86).....82

20k dBM AND MEASURED RESULTS (ρ_{in}=0.86,ρ_{out}=0).....83

20l dBM AND MEASURED RESULTS (ρ_{in}=0,ρ_{out}=1.58).....83

20m dBM AND MEASURED RESULTS (ρ_{in}=1.58,ρ_{out}=0).....84

20n dBM AND MEASURED RESULTS (ρ_{in}=0.86,ρ_{out}=1.58).....84

20o dBM AND MEASURED RESULTS (ρ_{in}=1.58,ρ_{out}=0.86).....85

21a COMPARISON OF dBM AND VAN DE GEIJN-PoCHENG CALCULATIONS WITH MEASUREMENTS FOR ρ = 0.86.....88

21b COMPARISON OF dBM AND VAN DE GEIJN-PoCHENG CALCULATIONS WITH MEASUREMENTS FOR ρ = 1.58.....89

22 APPROXIMATION OF A LUNG INHOMOGENEITY BY A CONICAL SEGMENT.....91

A-1 PHOTON TRAJECTORY CROSSING THE INTERFACE BETWEEN TWO MEDIA.....104

B-1 SEMI-INFINITE SLAB INHOMOGENEITY OF WIDTH r_i.....112

B-2 SEMI-INFINITE SLAB INHOMOGENEITY OF WIDTH r_o.....114

B-3 ANNULAR INHOMOGENEITY AT PHANTOM SURFACE.....117

C-1 CROSS SECTION OF A THIN CONICAL INHOMOGENEITY.....120

C-2 SLAB INHOMOGENEITY COVERING PART OF THE FIELD.....126

C-3 UNIT-DENSITY CONICAL INHOMOGENEITY IN

A NON-UNIT DENSITY MEDIUM.....127

Acknowledgements

I would like to thank Dr. E.G. Auld and Dr. L.D. Skarsgard for acting as members of my supervisory committee. During my two year stay, the staff of the Physics Department at the A. Maxwell Evans Clinic provided an enjoyable atmosphere to work in. In particular, I am grateful for the assistance of Dr. K. Yuen during the formative stages of this project, and to Mr. C. Potter for making much of the apparatus used in the experiments.

Most of the figures for this thesis were prepared with the assistance of the Medical Illustrations Department at the Clinic. The expert help and advice of that department's staff is greatly appreciated.

The financial support of the B.C. Cancer Foundation, through Mrs. Jean Sweeney, is gratefully acknowledged. I would also like to express my appreciation to the A. Maxwell Evans Clinic and the B.C. Cancer Research Centre for permitting me to use their equipment for the project.

Finally, I would like to thank Dr. R.O. Kornelsen, head physicist at the A. Maxwell Evans Clinic. As my thesis supervisor, he has provided the academic, and practical, advice and assistance required to ensure the successful completion of this project.

Brian J. McParland,

Vancouver, August, 1981

1 INTRODUCTION

The object of radiotherapy is to deliver a prescribed radiation dose to a tumor while minimizing the dose to surrounding normal tissue. A small change in the dose delivered to the tumor-containing volume may increase or decrease local control. Correspondingly, errors in the amount and placement of the radiation may result in failure of that control and unacceptable damage of uninvolved tissue. For example, a decrease as small as 10 % of the nominal dose can reduce the control probability of a supraglottic carcinoma by a factor of 7 [ICRU, 1976].

On the basis of radiobiological and clinical studies, the International Commission on Radiation Units and Measurements (ICRU) has recommended a need for a ± 5 % accuracy in delivery of the tumor dose. Uncertainties in the prescribed dose delivered are due to errors in the therapy machine calibration, the treatment planning algorithm, the placement of the patient and anatomical movements such as breathing. Loevinger and Loftus [ICRU, 1976] have calculated the minimum uncertainty in the machine calibration to be ± 2.5 %. Hence, for a ± 5 % accuracy in dose delivery to be achieved, errors in the treatment planning must be well below ± 2.5 %. Such precision implies the use of computed tomography (CT) [Geise and McCullough, 1977; Goitein, 1979; Stewart, et. al., 1978].

As the body is composed primarily of water, dose calculations have conventionally assumed it to be entirely water. Correction factors are then applied to account for the effects of anatomical inhomogeneities, such as lung and bone, upon the dose.

At ^{60}Co photon energies (1.17 and 1.33 MeV), the predominant photon-electron interaction is the Compton scattering process. Compton scatter is independent of the medium's atomic composition, but rather is a function of only the electron density ρ_e ,

$$\rho_e = (ZN/A)\ \rho_p$$

where Z is the atomic number, A is the atomic mass, N is Avogadro's number and ρ_p is the physical density . Hence, the ^{60}Co dosimetry for most tissue can neglect the atomic composition and consider only the electron density. For the remainder of the thesis, the medium's electron density relative to water will be called the 'relative electron density' and denoted by ρ.

In the body, the two major tissues with an electron density substantially different from that of water are lung and bone. The relative electron density of lung is in the range of 0.15 to 0.4 and that of bone is about 1.4 [Battista, et. al., 1980; van Dyk, et. al., 1980]. Such densities will greatly perturb the radiation dose. The relative fluence of the primary photons (photons that have not been scattered) through lung will increase whereas that through bone will decrease. The generation of scatter in lung is 0.15 to 0.4 of that in water-equivalent soft tissue, increasing to 1.4 in bone. To correct for the effects of these

inhomogeneities upon the dose, information about their electron densities and their location within the body must be available. The CT scanner provides this information in a form suited to computation.

Because an inhomogeneity affects primary and scattered photons quite differently, it will be useful to consider these effects separately. The perturbation of the primary is simple whereas that of the scatter is a complicated function of electron density and geometry. Hence, the density and anatomical information from a CT scan must be combined with a treatment planning algorithm that can accurately calculate the individual effects.

Commercially available since only 1972, the CT scanner generates a cross section of a patient from a multitude of X-ray transmission measurements in the form of a density matrix [Brooks and Di Chiro, 1976; Cormack, 1980; Hounsfield, 1980]. The two major radiotherapeutically useful features of a CT scan are a visualization of the internal anatomy without magnification, distortion or superposition, and numerical data from which tissue electron densities can be estimated [McCullough, 1975].

The success of the radiation treatment is dependent upon the dosimetry's accuracy which, in turn, is dependent upon the anatomical information available. Since the advent of CT, detailed anatomical knowledge has increased dramatically. With this information now available, the problem resides in how to use it to efficiently calculate patient doses. This is the problem examined by this thesis.

2 THEORY

2.1 Effects of inhomogeneities upon the photon fluence

A radiation beam is composed of primary and scatter components. An inhomogeneity affects these two components differently. The effect upon the primary is simple, whereas that upon the scatter component is complicated and not so well-understood. This subsection will examine these effects.

2.1.1 Definition of primary and scatter components

Consider figure (1). The point source at 'S' is irradiating a unit density medium and it is assumed that the sole interaction is Compton. A photon from the source can reach the central axis point 'P' along an infinite number of paths. A primary photon is one which travels along the trajectory SP - i.e., it does not interact with anything until it reaches 'P'. The photon travelling along SAP is scattered once and is defined as a first-order scatter photon. The photon which takes the route SBCP is called a second-order scatter photon, and so on for the higher orders.

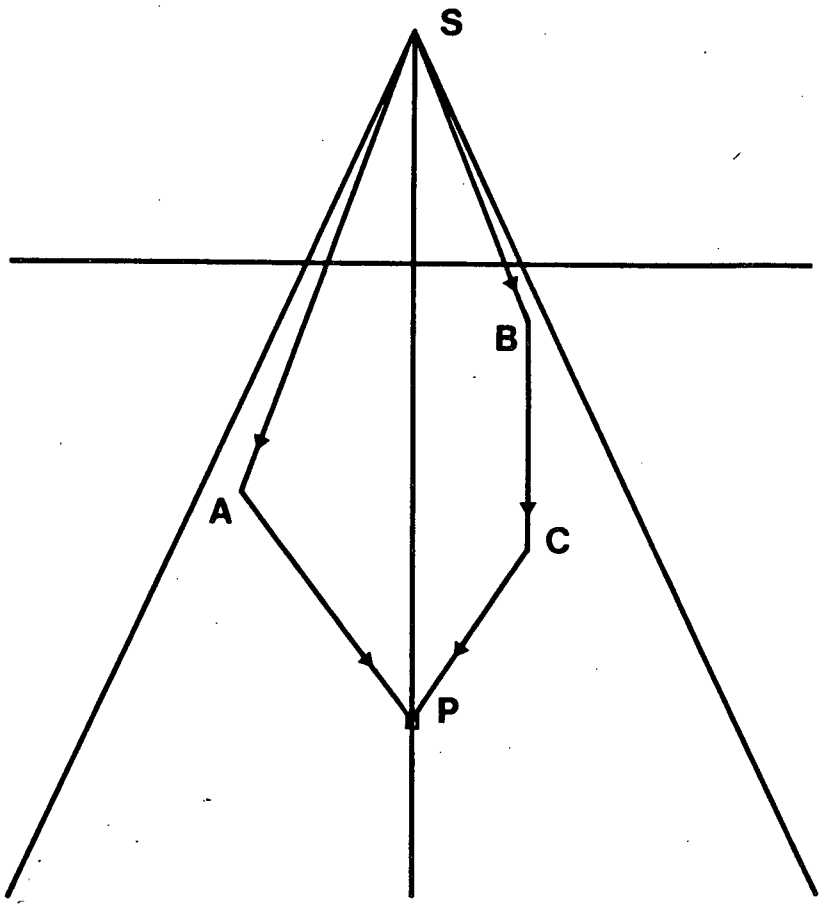

FIGURE 1

PRIMARY AND SCATTERED PHOTONS

2.1.2 Relative importance of the scatter component

Before describing the effects of inhomogeneities upon the dose, it is important to determine how much the scatter dose contributes to the total dose. The scatter component can be measured [Clarkson, 1941; Cunningham, 1972]. A beam of zero radius is composed of only primary radiation. By measuring the dose in fields of varying sizes, one can extrapolate the results to zero radius to yield the primary component. The scatter will be the difference between this component and the total. However, this method will find only the total scatter and not its sub-components.

These sub-components can be separated using analytical techniques [Berger and Spencer, 1959; Roesch, 1968; Wong, et.al., 1981a]. These methods calculate individual scatter components up to, at best, second-order. Beyond this order, the equations to be solved become unmanageable. In practice, Monte Carlo (stochastic) simulations are necessary to determine the higher orders of scatter.

For this thesis, we have developed a Monte Carlo routine, HMONTE, to calculate the kerma* due to the various radiation components along the central axis of a water phantom exposed to ^{60}Co photons. This routine is described in detail in Appendix A. For ^{60}Co photon energies, the kerma is very nearly equal to the absorbed dose at most points of practical interest [Batho, 1968].

* - Kerma is the radiological quantity defined as the total kinetic energy of the secondary particles released, per unit mass, by indirectly ionizing radiation [ICRU, 1980].

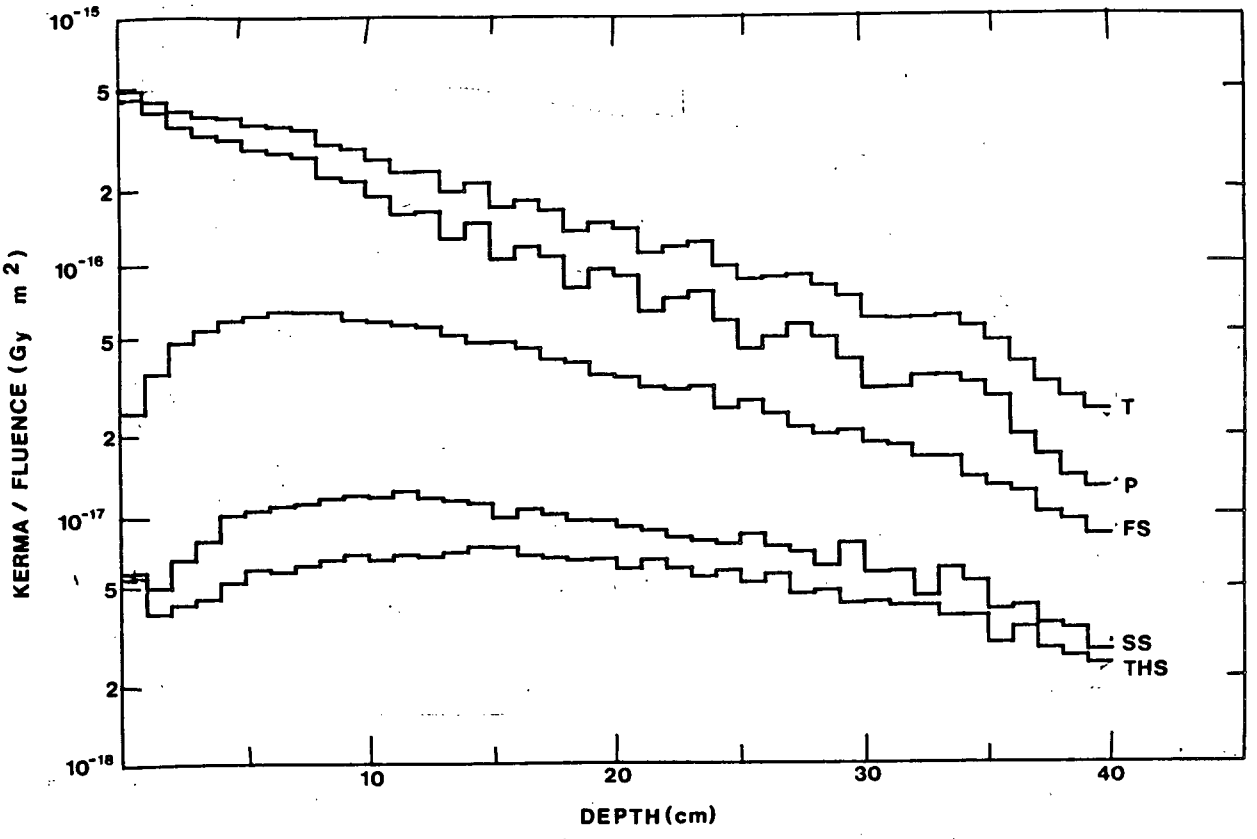

FIGURE 2

MONTE CARLO SIMULATION OF THE BEAM COMPONENTS
OF A ^{60}Co FIELD 10 CM IN DIAMETER @ 90 CM SSD
(10^7 PHOTON SIMULATION)

(T : TOTAL, P : PRIMARY, FS : FIRST SCATTER,
SS : SECOND SCATTER, THS : THIRD AND HIGHER SCATTER)

Figure (2) shows the beam components for a 10 cm diameter field at a source-surface distance (SSD) of 90 cm. The kerma normalized to the unit surface fluence is plotted against depth. It is apparent that the scatter is a significant contributor to the radiation dose. At a 10 cm depth, the net scatter amounts to 27 % of the total, emphasizing the need to take account of the scatter in correcting for inhomogeneities.

2.1.3 Effects of an inhomogeneity upon the primary component

The introduction of an inhomogeneity into the medium will alter the photon fluence reaching 'P' in a variety of ways. In a homogeneous unit density medium, the primary fluence is attenuated exponentially as $e^{-\mu x}$, where 'μ' is the linear attenuation coefficient in water and 'x' is the depth of 'P'. If an inhomogeneity were to be placed, as in figure (3), along the central axis so as to affect only the primary photons, the attenuation factor for the primary will be,

$$e^{-\mu a}\, e^{-\mu \rho b}\, e^{-\mu c} = e^{-\mu(a + \rho b + c)}$$

where 'ρ' is the relative electron density of the inhomogeneity. Thus the correction factor for the primary is simply another exponential.

2.1.4 Effects of an inhomogeneity upon the scatter component

The effects of an inhomogeneity upon the scatter are much more

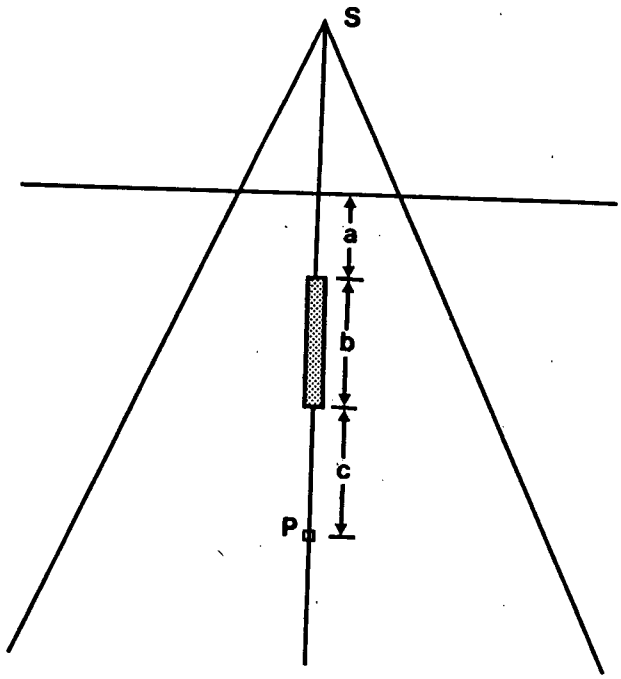

FIGURE 3

INHOMOGENEITY AFFECTING ONLY PRIMARY DOSE

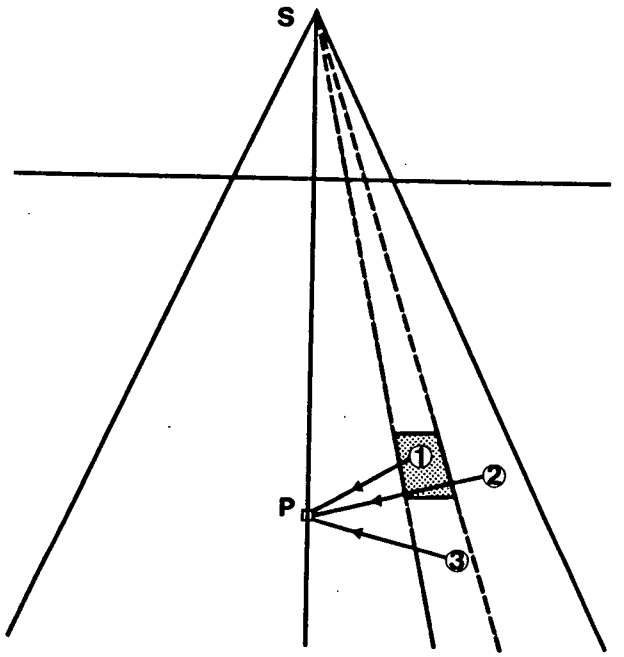

FIGURE 4

INHOMOGENEITY AFFECTING ONLY SCATTER DOSE

complicated than those for the primary. Consider the geometry of figure (4) where the inhomogeneity is off-axis and assume that its relative electron density is less than one. The primary photons reaching 'P' are unaffected. However, there are three competing effects that will alter the scattered photon fluence at 'P' :

(1) there is reduced scatter from the volume containing the inhomogeneity due to the reduction in the number of scattering centers within that volume;

(2) the transmission of scatter originating from beyond the inhomogeneity will be increased because of the lower density material within the volume; and

(3) the primary reaching points beyond the inhomogeneity will increase due to the decreased attenuation. Consequently, there will be an increase in scatter from this region reaching 'P'.

The opposite of these three results will occur for a density greater than unity. In either case, the competing effects may lead to an increase, a decrease or no change at all in the scattered photon fluence reaching 'P'.

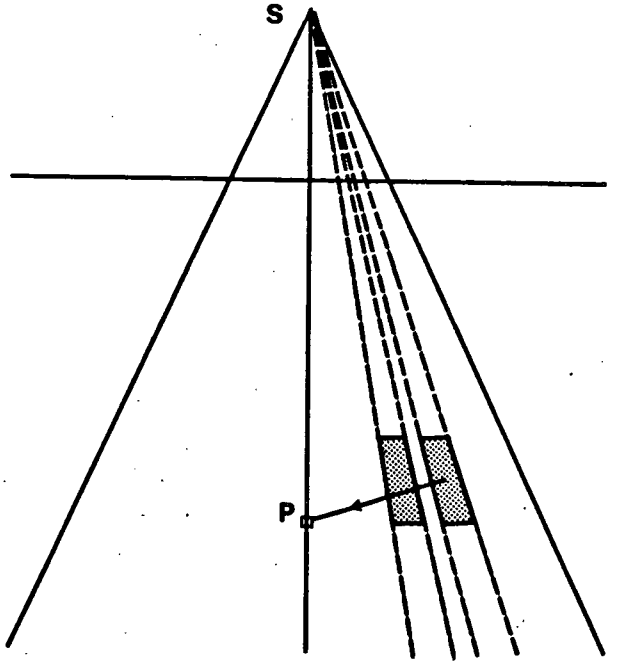

FIGURE 5a

EFFECTS OF MULTIPLE INHOMOGENEITIES I

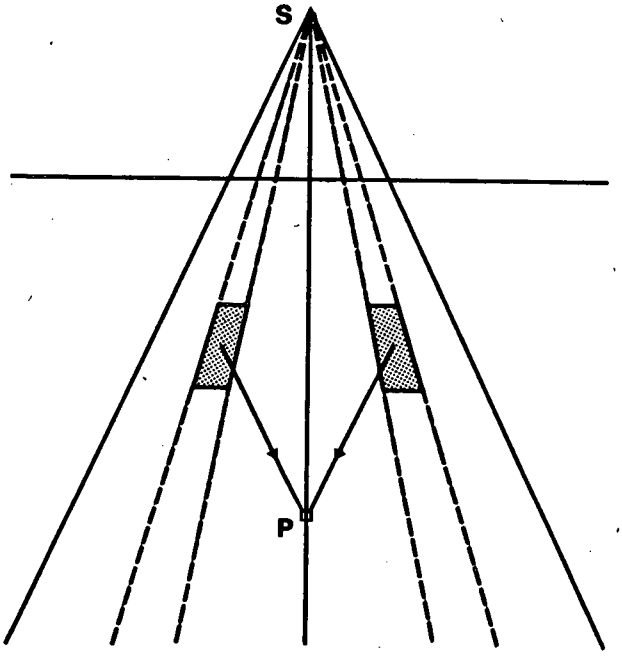

FIGURE 5b

EFFECTS OF MULTIPLE INHOMOGENEITIES II

A critical point to note is that the inhomogeneity's effect upon the scatter is neither additive nor independent. In general, the perturbation due to two inhomogeneities is not equal to the sum of the individual effects. For example, in figure (5a), the net effect is not equal to the sum of the individual effects as the scatter from the inhomogeneity furthest from 'P' is filtered by the nearest. In figure (5b), the net effect, to a first-order scatter approximation, is equal to the sum. Beyond firstorder, though, the effects are not additive.

2.2 Correction schemes

A number of correction schemes have been developed to give good approximations for particular geometries. These will be reviewed in this section.

It would be useful to introduce the concept of the tissue-air ratio at this time. The tissue-air ratio is the ratio of the dose at a point in tissue to the dose at the same point, in air, within a phantom just large enough to ensure maximum buildup [ICRU, 1973].

2.2.1 Homogeneous medium with $\rho \neq 1$

To correct for the effects of non-unit density materials upon the dose, the first approach would be to examine the problem of the homogeneous medium with $\rho \neq 1$. O'Connor [1957] published a method to calculate the dose at a point for such a case. Assume that the Compton

process is predominant and consider figure (6a).

O'Connor showed that the tissue-air ratio at a point in the phantom will be the same as that in a water phantom with all of the linear dimensions scaled by 'ρ', as in figure (6b). Johns, et. al. [1958], showed that, for ^{60}Co photon energies, the tissue-air ratio is independent of the source-axis distance (SAD) between the SAD values of 40 cm and 100 cm. Consequently, the SAD need not be scaled by ρ. The ratio of the scatter to primary fluences at a point in both phantoms will also be the same. Such a linear relationship between the density and the dimensions is strictly true only for a homogeneous medium but it does give an idea of the effect of density upon scatter.

O'Connor's method, by itself, is insufficient for direct clinical use. However, it can be combined with other methods in phantoms with more complicated geometries. An example is given in Appendix C.2.

2.2.2 Semi-infinite slab inhomogeneity normal to the beam axis

Batho [1964] proposed a semi-empirical method to correct for the effect of a semi-infinite slab placed across the radiation field.

Consider the geometry of figure (7) and assume that Compton scatter is predominant. If D_h is the dose at 'P' in the homogeneous medium and D_i is the dose for the inhomogeneous case, the correction

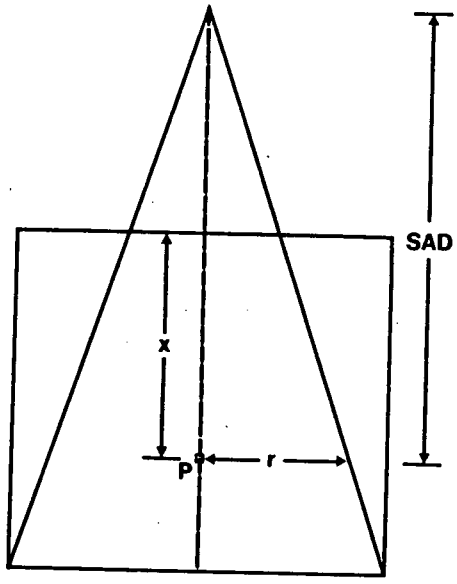

FIGURE 6a

HOMOGENEOUS MEDIUM WITH $\rho \neq 1$

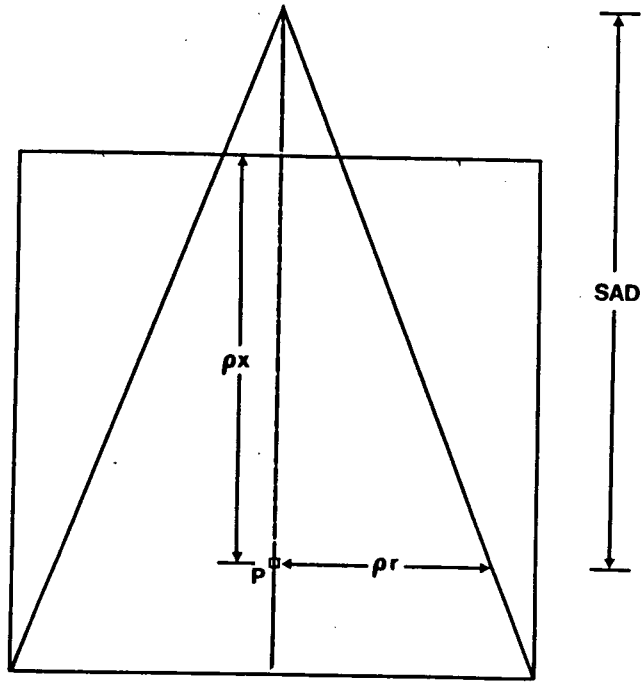

FIGURE 6b

EQUIVALENT UNIT-DENSITY MEDIUM

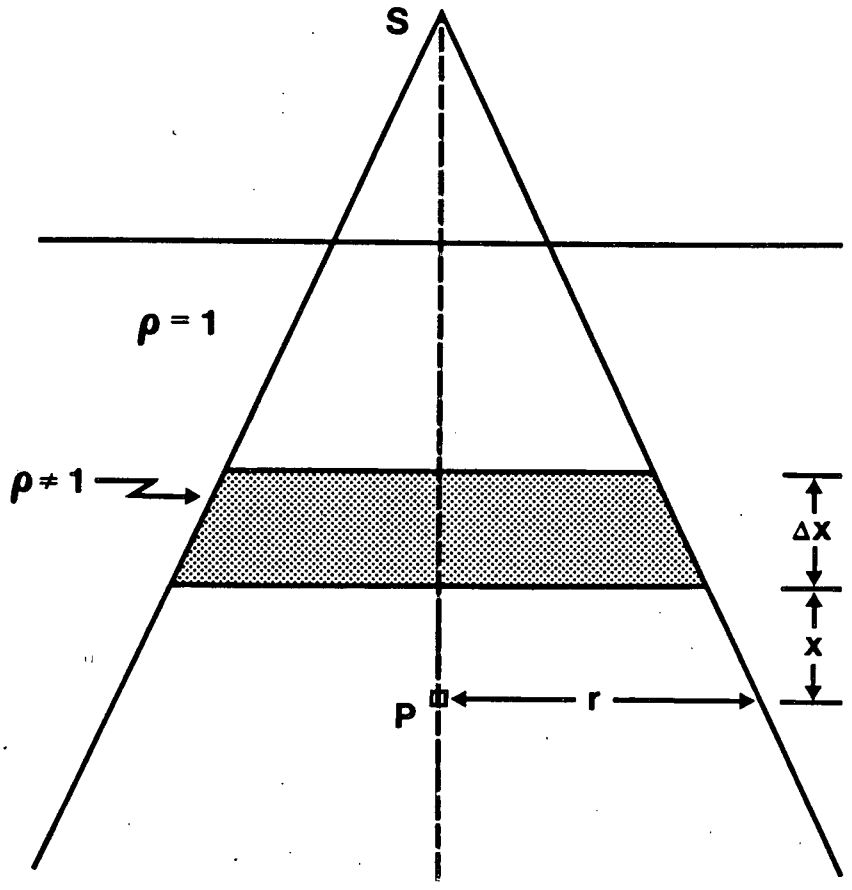

FIGURE 7

SEMI-INFINITE INHOMOGENEOUS SLAB EXTENDING ACROSS THE FIELD

factor proposed by Batho is,

$$CF_B = D_i / D_h = [TAR\ (x,r) / TAR\ (x + \Delta x,\ r)]^{1 - \rho} \quad (1)$$

where TAR (x,r) is the tissue-air ratio for a point at a distance x cm from the slab in a field of radius r cm at the point. This correction factor has been extensively examined since its publication. Young and Gaylord [1970] tested the method experimentally for single slabs of various sizes and electron densities exposed to ^{60}Co photons and 280 kV X rays and found good agreement between measurement and theory. Webb and Fox [1980] further validated the technique for multiple slabs using Monte Carlo simulations.

The Batho method, which corrects the total dose, has been widely used in treatment planning. Its main criterion that the inhomogeneity extends across the entire field is, of course, not always met. However, as shall be shown, it can be modified to correct for inhomogeneities that cover only part of the field.

2.2.3 General Geometries

O'Connor's and Batho's methods assumed simple geometries. Both have been experimentally verified and there is no doubt as to their usefulness in certain cases. The next consideration would be that of a complex heterogeneous medium, such as the body. These geometries are far more complicated, although approximations may be made such that O'Connor's and Batho's methods can be applied. In general, the effects of all irradiated regions should be taken account of. Two

methods are described here that sum all of the contributions of these regions so as to calculate the dose at a point.

2.2.3.1 Differential scatter-air ratio method

The differential scatter-air ratio (dSAR) is an empirical quantity that can be used to estimate the effects of inhomogeneities [Beaudoin, 1968; Cunningham, 1972; Cunningham and Beaudoin, 1972]. The scatter-air ratio is defined as the difference between the tissue-air ratios for a point in a beam of radius r and the same point for a zero radius beam,

$$SAR\ (d,r) = TAR\ (d,r) - TAR\ (d,0) \qquad (2)$$

where d is the depth of the point. The scatter-air ratio, then, is a measure of the scatter dose at a point. The differential scatter-air ratio is the contribution to the SAR from a small volume element (voxel) in the medium. By summing up all of the dSAR's over all voxels in the irradiated medium, one can determine the total scatter contribution.

Consider the geometry of figure (8), which represents an inhomogeneity in a unit-density medium. Beaudoin described the scatter contribution from a voxel in the inhomogeneity as,

$$\Delta S = e^{-\mu(x' - x)}\ dSAR\ \rho\ e^{-\mu(\theta)(y' - y)} \qquad (3)$$

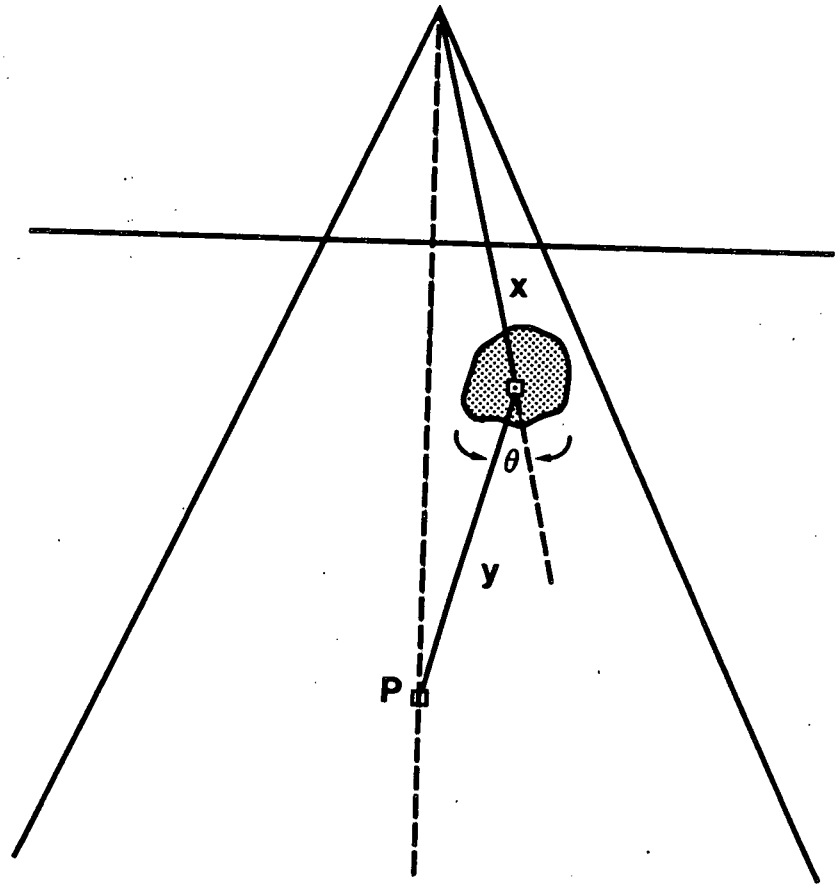

FIGURE 8

IRREGULAR INHOMOGENEITY AFFECTING ONLY SCATTER DOSE

The first exponential term describes the attenuation of the primary photons as they travel to the volume ΔV. x' and y' are density-scaled distances. dSAR is the differential scatter-air ratio for the voxel in the homogeneous water medium and ρ is the relative electron density of the inhomogeneity. The second exponential term gives the attenuation of the scattered photons. μ and $\mu(\theta)$ are the linear attenuation coefficients, in water, for the primary and scattered photons, respectively.

dSAR gives the scatter contribution of the voxel to the point 'P'. The dSAR assumes that the medium is homogeneous with $\rho = 1$ and equation (3) assumes that the inhomogeneity will alter all of the scatter components equally. But Sontag [1979] has shown that the components are affected differently.

The dSAR method's biggest disadvantage is its lengthy computation time due to the necessity of accounting for all of the voxels in the irradiated volume. Sontag states that the computation time is proportional to the square of the field size. Because of this shortcoming, the dSAR method has not been in widespread clinical use.

2.2.3.2 Equivalent tissue-air ratio method

The Sontag-Cunningham equivalent TAR method [Sontag, 1979; Sontag and Cunningham, 1978b] suggests the correction factor,

$$CF_{SC} = D_i / D_h = TAR(d',r') / TAR(d,r) \qquad (4)$$

where D_h is the homogeneous dose at a point at a depth d in a field of radius r, and D_i is the dose at the same point in the inhomogeneous phantom. d' is the effective depth of the point in the inhomogeneous case, i.e., the depth scaled by the electron densities along the beam axis, as by O'Connor, and r' is the scaled radius. Equation (4) is to hold for a general inhomogeneous medium and should approach the O'Connor solution as the medium becomes homogeneous with $\rho \neq 1$.

r' is calculated by scaling the radius r by a weighted average density. This average density is determined by considering the irradiated volume as a series of contiguous planes, corresponding to CT slices, parallel to the beam axis. Weighting factors are then applied to account for the effects of these slices upon the dose. These weighting factors are dSAR's. To simplify the dose calculations, it is assumed that these factors (and, hence, the scatter effects) are independent of each other along an axis mutually perpendicular to the beam axis and the planes. This allows the slices to be reduced to a single equivalent plane parallel to the beam axis. The densities are then averaged over this plane.

The equivalent TAR method has been used clinically [Sontag and Cunningham, 1978a]. Its use of planes makes it amenable to the use of CT slices, and its assumption of the independence of the weighting factors reduces computation time. Without this assumption, it would be necessary to perform a three-dimensional calculation, as with the dSAR method. We would then expect the computation time to be a similar function of the field-size, i.e., proportional to the square. By reducing

the calculations from three dimensions to two, Sontag reports that the calculation time becomes a linear function of the field size.

Yet there are shortcomings to the equivalent TAR method. Each calculation point has a unique set of weighting factors, estimated by calculating the dSAR's for each voxel. However, unlike the Beaudoin-Cunningham method, these calculated dSAR's account for the in-homogeneity's differing effects upon the scatter components. Additionally, by making the assumption that the contiguous slices are independent of each other, one also assumes that the scatter effects of a plane are not affected by the plane between it and the point of interest. This is not a physically valid assumption, and so will introduce errors.

Despite these shortcomings, the equivalent TAR method was the first CT-based inhomogeneity correction scheme widely used.

2.3 Inhomogeneity in the form of an annulus or a cone

It is now of interest to approach the problem of an infinitesimally small off-axis inhomogeneity, which will perturb only the scattered photons reaching a point on the central axis. Such an ideal case can be approximated by a finite elemental inhomogeneity. To obtain a scatter effect large enough to be measured, the inhomogeneity can be extended to a small annulus concentric about the central axis. This annulus will have, approximately, the same scatter perturbation, per unit volume, as the small elemental inhomogeneity at the same radius from the axis. The effects, though, will not be exactly the same due to their non-linearity, as explained in section 2.1.4.

Another related infinitesimal inhomogeneity is that of a line parallel to a fan line from the source. As a point can be extended to an annulus by revolving it around the central axis, a line can be similarly extended to an infinitesimally thin cone. An analysis of such a cone is given in Appendix C.1. The changes in scatter cannot be analytically found. However, a particularly interesting result from this analysis is the prediction that the perturbation will be zero at exactly two points in depth. That is, the scatter change due to this cone is not a monotonic function of depth.

To research the problem of infinitesimally small inhomogeneities, Wong, et. al. [1981b], made extensive measurements of the scatter effects of small low-density annuli in a ^{60}Co beam. They concluded that a theory to calculate the effects of infinitesimal inhomogeneites is of limited use. One cannot extrapolate the effects from such inhomogeneities to those that are macroscopic. One approach, then, that might be of clinical usefulness would be to measure the effects of macroscopic inhomogeneities in the form of finite annuli and cones.

In this thesis, we have measured the scatter changes introduced by such annuli and cones of varying densities in a water phantom exposed to ^{60}Co gamma radiation.

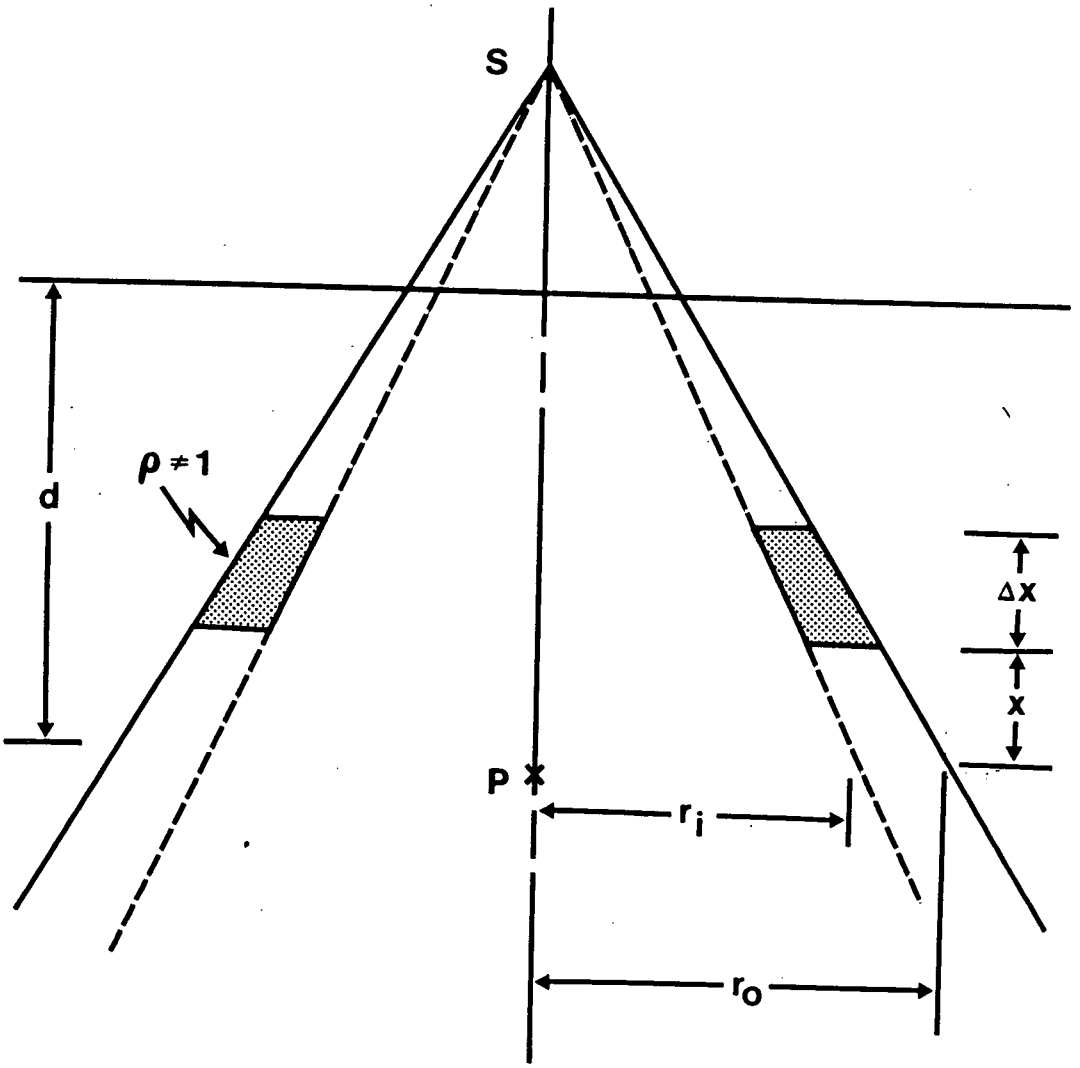

FIGURE 9

ANNULAR INHOMOGENEITY

2.3.1 Differential Batho method

In further study of this problem, Yuen [1980] has developed a technique, based upon the Batho method, for calculating the scatter effects of a finite cone frustum of any density.

This 'differential Batho method' is derived in Appendix B. The method yields two expressions for the correction, denoted by dBM(1) and dBM(2). The dBM(1) calculation should be more accurate than the dBM(2) for the cases where the field size is greater than the inhomogeneity. When the field size approximates the inhomogeneity, the dBM(2) result becomes a better representation. The reasons why are outlined in the appendix.

Consider the geometry of figure (9) with the frustum coincident with the field boundaries. The primary is not affected and only the scatter will be altered. The dBM(1) equation gives the scatter perturbation, normalized to the dose at the same point in a phantom just large enough to ensure maximum buildup, as,

$$\delta_1(r_i,r_o) = TAR\ (d,r_o)\ \Delta CF(r_o) - TAR\ (d,r_i)\ \Delta CF\ (r_i) \qquad (5)$$

where

$$\Delta CF\ (r) = [TAR\ (x,r)\ /\ TAR\ (x + \Delta x,\ r)]^{1\ -\ \rho}\ -\ 1$$

The corresponding dBM(2) calculation is,

$$\delta_2(r_i,r_o) = R\,[TAR\,(x + \Delta x,\ r_o)\ \Delta CF\,(r_o) - TAR\,(x + \Delta x,\ r_i)\ \Delta CF\,(r_i)] \qquad (6)$$

where R is the ratio of the primaries,

$$R = TAR\,(d,0) \,/\, TAR\,(x + \Delta x,\ 0)$$

The measurements and comparisons with the dBM(1) and dBM(2) calculations will be given in chapter 4.

2.3.2 van de Geijn-PoCheng method

In a recent abstract, van de Geijn and PoCheng [1980] have extended the Batho method to correct for an inhomogeneity that is smaller than the field, but which covers the central axis. In Appendix C.2, we have modified their result to correct for a conical inhomogeneity, of density ρ, concentric about the central axis. d is the depth of the point of interest, r_i and r_o are the inner and outer cone radii at the point and x is the length of the cone. The correction factor is,

$$CF_{VP} = 1 - [\,(TAR\,(\rho d,\rho r_i) \,/\, TAR\,(\rho d,\rho r_o)\,]\,[\,1 - \beta^{\alpha}\,] \qquad (7)$$

where,

$$\beta = TAR\,(\rho d,\ \rho r_i) \,/\, TAR\,(0.5\ cm,\ \rho r_i)$$

and,

$$\alpha = (1/\rho) - 1$$

3 APPARATUS AND EXPERIMENTAL PROCEDURE

3.1 Apparatus

All measurements were made with a 0.1 cc Spokas-type ionization chamber with Shonka A-150 tissue-equivalent plastic walls. The chamber was covered with a thin waterproof rubber balloon and the ionization current from the chamber was measured with a Keithley 610C electrometer with digital read-out.

The radiation source was a ^{60}Co therapy machine with the beam shaped by 7.5 cm thick lead alloy circular collimators of varying sizes.

Thin cone frustums were approximated by right annuli 3 cm thick. The width between the inner and outer radii of the annulus was kept at 3 cm. The annuli compositions and densities are given in table V.

For the measurement method used for the annuli, the ring and chamber were suspended in a (40 X 40 X 40) cm^3 water phantom with perspex walls. The chamber was fixed whereas the ring could be positioned by remote-control using an SHM Nuclear X-Y drive.

For large frustums, true cones were used. To further test the non-linearities of multiple inhomogeneities, two cones were made with one concentric about the other. Air and liquids were used for these inhomogeneities, which required hollow cones made from a material with a low atomic number and a relative electron density near one. We elected to use UVEX, a clear plastic used to make headshells for radiotherapy patients.

The dimensions of the cones, fitted into a perspex holder, are shown in figure (10). The two concentric cones were made to fit within a 10 cm diameter field at an SSD of 90 cm. The inner core and slot, both filled with water, were necessary so as to allow the 0.1 cc ionization chamber access along the central axis.

The cones were made by vacuum-forming the UVEX plastic around wood molds. The molds were then removed and the plastic cones fitted together with small nylon screws. The cones were made water-tight with silicone sealant and mounted inside the perspex box. The structure was light and mechanically stable. At the back of each cavity, two holes were drilled to allow the cones to be filled with fluids of various compositions. Small rubber stoppers were used to cover these holes.

For the measurement scheme used, the cones had to be removed from the beam while the chamber remained in place. This was done by

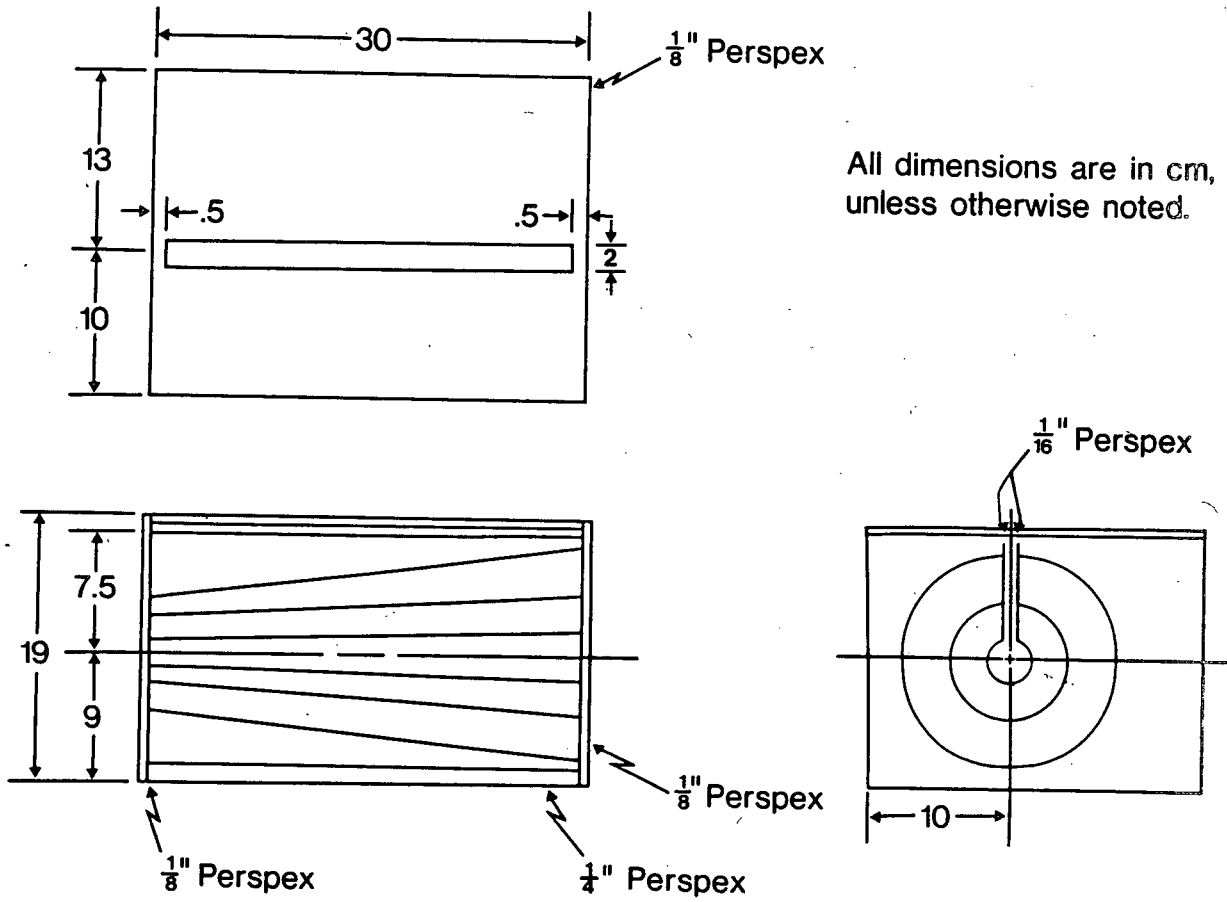

FIGURE 10

PERSPEX CONE STRUCTURE

physically moving the structure on a small steel scissors jack bolted to the phantom floor. The jack was connected to a reversible electric motor by a flexible steel cable. This arrangement was used to raise and lower the cones. Lateral movement was limited by aluminum brackets screwed onto the phantom walls. This system allowed the cones to be moved in and out of the beam about the chamber with the operation monitored by closed-circuit video. The set-up is shown in figure (11).

---- Figure (11) - Cone Experiment Apparatus (Next page)

This photograph shows the main apparatus for the cone experiments. The UVEX cones are on top of the steel jack in the water phantom. The ^{60}Co therapy machine head is at the right of the photograph. The divergence of the cones indicates the beam divergence. One of the aluminum brackets is visible at the end of the cones and it is apparent that it and the jack will affect only the multiple-scatter.

3.2 Measurement methods

3.2.1 Method A

This was the method used in the annuli experiments. The output of the Keithley electrometer, in the current mode, is a voltage proportional to the ionization current. This voltage was measured with a custom-built differential amplifier and a digital voltmeter. The chamber and annulus were aligned with the central axis of a horizontal beam. Then the annulus was removed from the beam to a point where its effect upon the scatter was negligible. The source was exposed and the homogeneous phantom signal from the electrometer recorded using the amplifier and voltmeter. The signal was then nulled with a precision voltage source and the annulus moved into the beam. The differential voltage due to the perturbation introduced by the ring was then measured and recorded. The ratio of the differential to homogeneous voltages would equal the ratio of the scatter dose change to the homogeneous total dose.

The digital voltmeter had a resolution of ± 0.1 mV. Random noise levels were ± 2 mV. For a typical measured signal of 800 mV, these levels limited the measurement resolution to ± 0.25 %.

While planning the cone experiments, we felt that it would be useful to use the apparatus in a manner so as to yield a greater precision. This more accurate method was known as method B.

3.2.2 Method B

The electrometer output was recorded by a Hewlett Packard 680M chart recorder. The cones and chamber were placed in the phantom and centered on the beam axis. The jack was lowered, removing the cones from the beam, and the source exposed.

The homogeneous signal from the Keithley was nulled using the electrometer's zero-adjust control and the recorder switched to a more sensitive scale. The cones were then raised into the beam and the scatter perturbation measured from the recorder. The signal was averaged over a period of about thirty seconds and the entire operation repeated three times to obtain good statistics. A sample trace from the chart recorder is shown in figure (12).

To estimate the resolution of this system, the chamber was placed in a water phantom at a depth of 9.5 cm. A circular field 10 cm in diameter at a 90 cm SSD was used. The chamber was cycled forward a centimeter and back several times in order to create a reproducible change in signal to be measured on the chart recorder. The average relative change of 6 % agreed with data from depth dose tables. This 6 % change produced a 43.2 mm deflection on the chart recorder. As the resolution on the chart paper can be reasonably set at 0.5 mm, the system resolution was estimated as (0.5 / 43.2) X 6 % = 0.07 %.

An estimate of the electronic noise was also made. Figure (13a)

shows a signal obtained from the chamber exposed to the source. Figure (13b) shows the signal for when the source was off and the chamber disconnected from the electrometer. This is is the electronic noise. It can be seen that it accounts for only about a third of the total noise.

It was believed that consideration of the photon statistics would be useful in understanding the nature of the noise measured. Using

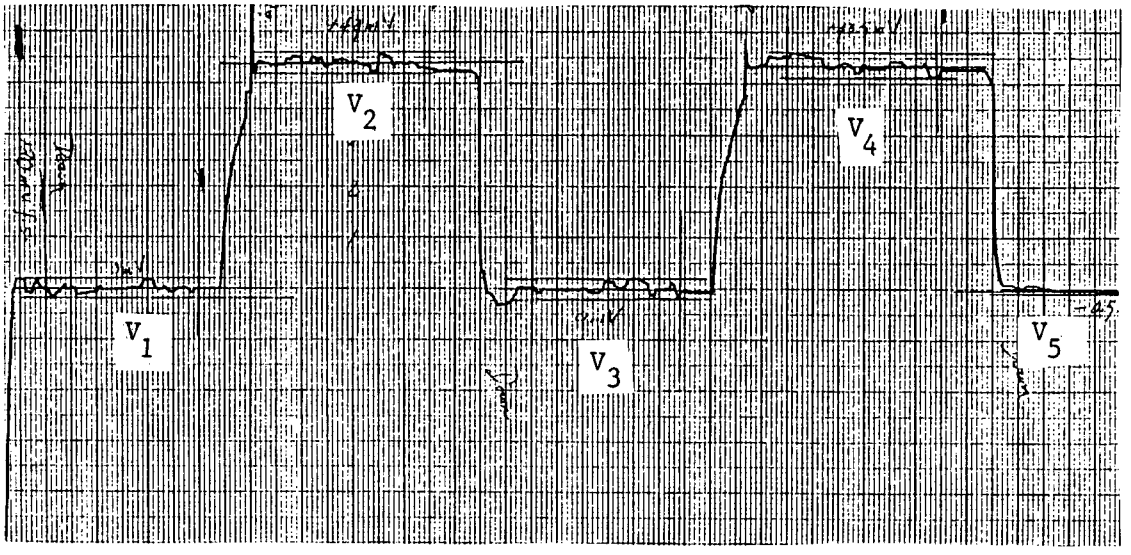

FIGURE 12

SAMPLE DIFFERENTIAL SIGNAL

($V_{1,3,5}$ and $V_{2,4}$ are the voltages corresponding to the unperturbed and perturbed cases, respectively)

The averaged perturbation would be,

$$\tfrac{1}{4}\left((V_2-V_1) + (V_2-V_3) + (V_4-V_3) + (V_4-V_5)\right)$$

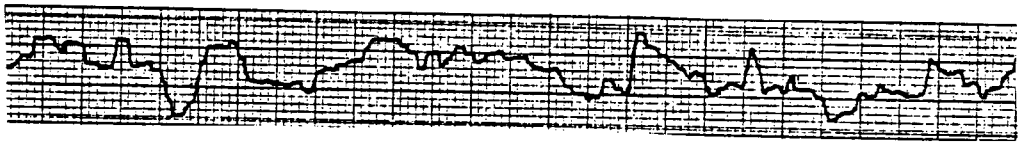

FIGURE 13a

RECORDED NOISE SIGNAL FROM CHAMBER EXPOSED TO ^{60}Co SOURCE

FIGURE 13b

RECORDED INSTRUMENT NOISE

(The scale of the graph is the same

as that of figure 13a)

microdosimetric data, an estimate of the fractional standard deviation of the photon statistics can be obtained.

The air-filled Spokas chamber was approximated by a spherical chamber with a radius of 2.9 mm, so as to retain the 0.1 cc volume. The equivalent unit-density radius would be,

$$\rho\, r = (1.29 \times 10^{-3})\ (2.9\ \text{mm}) = 3.74\ \mu$$

where $\rho = 1.29 \times 10^{-3}$ is the relative electron density of air.

For a uniform photon fluence, the average path length of a secondary electron crossing the chamber will be equal to this radius [Rossi, 1968]. Bengtsson [1972] measured the event size as a function of equivalent unit-density radius for ^{60}Co gamma rays. For a chamber with a radius of 3.74 μ, Bengtsson reports an average event size of 0.5 keV/μ. The average energy released by a secondary electron crossing the chamber will then be,

$$(0.5\ \text{keV}/\mu)\cdot(3.74\ \mu) = 1.87\ \text{keV}$$

Assuming that the mean energy expended by the electron per ion pair formed in air is 33.7 eV, the charge released per event will be,

$$Q = (1.6 \times 10^{-19}\ \text{C / ion pair}) \times (1\ \text{ion pair} / 33.7\ \text{eV}) \times (1870\ \text{eV / event}) = 8.87 \times 10^{-18}\ \text{C / event}$$

or about 55 ion pairs per event. We exposed the chamber to a ^{60}Co

beam 10 cm in diameter at a 90 cm SSD in the water phantom at a depth of 9.5 cm. An average ionization current of 24.1 pA was measured. The measured response time of the system was 0.85 seconds. So, the charge collected by the chamber during this time interval would be,

$$(24.1 \times 10^{-12} \text{ C / sec}) \times (0.85 \text{ sec}) = 2.05 \times 10^{-11} \text{ C}$$

The number of events causing this ionization is,

$$N = (2.05 \times 10^{-11} \text{ C}) / (8.87 \times 10^{-18} \text{ C / event})$$
$$= 2.31 \times 10^{6} \text{ events}$$

The percentage deviation is $\sigma/N = N^{-\frac{1}{2}} = 0.07$ %, approaching the measured resolution. The ultimate limitation, then, in these measurements would be the noise due to the individual quantum fluctuations.

σ/N could be reduced by increasing the collecting volume of the chamber which would require widening the inner water core. However, it was desirable to keep the core and access slot as small as possible in order to approach a true conical shape for the cavities. This results in a trade-off over chamber size.

3.3 Sources of error

3.3.1 Annulus experiments

The annulus was continually cycled in and out of the beam with an estimated reproducibility of ± 0.25 mm. Alignment of the photon beam axis with one axis of the X-Y drive was done visually, using optical cross-hairs projected by the cobalt unit. The annular inhomogeneity and the chamber were also positioned on this axis. Estimated errors in alignment were ± 2 mm or less. The total error due to positioning was of the order of ± 0.25 % of the homogeneous total dose.

Random noise in the measured signal was apparent and, as described in section 3.2.1, limited the measuring resolution to about ± 0.25 %. Because the detector was immersed in a large water bath, temperature changes during the experiment introduced negligible error. Amplifier drift during the reading was small (< 0.25 % of the homogeneous signal per minute).

Adding the two major sources of error in quadrature gives a value of ± 0.35 %, a value consistent with the standard error of repeated measurements of the same point, as can be seen in figures (14) to (16).

3.3.2 Cone experiments

The major contributions to experimental error in the cone experiments were from the following :

(i) The cone structure had some lateral movement such that it would not bind while being raised or lowered and damage the chamber. Misalignment between the beam axis and the center line of the cones was never more than a few millimeters.

(ii) The chamber was centered on the central axis accurately with a homogeneous signal reproducibility of less than ± 1 %. As all of the perturbations were normalized to the homogeneous signals, this error was insignificant.

(iii) When the cones were filled with the liquids, small air bubbles developed. Most of these could be removed, but not all. Also, whenever the cones contained any of the low density materials, they tended to float. Small lead blocks were used as ballast. There was no indication of either the air bubbles or lead blocks affecting the measurements.

(iv) As shown in table IV, the apparatus had a small, but measurable, effect upon the scatter. This affect was accounted for as will be explained later.

(v) Because the horizontal beam had to pass through 1.2 cm of perspex (the phantom wall) and 1.3 cm of water to reach the cones, we assumed that there was 2.5 cm of unit-density material interposed between the cones and the surface. The relative electron density of perspex was 1.146. The errors caused by assuming perspex to be water-equivalent were insignificant in these experiments.

3.4 Experiment procedures

3.4.1 Annulus experiments

Three types of annulus experiments were performed. The scatter changes were measured as a function of the annulus density and the relative positions of the annulus and the point of interest for :

(a) The field size slightly smaller than the annulus; and

(b) The field size much larger than the annulus.

The third annulus experiment was to

(c) Measure the perturbation for the annulus and measuring point fixed but with the field size varying.

3.4.1.1 Field size slightly smaller than the annulus

Parameters for this experiment are given in table I. The ionization chamber was placed at a depth of 30 cm on the central axis and the field radius was 3.5 cm at an 80 cm SSD. The annulus was moved along the central axis from a depth of 15 cm to 25 cm (measured from the face nearest the surface), corresponding to a ring-chamber separation of 12 cm to 2 cm, respectively. Over this range, the field radius varied from 4.3 cm to 4.7 cm. An annulus with a 5 cm outer radius was used.

3.4.1.2 Field size larger than the annulus

Parameters for this experiment are given in table II. This experiment was identical to that described in the previous section, except that the field radius at the surface was increased to 8 cm. The field radius at the annulus varied from 9.7 cm to 10.7 cm.

3.4.1.3 Variable field size

The parameters for this experiment are summarized in table III. The chamber was kept at a 30 cm depth for an 80 cm SSD. An annulus with an outer radius of 5 cm was placed 5 cm in front of the chamber.

For convenience in changing field size, the machine collimator was used in this experiment to produce square fields, each of which was assigned an equivalent radius, according to Batho, et. al., [1956].

TABLE I

ANNULUS EXPERIMENT PARAMETERS I

SSD = 80 cm	SAD = 110 cm
Field radius at surface = 3.5 cm	
Annulus radii : Inner = 2 cm;	Outer = 5 cm
Annulus thickness = 3 cm	
Densities of annuli used : 0.352, 2.33	

TABLE II

ANNULUS EXPERIMENT PARAMETERS II	
SSD = 80 cm	SAD = 110 cm
Field radius at surface = 8 cm	
Annulus radii : Inner = 2 cm;	Outer = 5 cm
Annulus thickness = 3 cm	
Densities of annuli used : 0.352, 2.33	

TABLE III

ANNULUS EXPERIMENT PARAMETERS	
SSD = 80 cm	SAD = 110 cm
Annulus radii : Inner = 2 cm;	Outer = 5 cm
Annulus thickness = 3 cm	
Density of annulus used : 0.028	

3.4.2 Cone experiments

These experiments were to measure the scatter effects caused by the various combinations of inhomogeneities. With two concentric cones

and four materials (see table V), there were $2^4 - 1 = 15$ possible combinations, excluding the case of both cones filled with water.

3.4.2.1 Corrections for conical inhomogeneity measurements

The slot running down the length of the cones was required to allow the ion chamber to travel along the central axis, as can be seen in figure (10). This slot removed some of the scattering material and reduced the effects expected from a full cone. The ratio of the measured change to that of the full cone was assumed to equal the ratio of the actual cavity volume to the theoretical complete cone volume.

The volume of a cone frustum of height h, upper radius r_u and lower radius r_l is,

$$(\pi/3)\ h\ (r_l^2 + r_u^2 + r_l \cdot r_u)$$

Referring to the dimensions of figure (10), we calculated the volume of the full inner cone. The full inner core had a volume of 130 cc. The volume of the full inner cone, including the core, was

$$(\pi/3)\ (30)\ (4^2 + 3^2 + 4 \cdot 3) = 1162.5 \text{ cc}$$

Then the ideal volume of the inner cavity, defined by the inner core and the outer cavity was,

$$1162.5 - 130.0 = 1032.5 \text{ cc}$$

The actual volume was found by weighing the amount of water that filled the cone and dividing the result by the measured density of water to get 855.7 cc. The difference in volumes was due to the slot and the thickness of the plastic . The correction factor for the inner cavity was,

$$k_{in} = 1032.5 \text{ cc} / 855.7 \text{ cc} = 1.20_7$$

The volume correction factors for the outer cavity and both cavities used together, k_{out} and k_{total}, were 1.14_5 and 1.16_5, respectively. Then, the normalized scatter perturbation was defined as,

$$\delta = k\delta_m - \lambda$$

where k is the appropriate correction factor, δ_m is the measured normalized perturbation and λ is a quantity to account for the effects due to the apparatus itself. Again, a linear relationship was assumed.

The apparatus was not expected to alter the scatter to any great degree. The metal components were all outside the beam and would affect only the second- and higher-order scatter components. This small effect should justify the linearity assumption.

To measure the scatter effect due to the apparatus, both the inner and outer cones were filled with water. A measurement protocol was set such that the perturbations for all combinations of inhomogeneities were measured at depths of 5, 8, 10, 15 and 20 cm. Beyond 20 cm, backscatter from the water behind the cones would alter the perturbations.

In addition, clinical interest would be limited to those effects occurring in the first 20 cm anyway. λ values were measured and are given in table IV.

TABLE IV

PERCENTAGE DOSE CHANGE DUE TO CONE APPARATUS

	DEPTH (CM)				
	5	8	10	15	20
λ	+0.19	+0.29	+0.21	+0.03	+0.07

These measurements did not have to be corrected for the volume. The effects are less than 0.3 % and are within experimental resolution for the last two depths.

A summary of the shapes and materials of the inhomogeneities used is given in table V. The relative electron density in each case was determined from the measured physical density and an assumed chemical composition of the inhomogeneity.

TABLE V

INHOMOGENEITIES

RELATIVE ELECTRON DENSITY	MATERIAL	GEOMETRY	MEASUREMENT METHOD[1]
0.000	Air	Cone	B
0.028	Polystyrene[2]	Annulus	A
0.352	Cedar wood[3]	Annulus	A
0.860	Mineral oil[4]	Cone	B
1.580	Witt liquid[5]	Cone	B
2.330	Aluminum	Annulus	A

1 - 'A' refers to method using electrometer, amplifier and voltmeter
'B' refers to method using electrometer and chart recorder

2 - Polystyrene foam : 92.26 C, 7.74 H by weight

3 - Cedar wood : assumed to be cellulose ($C_6 H_{10} O_5$)

4 - Mineral oil : composed of a mixture of paraffins

5 - Witt liquid : saturated aqueous solution of $K_2 HPO_4$ [White, 1978]

4 RESULTS AND DISCUSSION

4.1 Results from annulus experiments

4.1.1 Field size slightly smaller than the annulus

Scatter perturbations were measured for annulus relative electron densities of $\rho = 0.352$ and $\rho = 2.33$. The parameters of the experiment are given in table I. The experimental results (of the perturbation normalized to the total dose in the homogeneous phantom) are plotted in figures (14a) and (14b).

The error bars on these and other plots are the standard errors for each set of measurements.

4.1.2 Field size larger than the annulus

Scatter perturbations were also measured for annulus densities of $\rho = 0.352$ and 2.33 and the parameters are summarized in table II. The experimental results are plotted in figures (15a) and (15b).

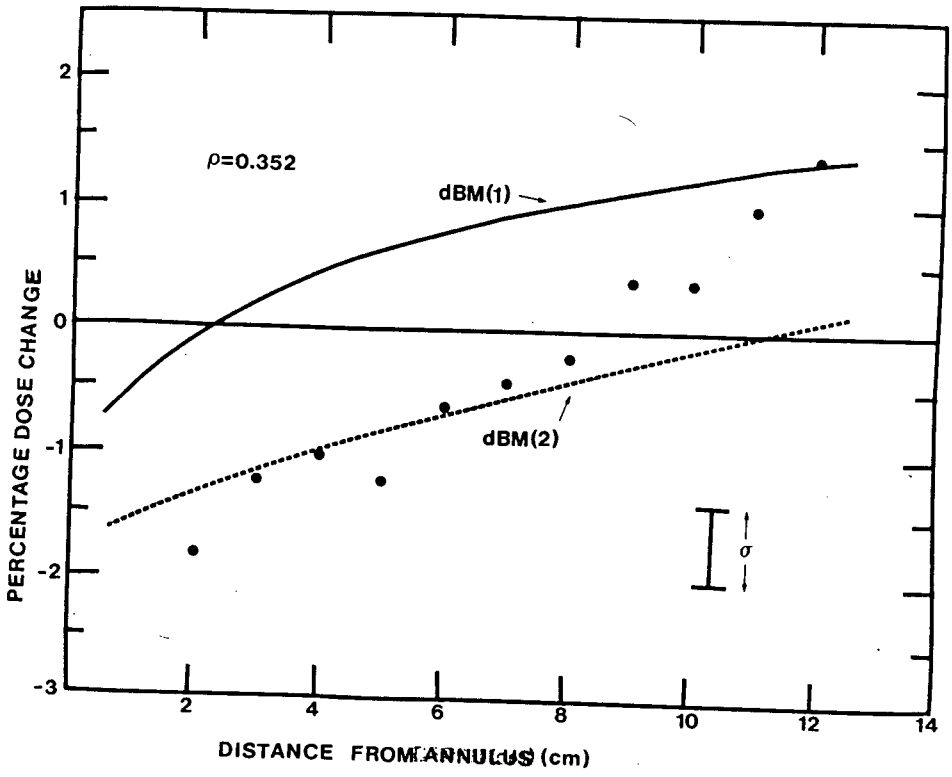

FIGURE 14a

PERCENTAGE DOSE CHANGE VS. DISTANCE
FOR FIELD SLIGHTLY SMALLER THAN THE ANNULUS (ρ = 0.352)

(Experiment parameters are on page 41, table I)

(For figures 14 - 16, the dots are the measured data)

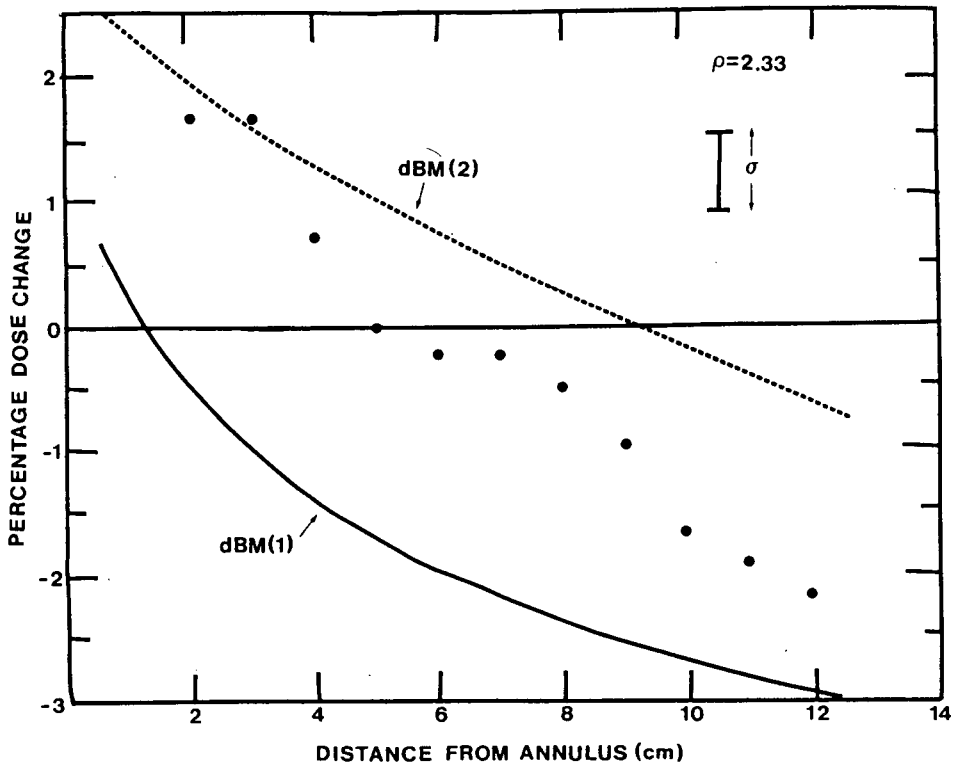

FIGURE 14b

PERCENTAGE DOSE CHANGE VS. DISTANCE
FOR FIELD SLIGHTLY SMALLER THAN THE ANNULUS (ρ = 2.33)

(Experiment parameters are on page 41, table I)

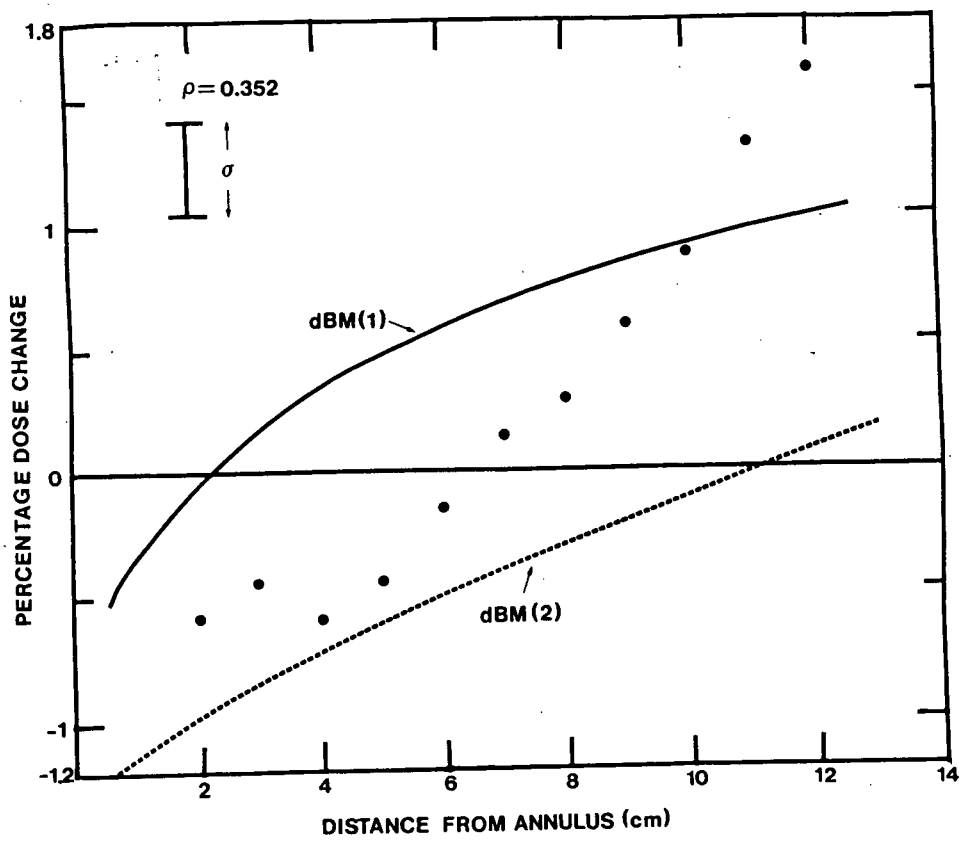

FIGURE 15a

PERCENTAGE DOSE CHANGE VS. DISTANCE
FOR FIELD LARGER THAN THE ANNULUS (ρ = 0.352)

(Experiment parameters are on page 42, table II)

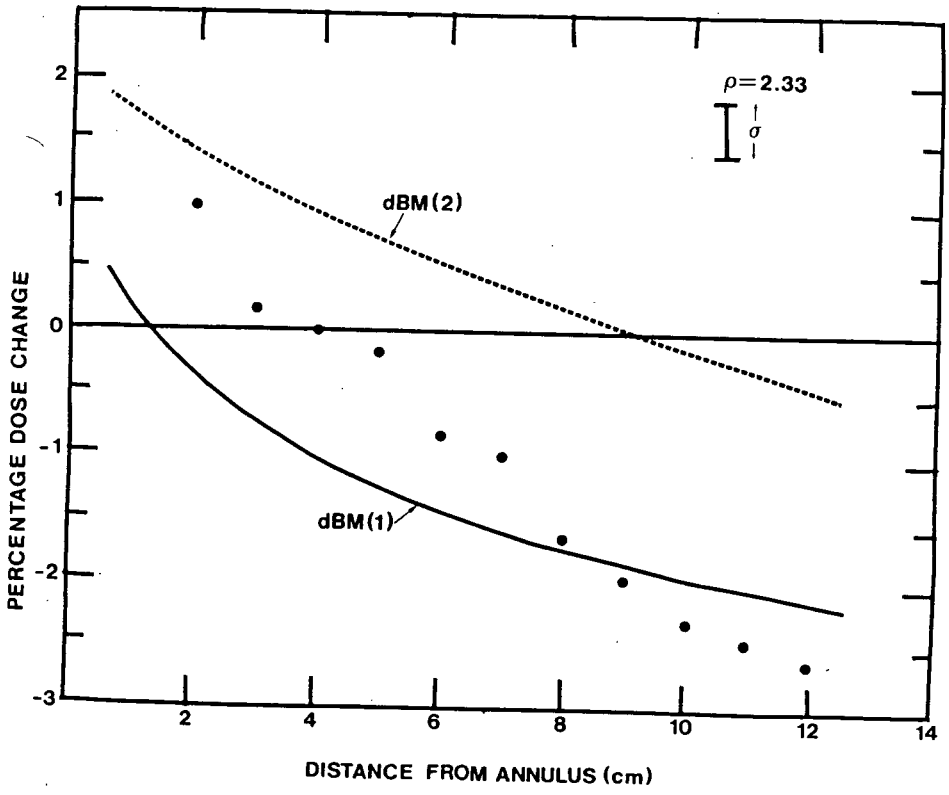

FIGURE 15b

PERCENTAGE DOSE CHANGE VS. DISTANCE
FOR FIELD LARGER THAN THE ANNULUS (ρ = 2.330)

(Experiment parameters are on page 42, table II)

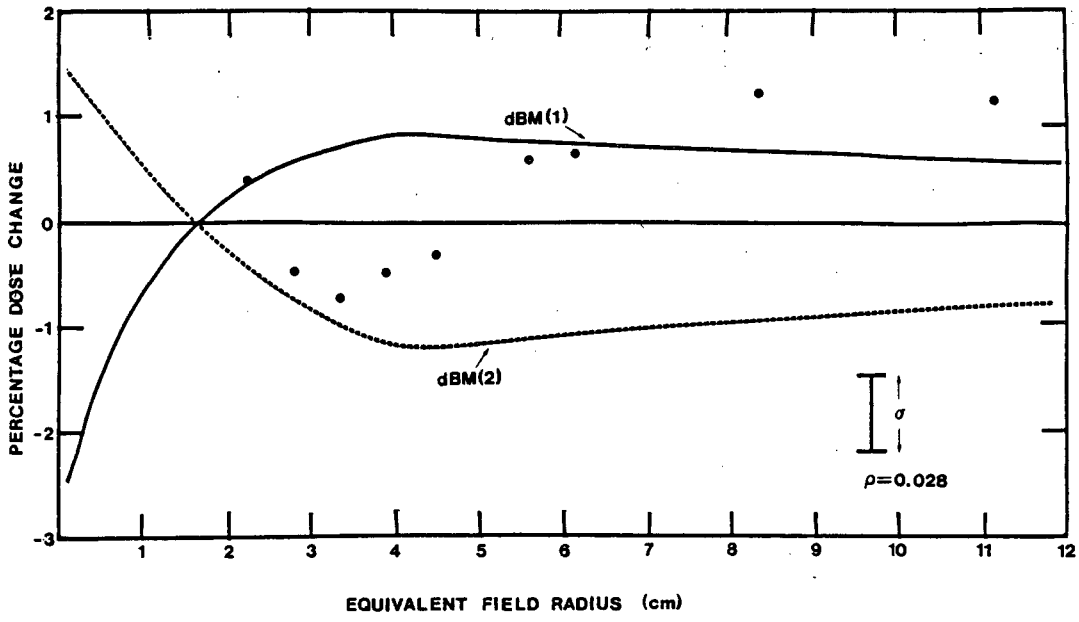

FIGURE 16

PERCENTAGE DOSE CHANGE VS. EQUIVALENT FIELD RADIUS

(ρ = 0.028)

(Experiment parameters are on page 42, table III)

4.1.3 Variable field size

As described in section 3.4.1.3, a single annulus in a fixed position was used and the field size varied. A polystyrene foam annulus (ρ = 0.028) was chosen. A summary of the parameters is given in table III and the results are plotted in figure (16).

For some fields, the annulus outer radius was greater than the field radius such that not all of the annulus was irradiated. To correct for this condition, when the field radius was smaller than the annulus outer radius the outer radius was set equal to the field radius.

4.1.4 Discussion of annulus experiments

The differential Batho method assumes that the cone frustum or annulus is coincident with the field boundaries. Despite this restriction, the method gives a good qualitative representation of the scatter perturbations when this condition is relaxed. As can be seen in figures (14) to (16), the two calculation types seem to set boundaries on these perturbations which are exceeded only when the field is much larger than the annulus.

4.1.4.1 Dependence of scatter changes upon density and depth

From figures (14a) and (15a), it is apparent that for an annulus density of less than one, the scatter changes are negative near the annulus and positive for points sufficiently deep. This is due to the reduction in the number of scattering centers in the volume displaced by the annulus.

Further behind the annulus, the scatter has increased due to the increase in transmission of the primary through the ring. This generates more scatter behind the annulus. The opposite arguments hold for $\rho > 1$, the results of which are shown in figures (14b) and (15b).

Both figures (14) and (15) show that for both densities, the measured data is closer to the dBM(2) result when near the annulus and approaches dBM(1) further away. This is due to both the filtration effect (see Appendix B) which is accounted for in the dBM(1) calculation, but not in the dBM(2), and the angular distribution of the Compton scattered photons.

For ^{60}Co photon energies, the angular distribution of the Compton scattered photons is peaked in the forward direction, so the probability of such photons being scattered at a wide angle is relatively small.

When the chamber is behind and near the annulus, the only photons it detects which have undergone the filtration effect are those which have been scattered through a wide angle. As these photons comprise a small fraction of all the scattered photons, the observed filtration effect will be at a minimum and the dBM(2) will be a better measure of the scatter change. As the chamber and annulus are separated, more of the predominant small angle scatter is altered by the filtration effect and the dBM(1) becomes a better representation.

4.1.4.2 Dependence of scatter changes upon field size

From figure (16), it is apparent that the scatter perturbation, as

a function of field size, is not monotonic.

The measured results tend to the dBM(2) calculation when the annulus is larger than or equal to the field size. When the field size becomes larger than the annulus, the measured results reverse direction and approach dBM(1). As the field radius further increases, the results exceed even the dBM(1) calculation and appear to approach an asymptotic maximum.

This effect can be explained qualitatively. As the field radius is increased, more regions between the surface and annulus are irradiated - leading to an increase in forward scatter. This scatter is transmitted (either with a gain or a loss) through the annulus to affect the scatter dose along the central axis behind the ring. Thus, one would expect the dBM(1) calculation, which includes the filtration effect, to be more accurate than the dBM(2) for large field sizes. This conclusion is observed.

As mentioned previously, Wong and others [1981b] performed similar annulus experiments at the Ontario Cancer Institute. They measured the scatter perturbation at a single fixed central axis point at a depth of 10 cm in a water phantom for a single ^{60}Co field of diameter 20 cm at an SSD of 90 cm. Polystyrene foam annuli (with a density given as 0.026) of varying sizes, but with a constant 2.5 cm thickness, were used. The results were plotted as an isoeffect contour plot which showed regions of increased and decreased scatter in a manner qualitatively similar to our results.

Moreover, they calculated the effects using a semi-analytical technique that accounted for the scatter up to second-order. The calculated results agreed qualitatively with those measured. However, as the calculations did not include scatter of third-order and higher, the quantitative differences between measurement and theory were appreciable. Additionally, their theory allows one to calculate the effects due, essentially, to the complete removal of the scattering centers within a volume ($\rho = 0$). It does not give any indication how these results can be used to predict the effects for a finite inhomogeneity of arbitrary density.

4.2 Results from cone experiments

The cone results are from a number of experiments with separate set-ups done over a period of several weeks. It was apparent that measurements from a single experiment showed greater consistency than data taken with different set-ups. We believed that these variations were due to one or more unidentified systematic errors in the experimental set-up. We expected, however, that the dependence of the scatter effects upon density should be a smooth function.

The experimental values at each depth were examined as functions of the two variables : inner and outer densities. These values were cross plotted (inner density versus perturbation for constant outer density and outer density versus perturbation for constant inner density) and the results were then least-squares fitted to quadratics [Walpole and Myers, 1972].

Figures (17a) and (17b) are sample cross plots for the 10 cm depth. Figure (17a) shows the scatter perturbations as a function of inner cone density for a constant outer cone density, and figure (17b) shows the perturbation as a function of outer cone density for a constant inner cone density. Generally, there is a good fit between the curves and the measured data, except for the cases when a cone is filled with air. The standard error between the measured and fitted data was calculated to be 0.4 %.

The smoothed scatter perturbations are given in tables VI (a - e).

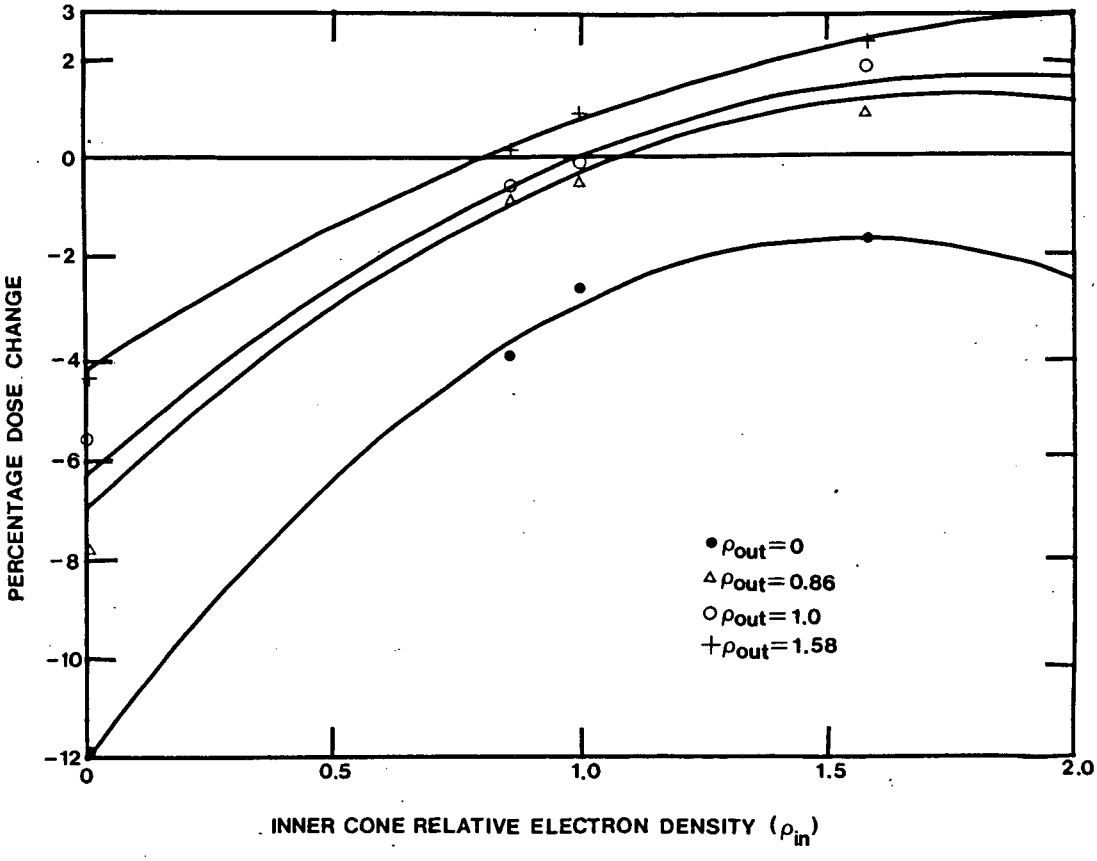

FIGURE 17a

PERCENTAGE DOSE CHANGE VS. INNER CONE DENSITY
(LEAST-SQUARES QUADRATIC FIT)
FOR 10 CM DEPTH

(For figures 17a and 17b, the points are the measured data and the lines are the fitted quadratics)

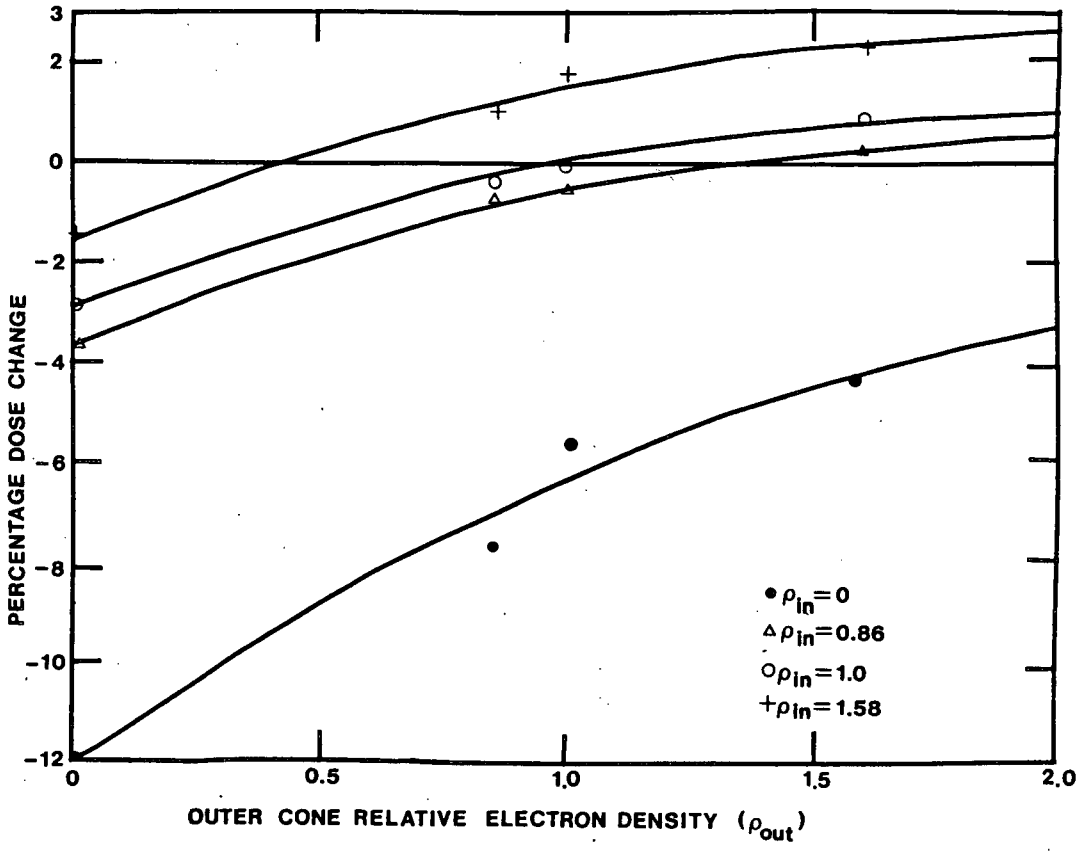

FIGURE 17b

PERCENTAGE DOSE CHANGE VS. OUTER CONE DENSITY
(LEAST-SQUARES QUADRATIC FIT)
FOR 10 CM DEPTH

TABLE VIa

PERCENTAGE DOSE CHANGE (SMOOTHED) AT 5 CM

	ρ_{OUT}			
	0.00	0.86	1.00	1.58
ρ_{in}				
0.00	-3.67	-2.49	-2.33	-1.79
0.86	-1.39	-0.53	-0.55	+0.15
1.00	-1.12	-0.22	-0.09	+0.44
1.58	-0.28	+1.01	+1.15	+1.55

TABLE VIb

PERCENTAGE DOSE CHANGE (SMOOTHED) AT 8 CM

	ρ_{OUT}			
	0.00	0.86	1.00	1.58
ρ_{in}				
0.00	-9.41	-5.75	-5.25	-3.50
0.86	-2.78	-0.82	-0.57	+0.19
1.00	-2.15	-0.25	-0.02	+0.68
1.58	-0.87	+1.41	+1.65	+2.25

TABLE VIc

PERCENTAGE DOSE CHANGE (SMOOTHED) AT 10 CM

	ρ_{OUT}			
	0.00	0.86	1.00	1.58
ρ_{in}				
0.00	-12.04	-6.96	-6.32	-4.23
0.86	-3.65	-0.85	-0.53	+0.33
1.00	-2.90	-0.28	+0.07	+0.86
1.58	-1.57	+1.26	+1.57	+2.46

TABLE VId

PERCENTAGE DOSE CHANGE (SMOOTHED) AT 15 CM

	ρ_{out}			
	0.00	0.86	1.00	1.58
ρ_{in}				
0.00	-15.89	-8.18	-7.36	-5.25
0.86	-5.56	-0.74	-0.28	+0.65
1.00	-4.69	-0.15	+0.27	+1.07
1.58	-3.55	+0.45	+0.77	+1.10

TABLE VIe

PERCENTAGE DOSE CHANGE (SMOOTHED) AT 20 CM

	ρ_{OUT}			
	0.00	0.86	1.00	1.58
ρ_{in}				
0.00	-18.13	-8.45	-7.60	-6.26
0.86	-6.56	-0.47	-0.05	-0.02
1.00	-5.62	-0.08	+0.30	+0.32
1.58	-4.54	-1.17	-0.86	-0.31

4.2.1 Discussion of cone experiments

From the data, it is obvious that the scatter effects are complicated functions of depth and density. What are of interest are the interactions between inhomogeneities. It is known that the scatter effects are non-additive, but we considered the possibility that under certain geometries useful approximations could be obtained by the addition of effects.

To examine this possibility, we examined the effects of changing one cone's density while maintaining the other constant. This was done by looking at the ratios of correction factors. The correction factor is

the ratio of the inhomogeneous to homogeneous doses, and is related to the normalized scatter perturbation by,

$$CF = D_i / D_h = (D_h + \delta) / D_h = 1 + (\delta / D_h)$$

Consider a ratio of correction factors, CF_f/CF_i, where CF_i is the correction factor for the initial density combination and CF_f is that for the final combination. If the ratio is greater than one, then there is an increase in the scatter dose. Correspondingly, if the ratio is less than one, there is a decrease.

We analyzed the effect of increasing one cone's density from 1 to 1.58 (or decreasing it from 1 to 0) with the other cone density held constant. Table VIIa gives the ratios for when the outer density is increased from 1 to 1.58, table VIIb shows the ratios for when the inner density is increased from 1 to 1.58, table VIIc is for when the outer density is decreased from 1 to 0 and table VIId gives the ratios for when the inner density is decreased from 1 to 0. The smoothed data were used in calculating the correction factors.

TABLE VIIa

RATIO OF CORRECTION FACTORS FOR INCREASING OUTER CONE DENSITY

$CF(\rho_{in},\rho_{out})$ Ratio	Depth (cm)				
	5	8	10	15	20
$\frac{CF(0,1.58)}{CF(0,1)}$	1.006	1.019	1.022	1.023	1.015
$\frac{CF(.86,1.58)}{CF(.86,1)}$	1.006	1.008	1.009	1.009	1.000
$\frac{CF(1,1.58)}{CF(1,1)}$	1.004	1.007	1.009	1.011	1.003
$\frac{CF(1.58,1.58)}{CF(1.58,1)}$	1.004	1.006	1.009	1.004	1.006

TABLE VIIb

RATIO OF CORRECTION FACTORS FOR INCREASING INNER CONE DENSITY

$CF(\rho_{in},\rho_{out})$ Ratio	Depth (cm)				
	5	8	10	15	20
$\frac{CF(1.58,0)}{CF(1,0)}$	1.009	1.013	1.014	1.011	1.011
$\frac{CF(1.58,.86)}{CF(1,.86)}$	1.012	1.017	1.015	1.006	0.989
$\frac{CF(1.58,1)}{CF(1,1)}$	1.012	1.017	1.016	1.008	0.991
$\frac{CF(1.58,1.58)}{CF(1,1.58)}$	1.014	1.016	1.016	1.014	0.994

TABLE VIIc

RATIO OF CORRECTION FACTORS FOR DECREASING OUTER CONE DENSITY

$CF(\rho_{in},\rho_{out})$ Ratio	Depth (cm)				
	5	8	10	15	20
$\frac{CF(0,0)}{CF(0,1)}$	0.986	0.956	0.939	0.908	0.886
$\frac{CF(.86,0)}{CF(.86,1)}$	0.992	0.978	0.969	0.947	0.935
$\frac{CF(1,0)}{CF(1,1)}$	0.989	0.979	0.971	0.953	0.944
$\frac{CF(1.58,0)}{CF91.58,1)}$	0.986	0.975	0.969	0.957	0.963

TABLE VIId

RATIO OF CORRECTION FACTORS FOR DECREASING INNER CONE DENSITY

$CF(\rho_{in},\rho_{out})$ Ratio	Depth (cm)				
	5	8	10	15	20
$\frac{CF(0,0)}{CF(1,0)}$	0.974	0.926	0.906	0.883	0.868
$\frac{CF(0,.86)}{CF(1,.86)}$	0.977	0.945	0.934	0.920	0.916
$\frac{CF(0,1)}{CF(1,1)}$	0.977	0.948	0.937	0.926	0.924
$\frac{CF(0,1.58)}{CF(1,1.58)}$	0.986	0.959	0.950	0.938	0.934

Several comments can be made about these results. The first is the obvious, and expected, result that changing the inner cone density will have a generally greater effect upon the central-axis scatter dose than will changing the outer cone density. An exception to this occurs when the inner cone is filled with air. In that case, there is complete transmission of the outer cone's scatter effects to the central axis.

One can also see that, except for the case of the outer cone filled with air, the effect of changing the inner density, at each depth, is almost entirely independent of the outer cone density (tables VIIb and VIId). This is a critical observation. If we can assume that the effect of the inner cone density upon the central-axis scatter dose is independent of the outer cone density, then an additivity in these scatter effects may also be assumed.

To further investigate this assumption, we compared the sums of effects to the total effects. For example, we summed the scatter change due to the inner cone filled with water and the outer cone filled with oil with those due to the inner cone filled with oil and the outer cone filled with water. We compared this sum to the scatter effects due to both cones filled with oil. The comparisons of all of the density combinations is given in table VIII. Smoothed data were again used. Three cases, $\delta(0,0)$, $\delta(1.58,1.58)$ and $\delta(0,1.58)$ are plotted in figures (18a), (18b) and (18c), along with the summed effects.

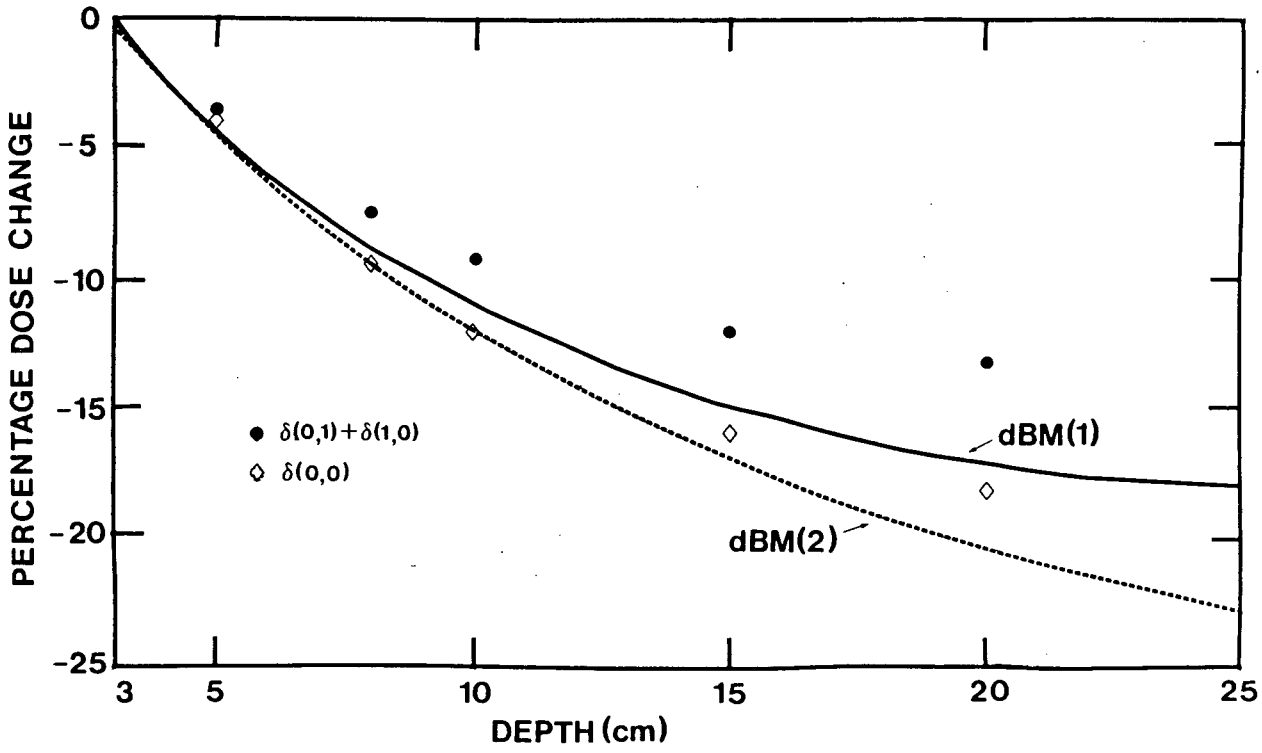

FIGURE 18a

COMPARISON OF SUMMED AND NET EFFECTS

FOR $\rho_{in} = \rho_{out} = 0$

(For figures 18a, 18b and 18c, the points are the smoothed data)

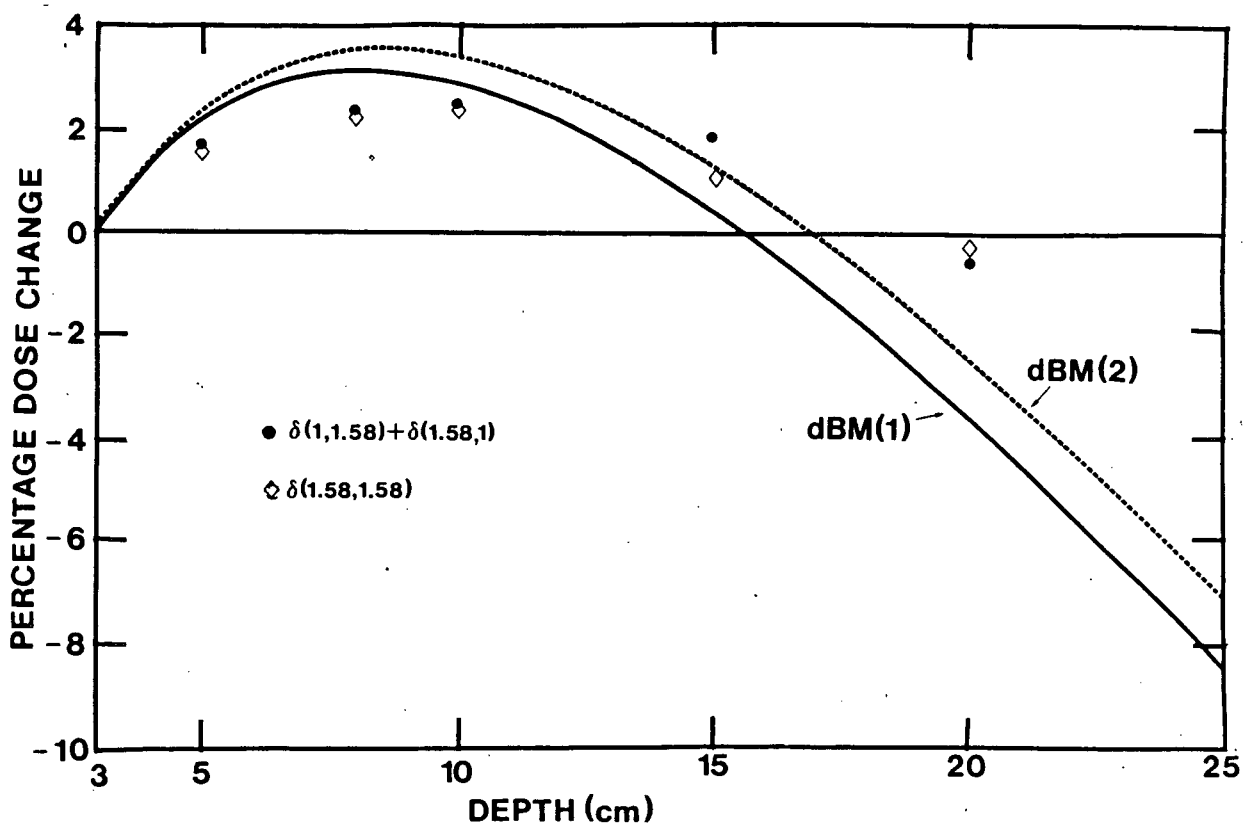

FIGURE 18b

COMPARISON OF SUMMED AND NET EFFECTS

FOR $\rho_{in} = \rho_{out} = 1.58$

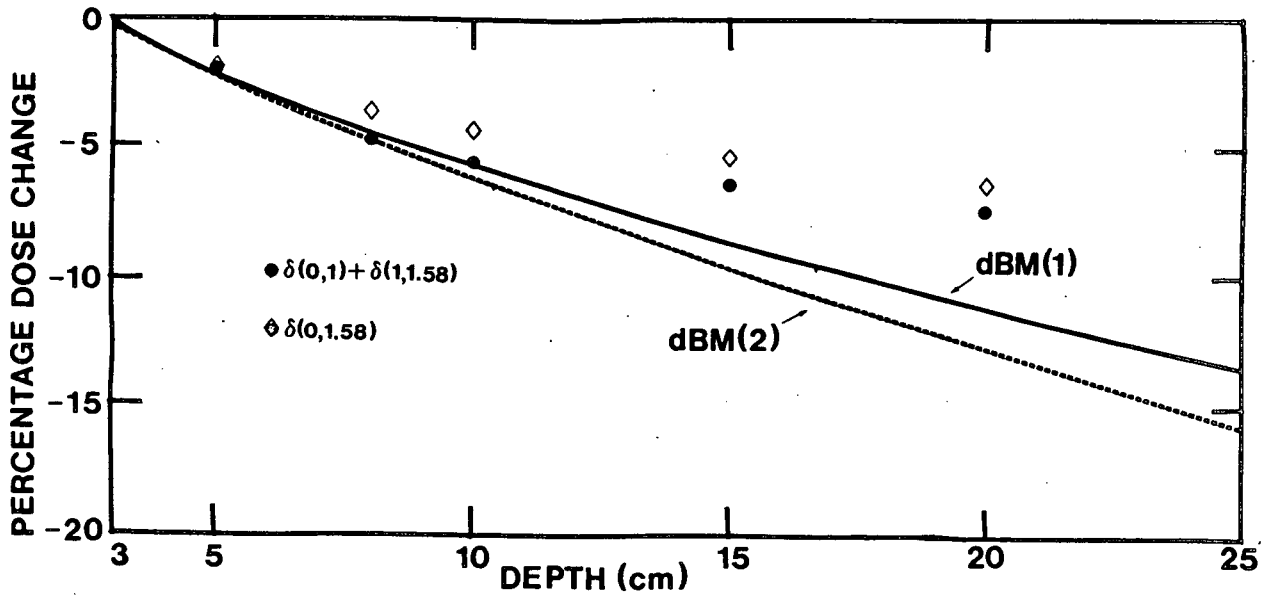

FIGURE 18c

COMPARISON OF SUMMED AND NET EFFECTS

FOR ρ_{in} = 0 AND ρ_{out} = 1.58

TABLE VIII

COMPARISON OF ADDED EFFECTS TO NET EFFECT

PERCENTAGE DOSE CHANGE

$\delta(\rho_{in},\rho_{out})$	Depth (cm)				
	5	8	10	15	20
$\delta(1,0)+\delta(0,1)$	-3.45	-7.40	-9.22	-12.05	-13.22
$\delta(0,0)$	-3.67	-9.41	-12.04	-15.89	-18.13
$\delta(1,.86)+\delta(.86,1)$	-0.77	-0.82	-0.81	-0.43	-0.13
$\delta(.86,.86)$	-0.53	-0.82	-0.85	-0.74	-0.47
$\delta(1,1.58)+\delta(1.58,1)$	+1.59	+2.33	+2.43	+1.85	-0.54
$\delta(1.58,1.58)$	+1.55	+2.25	+2.46	+1.10	-0.31
$\delta(0,1)+\delta(1,.86)$	-2.55	-5.50	-6.60	-7.51	-7.68
$\delta(0,.86)$	-2.49	-5.75	-6.96	-8.18	-8.45
$\delta(0,1)+\delta(1,1.58)$	-1.89	-4.57	-5.46	-6.29	-7.28
$\delta(0,1.58)$	-1.79	-3.50	-4.23	-5.25	-6.26
$\delta(.86,1)+\delta(1,0)$	-1.67	-2.72	-3.43	-4.97	-5.67
$\delta(.86,0)$	-1.39	-2.78	-3.65	-5.56	-6.56

TABLE VIII (CONTINUED)

COMPARISON OF ADDED EFFECTS TO NET EFFECT

PERCENTAGE DOSE CHANGE

$\delta(\rho_{in},\rho_{out})$	Depth (cm)				
	5	8	10	15	20
$\delta(.86,1)+\delta(1,1.58)$	-0.11	+0.11	+0.33	+0.79	+0.27
$\delta(.86,1.58)$	+0.15	+0.19	+0.33	+0.65	-0.02
$\delta(1.58,1)+\delta(1,0)$	+0.03	-0.50	-1.33	-3.92	-6.48
$\delta(1.58,0)$	-0.28	-0.87	-1.57	-3.55	-4.54
$\delta(1.58,1)+\delta(1,.86)$	+0.93	+1.40	+1.29	+0.62	-0.94
$\delta(1.58,.86)$	+1.01	+1.41	+1.26	+0.45	-1.17

In most cases, except for that of both cones filled with air, the sum of the effects agrees very well with the net effect. This result is somewhat surprising. In section 2.1.4, it was argued that the effects of inhomogeneities upon the scatter dose were dependent and non-additive. This is strictly true. As we have found here, some geometries in fact allow the effects to be summed to give a useful approximation to the total effect.

Before explaining this behavior, we should remind ourselves of the Monte Carlo result in figure (2). Although the net scatter component of the 10 cm diameter field can account for more than 30 % of the total, multiple-scatter (second-order and higher) is well below 10 % of the total. With this in mind, consider figure (19).

Consider two inhomogeneities varying radially. If we measure their effects at a point 'P' sufficiently far down the central axis, very little of the scatter from inhomogeneity 2 is filtered by inhomogeneity 1 before reaching 'P'. Secondly, any photons scattered from either inhomogeneity and then scattered by the other prior to reaching 'P' must be second-order or higher. These photons are only a small amount of the total reaching 'P'. Because the interactions between the inhomogeneities are small in this case, we can approximate the net effect with the sum of the effects. This is not always true. For example, consider the case of two inhomogeneities that are stacked one upon the other. All of the scatter components reaching central-axis points behind them are affected by the interactions between inhomogeneities. In this case, one cannot say that the sum of the effects is equal to the net perturbation.

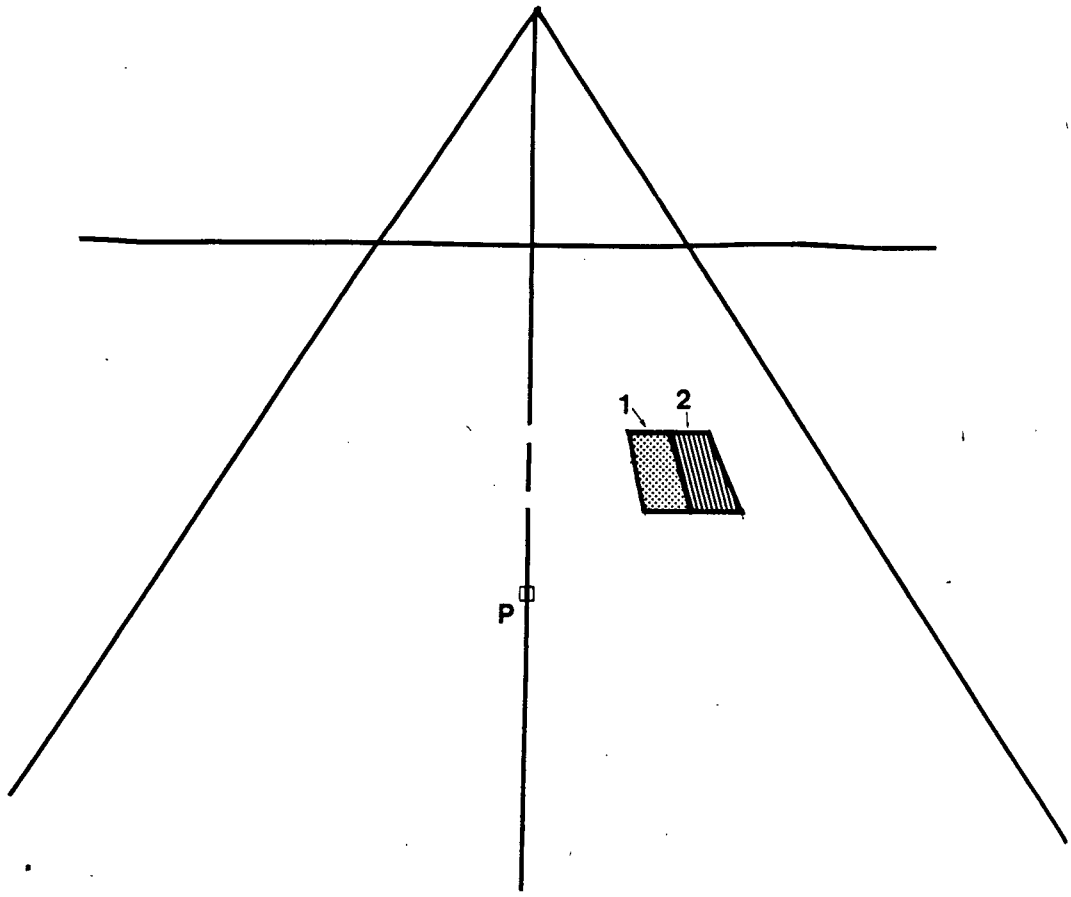

FIGURE 19

MULTIPLE INHOMOGENEITIES VARYING RADIALLY

The concentric cones used in these experiments are extensions of the inhomogeneities in figure (19). Except for the penumbra, the inhomogeneous cones fill all of the regions exposed to the primary radiation. And yet the effects are still virtually additive. This property may prove to be clinically useful, as will be shown later.

4.2.1.1 Differential Batho method calculations

The differential Batho method can take account of an inhomogeneity lying between any two depths less than or equal to that of the point of interest. However, in these cone experiments, the inhomogeneity extended beyond the point of interest. There were scatter changes due to the regions all around the point. Thus, before comparing the dBM calculations to the measured data, we know that exact agreement is unlikely.

The tissue-air ratio for ^{60}Co is not defined for depths of less than the 0.5 cm buildup depth. Consequently, the dBM calculations assumed that the cone extended from 2.5 cm below the surface (as in the experiment) to 0.5 cm above the point measured. Scatter effects from regions deeper than this point were neglected.

In figures (20a - 20o), the dBM(1) and dBM(2) results are plotted, with the smoothed data, against depth for all of the density combinations. As shown by the analysis in Appendix C.1, the scatter perturbations are not monotonic with depth, except for the cases where one of the cones is filled with air. In these cases, there has been an almost complete removal of the scattering centers in the volume. The scatter effects will

then vary over a much greater distance such that of the first 20 cm, the effects are seen as monotonically decreasing.

There is good qualitative agreement between the differential Batho method calculations and the data. The quantitative agreement is best up to a depth of about 15 cm. The reason why is probably due to the backscatter changes neglected by the differential Batho method. Especially in the case when one of the cavities contains air, there is complete transmission of the backscatter, from the water far behind the cavities, with little attenuation. It is likely that this is responsible for the poorer agreement with increasing depth.

For cases where there are combinations of densities (say an inner density of 1.58 and an outer density of 0.86), the additive property of the differential Batho method was used. That is, the individual scatter perturbation of each cone was calculated separately and then summed. There is a good correlation between the calculated and measured values for these combinations.

In figures (20a - 20o), the dots represent the smoothed data.

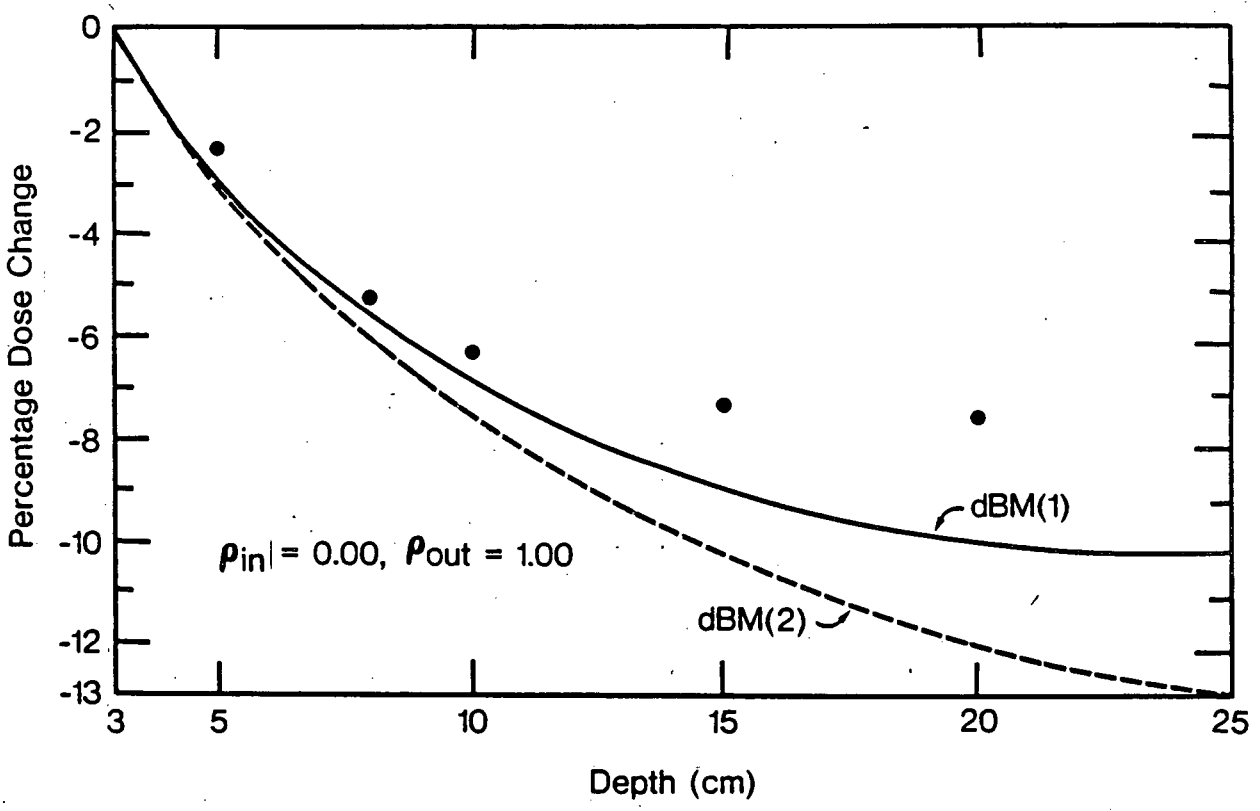

FIGURE 20a - dBM AND MEASURED RESULTS ($\rho_{in} = 0$, $\rho_{out} = 1$)

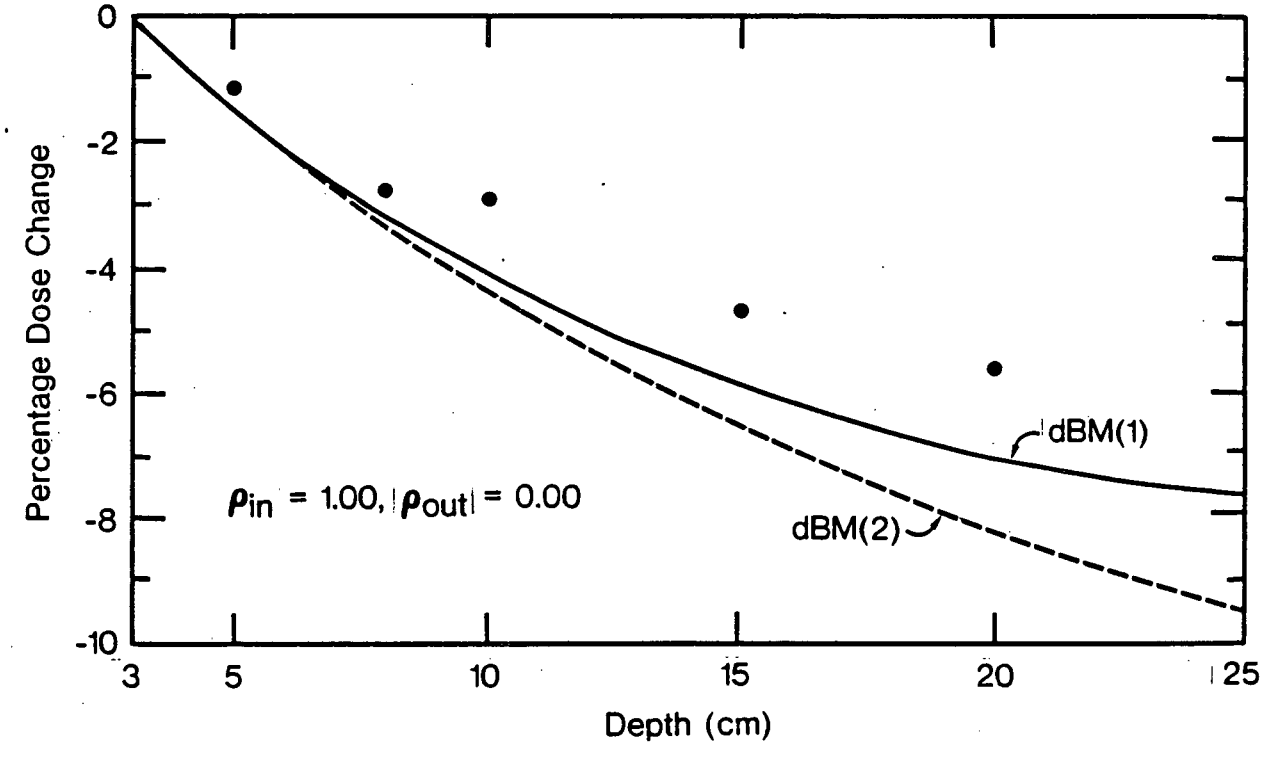

FIGURE 20b - dBM AND MEASURED RESULTS ($\rho_{in} = 1$, $\rho_{out} = 0$)

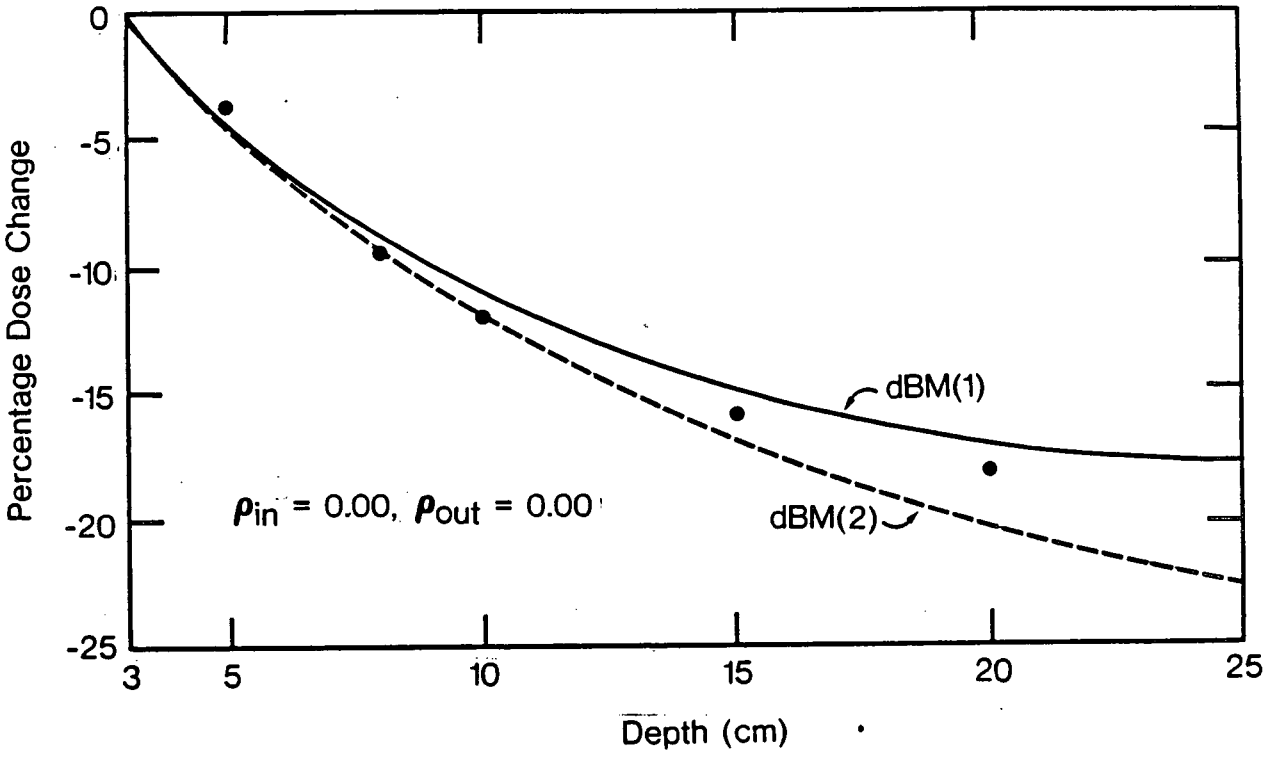

FIGURE 20c - dBM AND MEASURED RESULTS ($\rho_{in} = \rho_{out} = 0$)

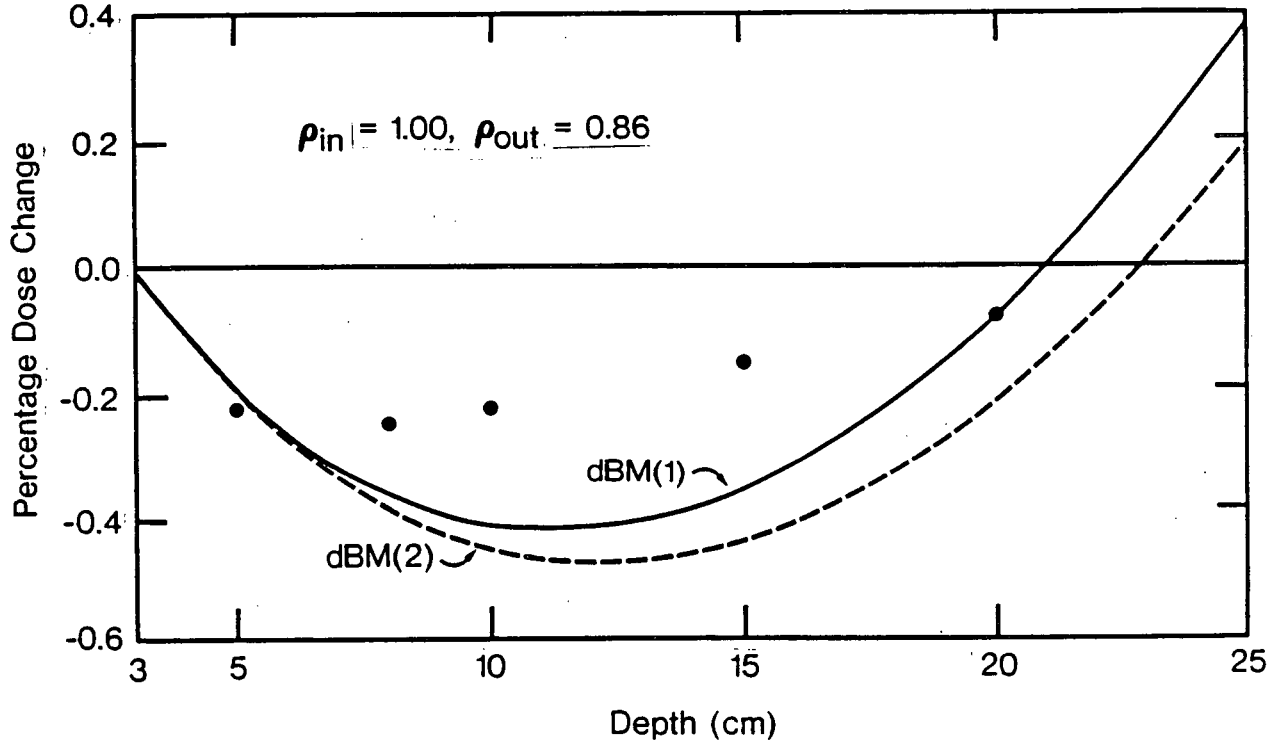

FIGURE 20d - dBM AND MEASURED RESULTS ($\rho_{in} = 1, \rho_{out} = 0.86$)

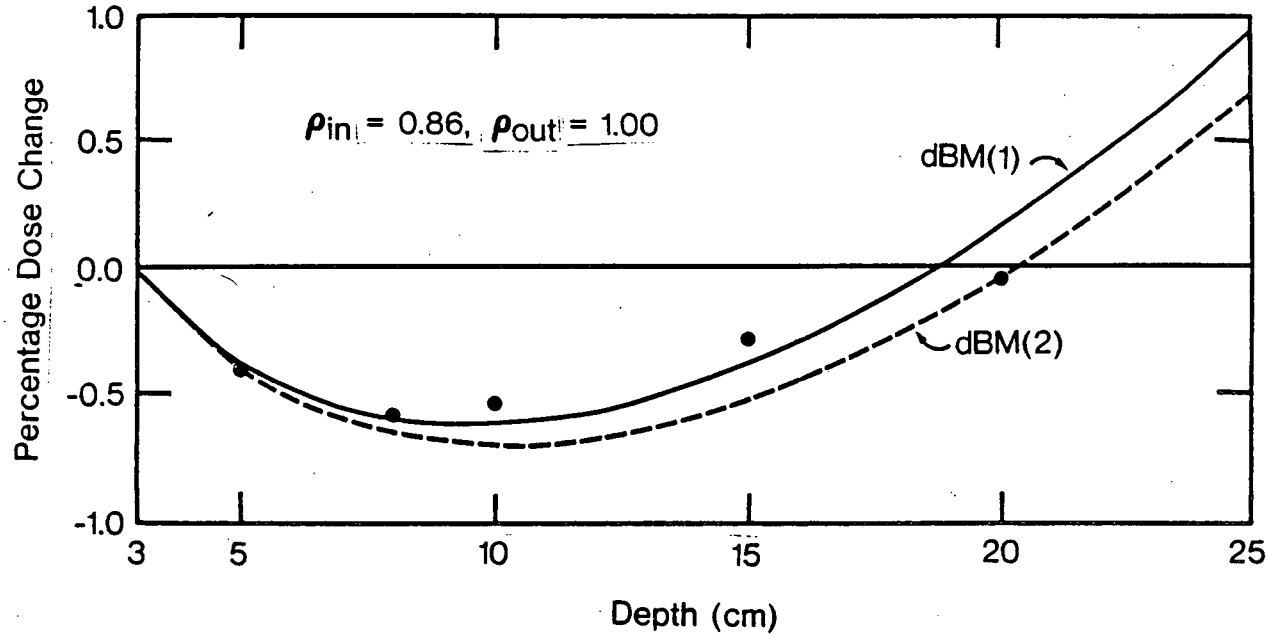

FIGURE 20e - dBM AND MEASURED RESULTS (ρ_{in} = 0.86, ρ_{out} = 1)

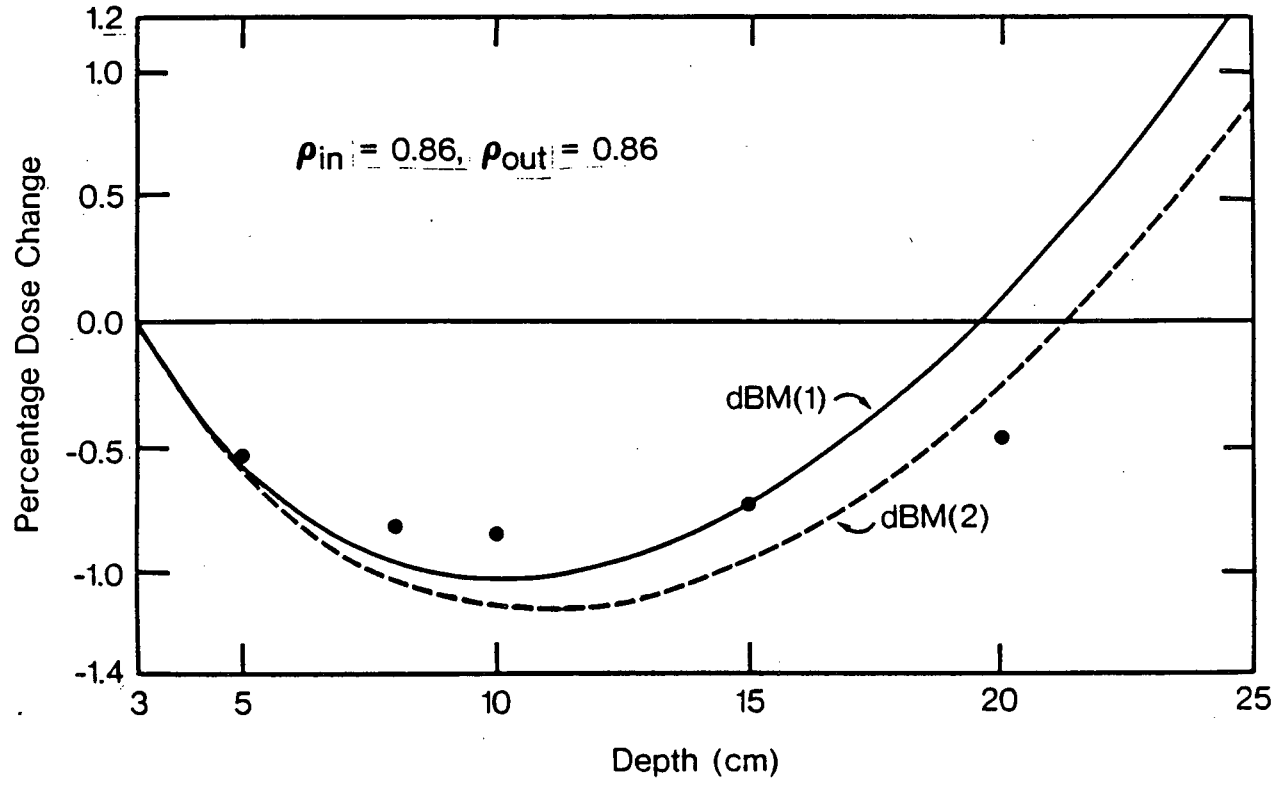

FIGURE 20f - dBM AND MEASURED RESULTS (ρ_{in} = ρ_{out} = 0.86)

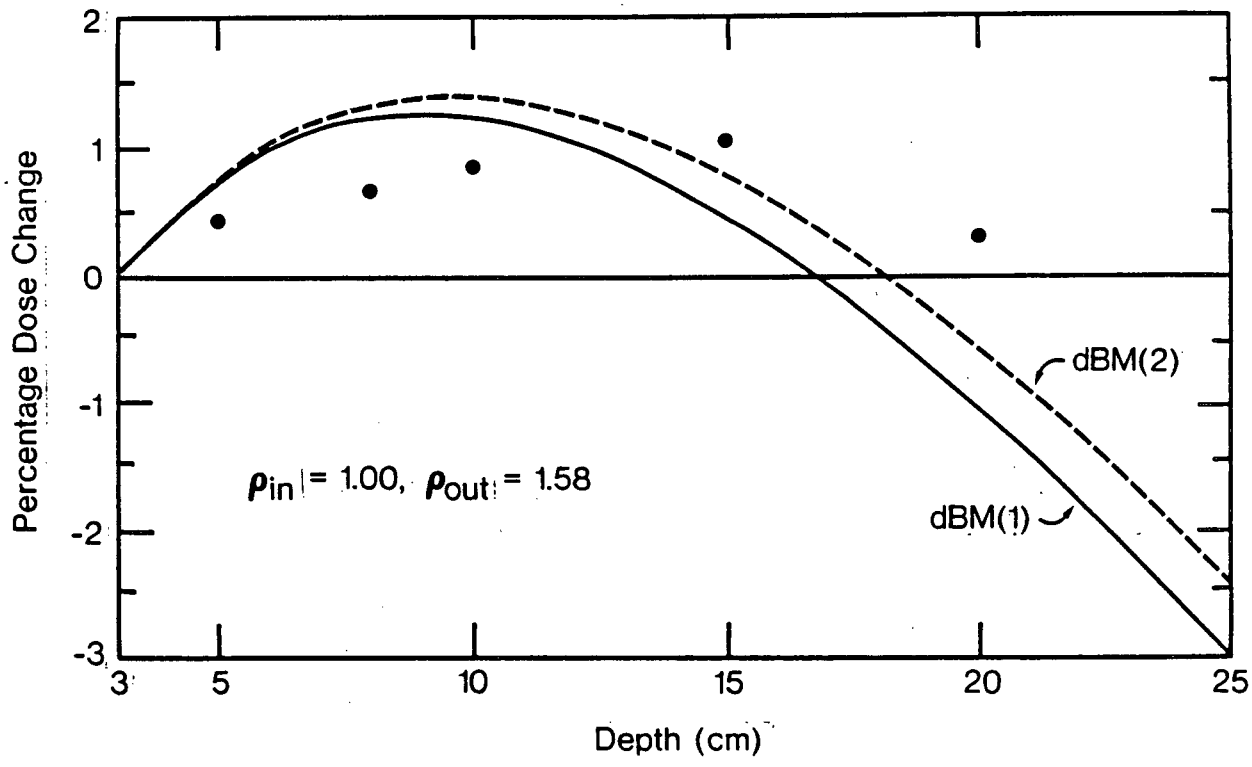

FIGURE 20g - dBM AND MEASURED RESULTS (ρ_{in} = 1, ρ_{out} = 1.58)

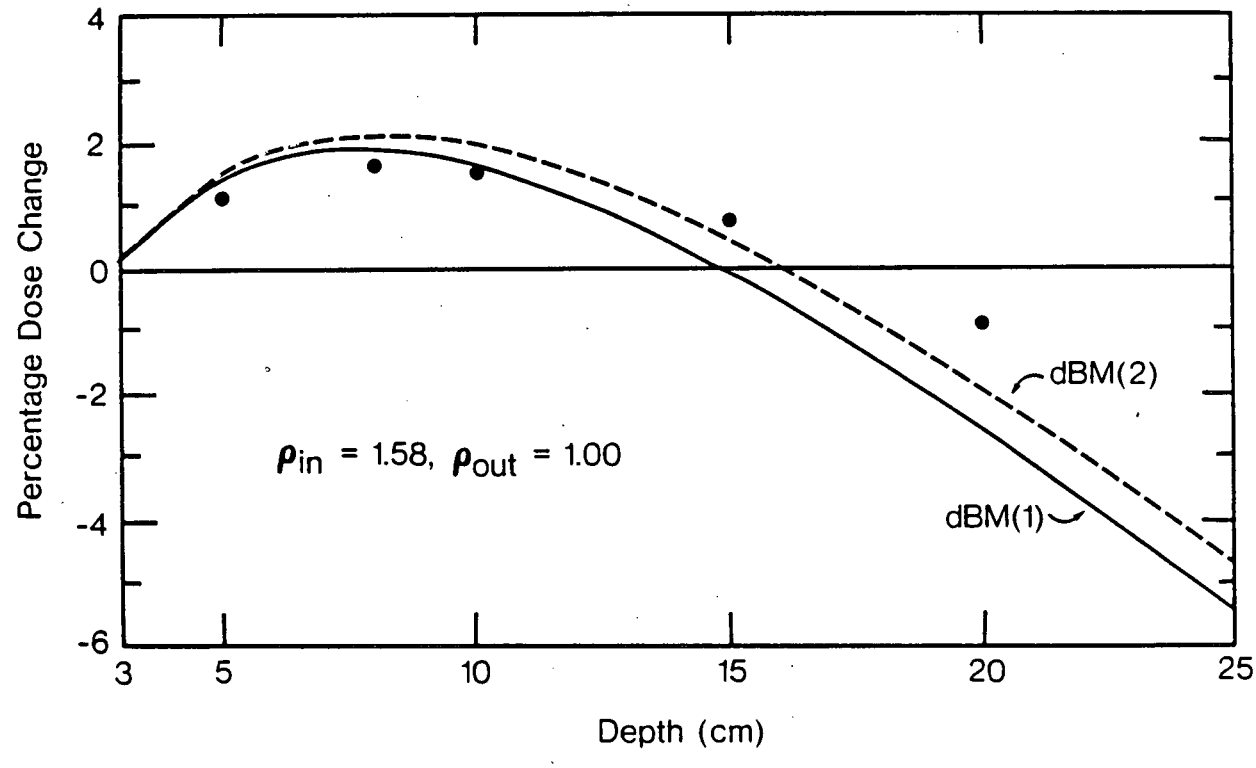

FIGURE 20h - dBM AND MEASURED RESULTS (ρ_{in} = 1.58, ρ_{out} = 1)

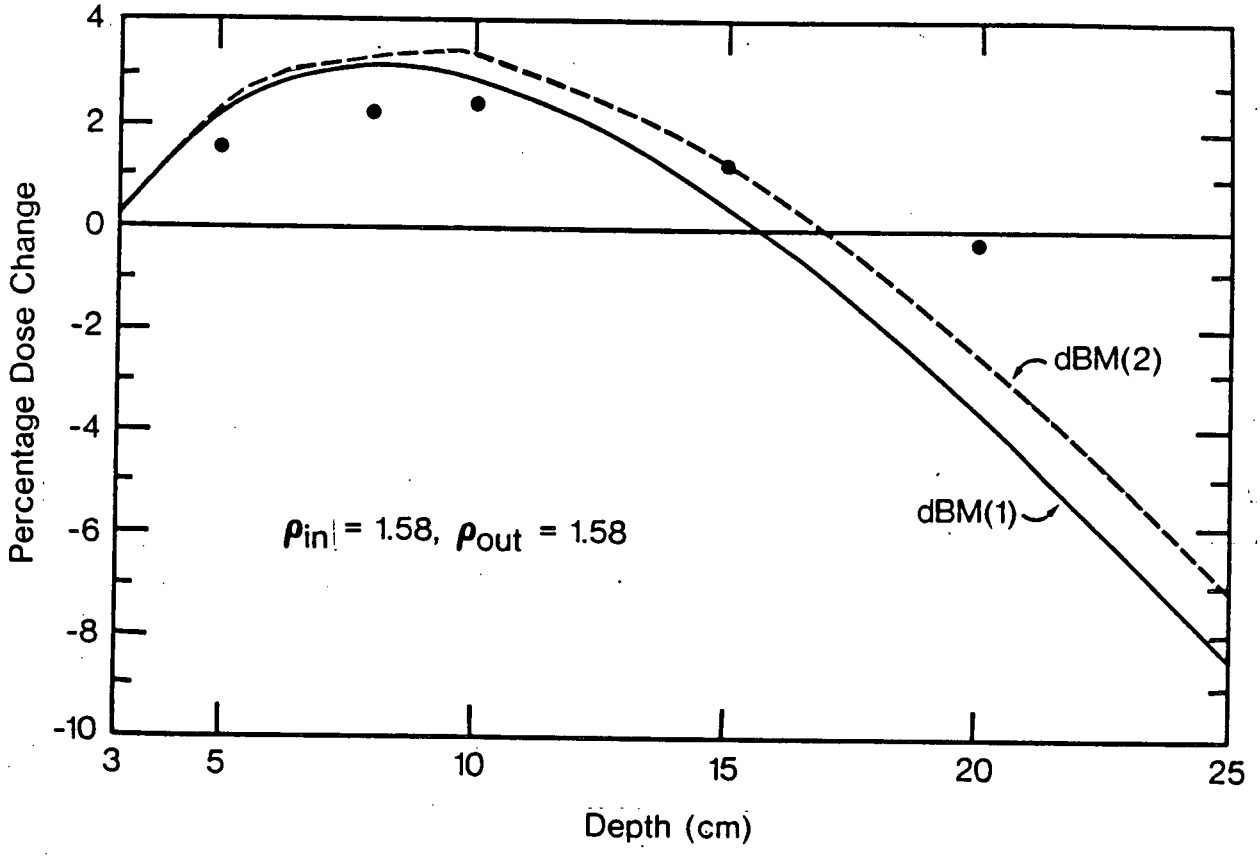

FIGURE 20i - dBM AND MEASURED RESULTS ($\rho_{in} = \rho_{out} = 1.58$)

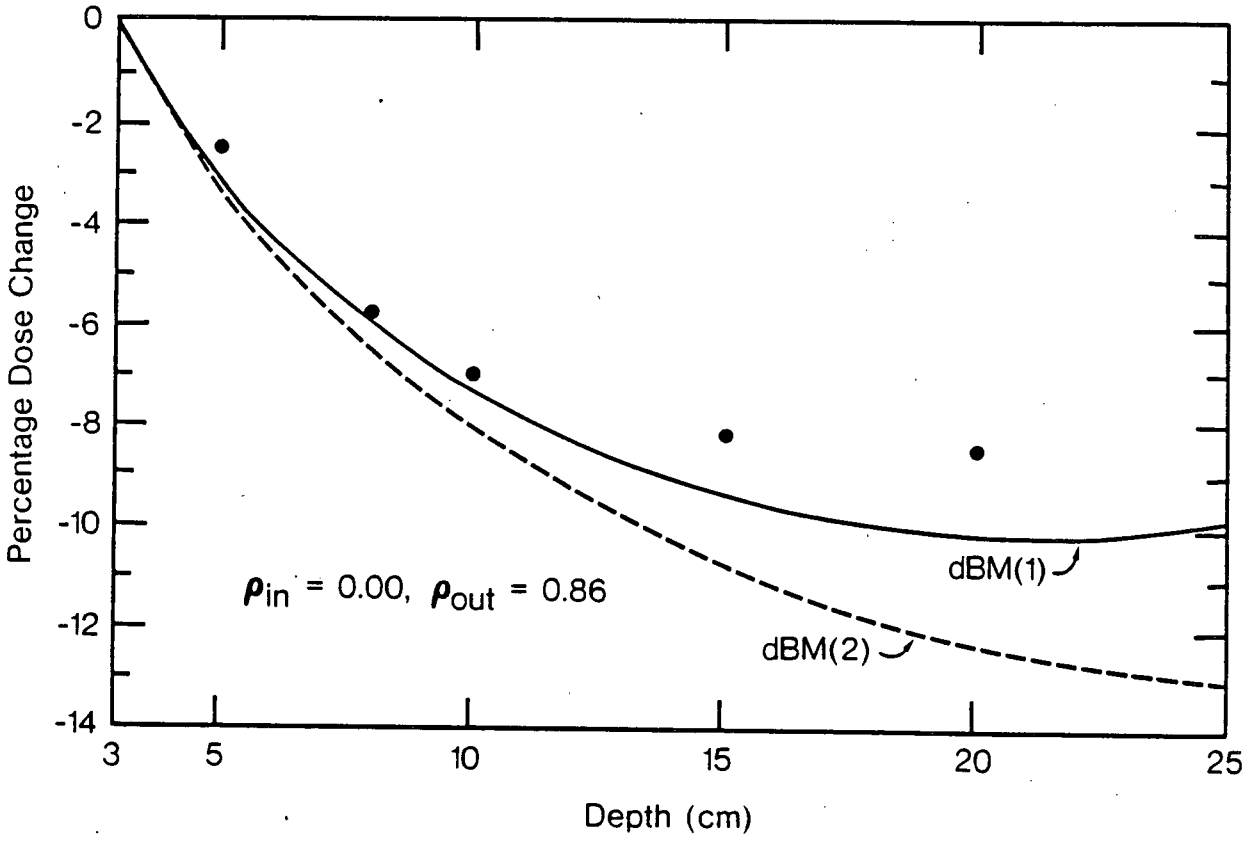

FIGURE 20j - dBM AND MEASURED RESULTS ($\rho_{in} = 0$, $\rho_{out} = 0.86$)

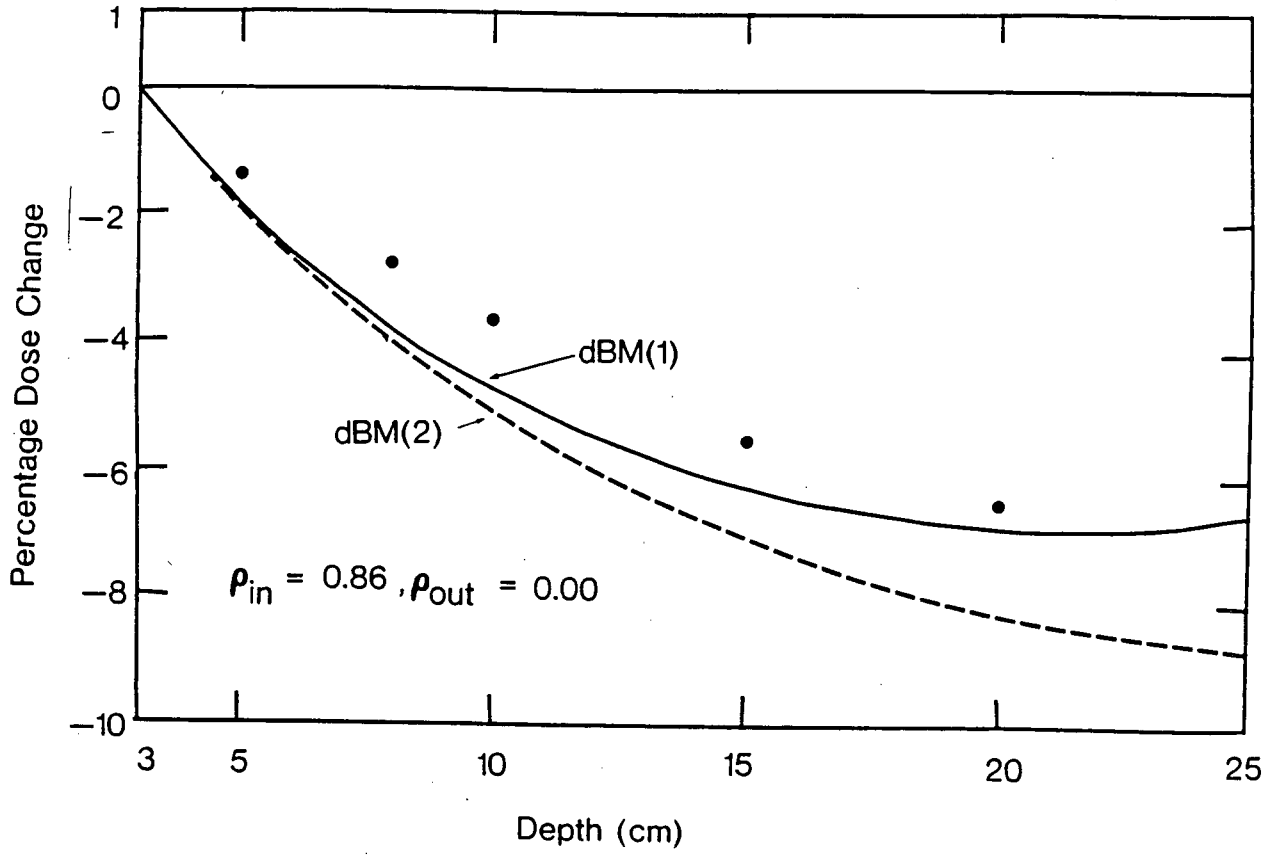

FIGURE 20k - dBM AND MEASURED RESULTS (ρ_{in} = 0.86, ρ_{out} = 0)

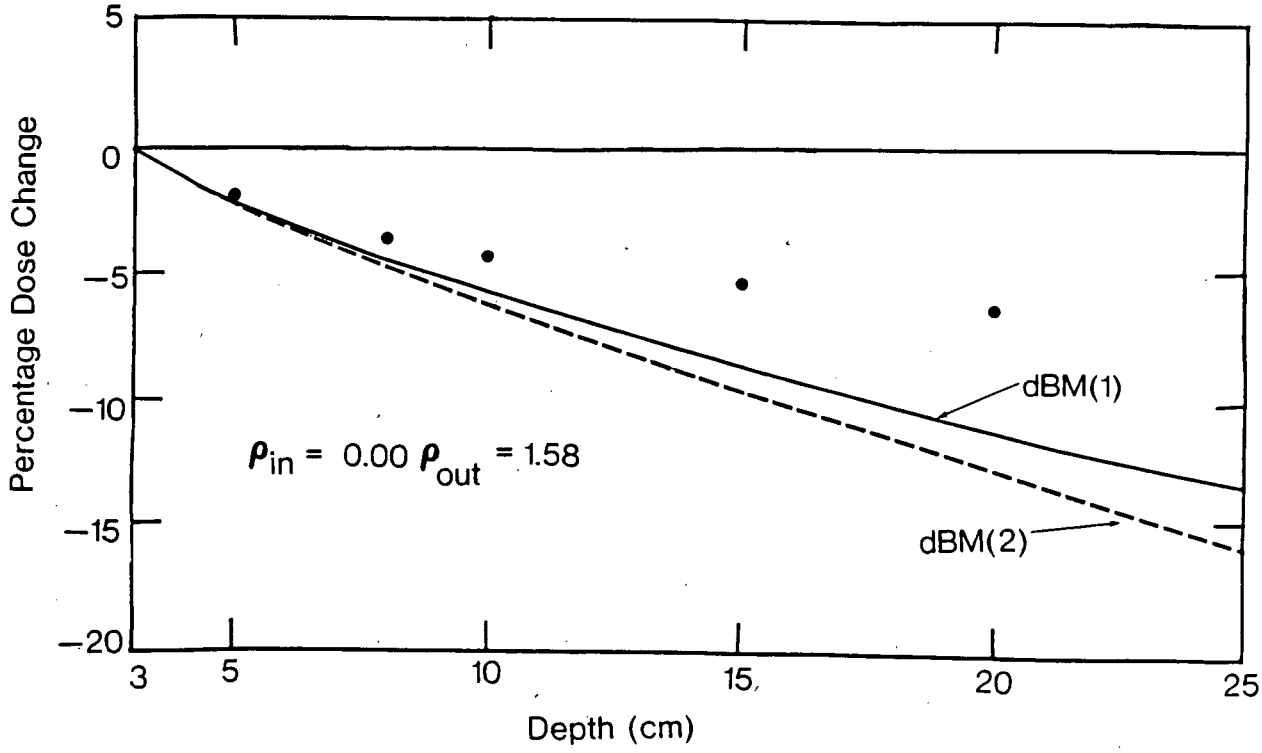

FIGURE 201 - dBM AND MEASURED RESULTS (ρ_{in} = 0, ρ_{out} = 1.58)

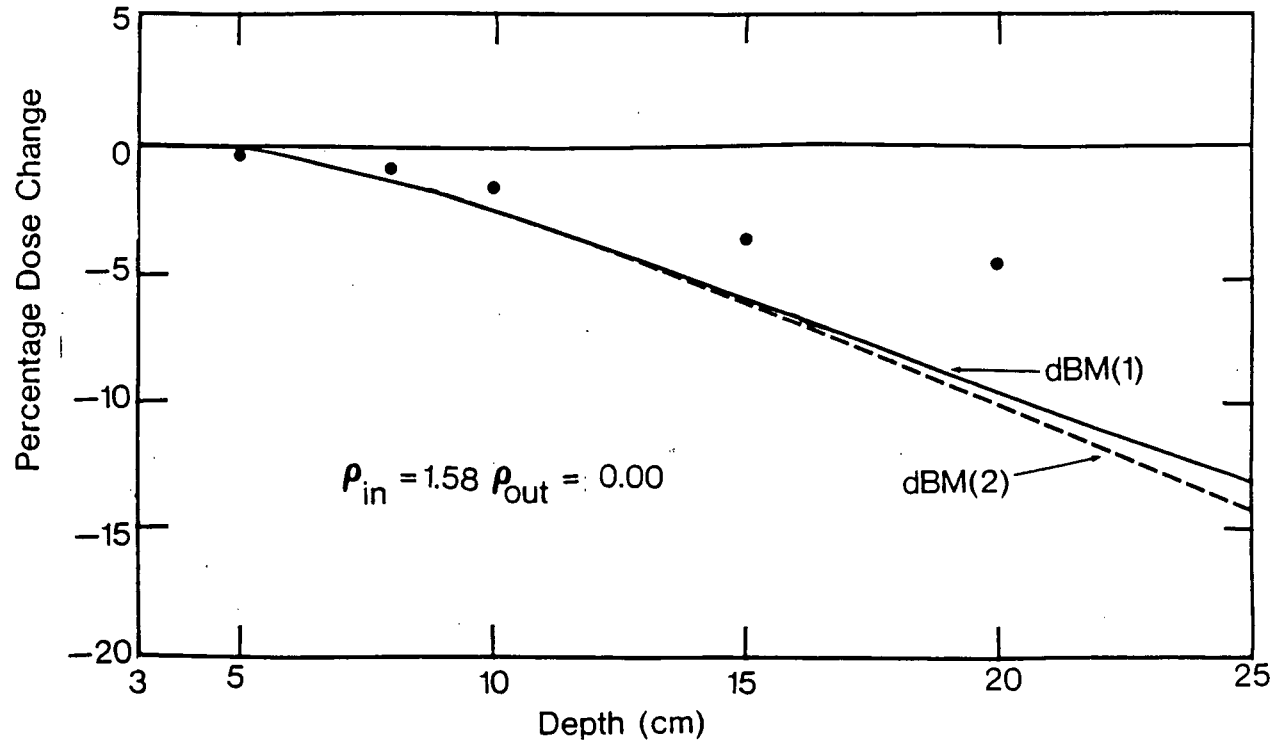

FIGURE 20m - dBM AND MEASURED RESULTS (ρ_{in} = 1.58, ρ_{out} = 0)

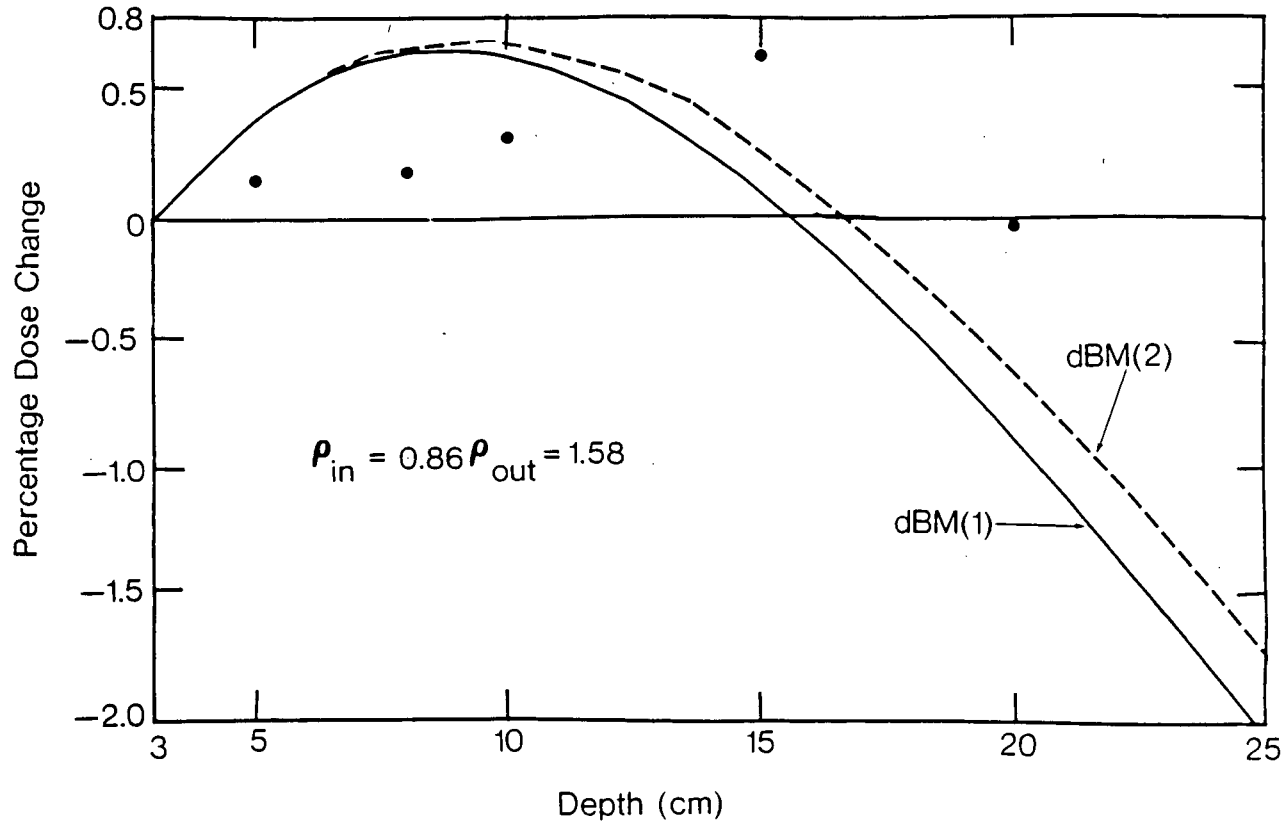

FIGURE 20n - dBM AND MEASURED RESULTS ($_{in}$ = 0.86, $_{out}$ = 1.58)

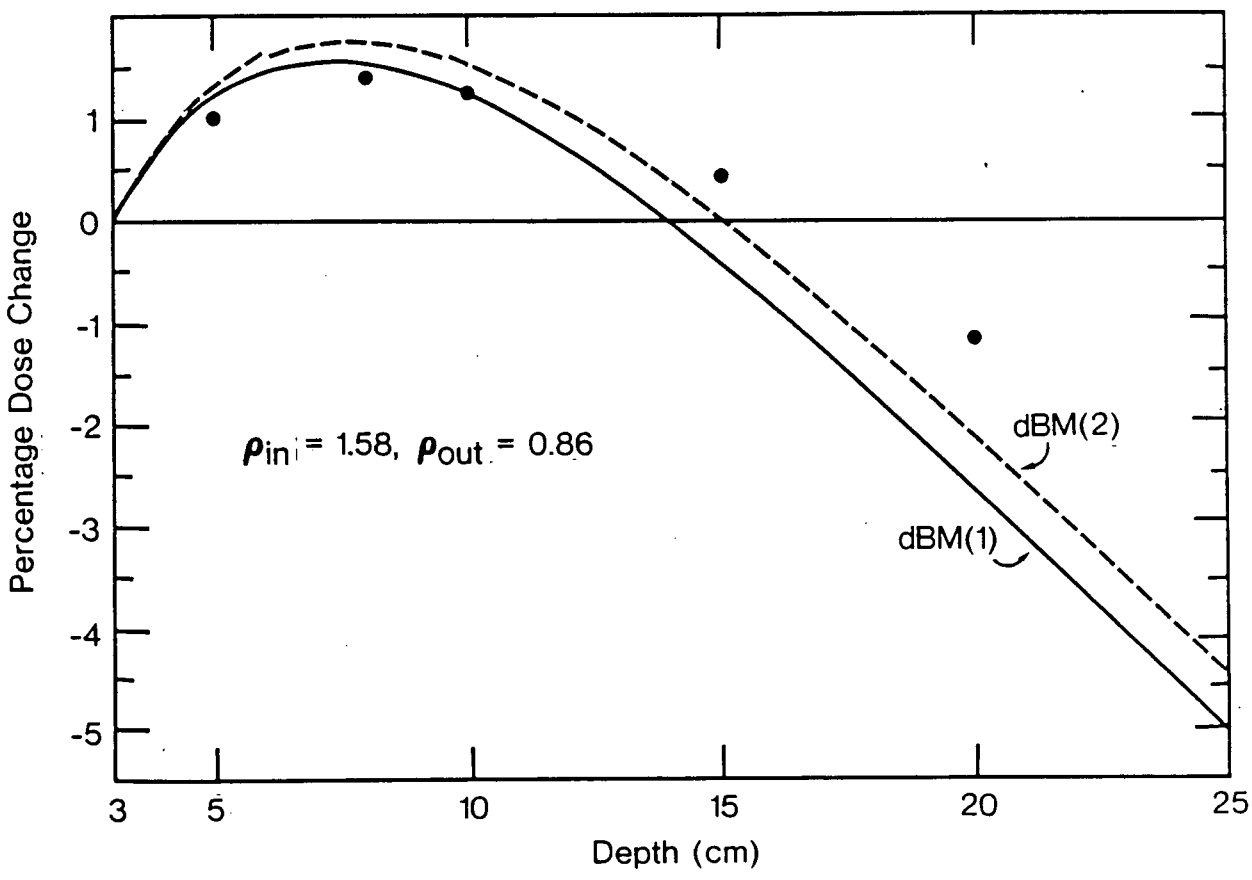

FIGURE 20o - dBM AND MEASURED RESULTS (ρ_{in} = 1.58, ρ_{out} = 0.86)

4.2.1.2 van de Geijn-PoCheng calculations

This calculation method was reviewed in section 2.3.2, which presented equation (7) to correct for the scatter perturbations due to a single thick cone. Equation (7) had to be modified, though, to account for the 2.5 cm slab of water above the cone,

$$CF_{VP} = 1 - [\ (TAR\ (\rho d, \rho r_i) / TAR\ (\rho d, \rho r_o)\ ]\ [\ 1 - \beta^{\alpha}] \qquad (7)$$

where,

$$\beta = TAR\ (\rho(d - 2.5\ cm),\ \rho r_i) / TAR\ (0.5\ cm,\ \rho r_i)$$

and,

$$\alpha = (1/\rho) - 1$$

To correct for the slab, equation (7) must be multiplied by a Batho correction factor,

$$CF_B = (\ TAR\ (\rho x, \rho r_o) / TAR\ (\rho d, \rho r_o))^{1 - \rho}$$

The modification of the van de Geijn-PoCheng calculation requires that the cone be of a single density and coincident with the field boundaries. In addition, it, like the dBM calculation, neglects the backscatter perturbations. These restrictions on this calculation method do not allow it to approach the versatility of the differential Batho method.

We have plotted the van de Geijn-PoCheng and the dBM calculations against depth for the two cases of both cones filled with K_2 HPO_4 solution and oil in figures (21a) and (21b). There is a reasonable qualitative agreement. Quantitatively, this calculation method also over-predicts the scatter effect, but more so than the dBM calcualtions. These two graphs show that the differential Batho method is a better representation of the measured data than that of van de Geijn and PoCheng.

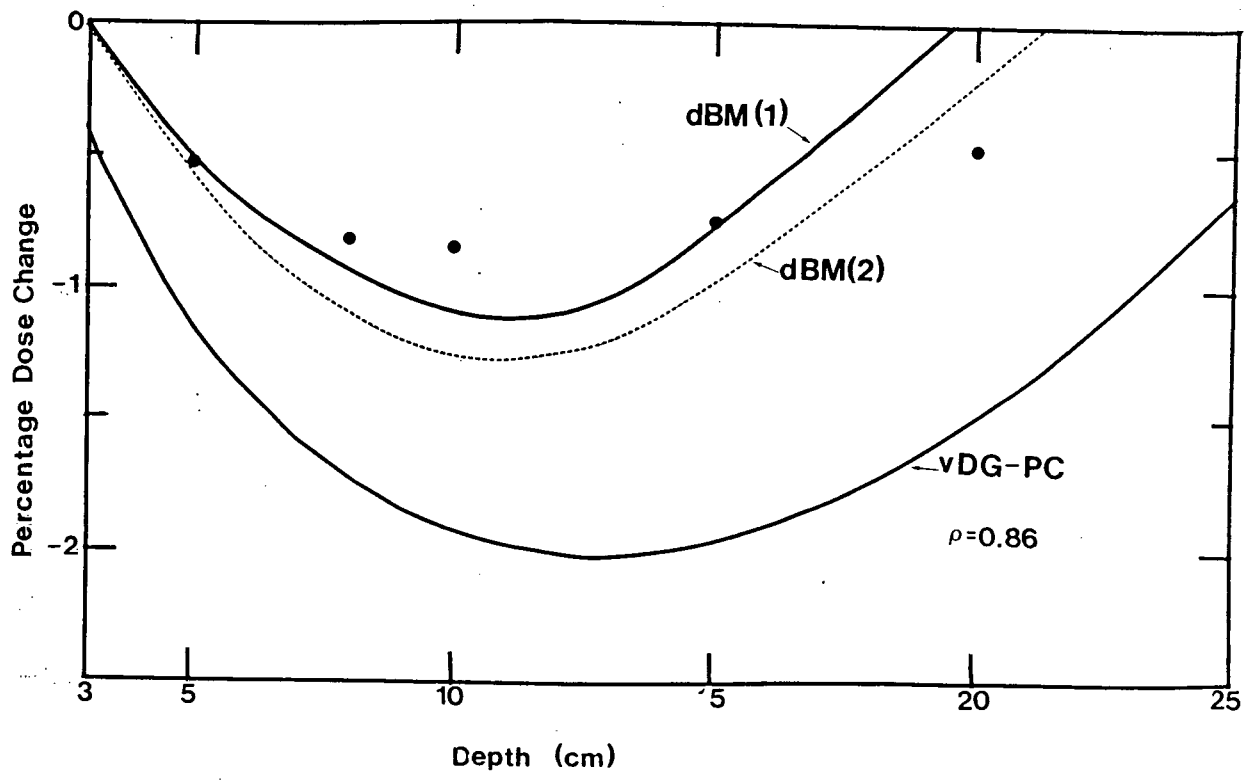

FIGURE 21a

COMPARISON OF dBM AND VAN DE GEIJN-PoCHENG CALCULATIONS WITH MEASUREMENTS FOR $\rho = 0.86$

(For figures 21a and 21b, the points are the smoothed data)

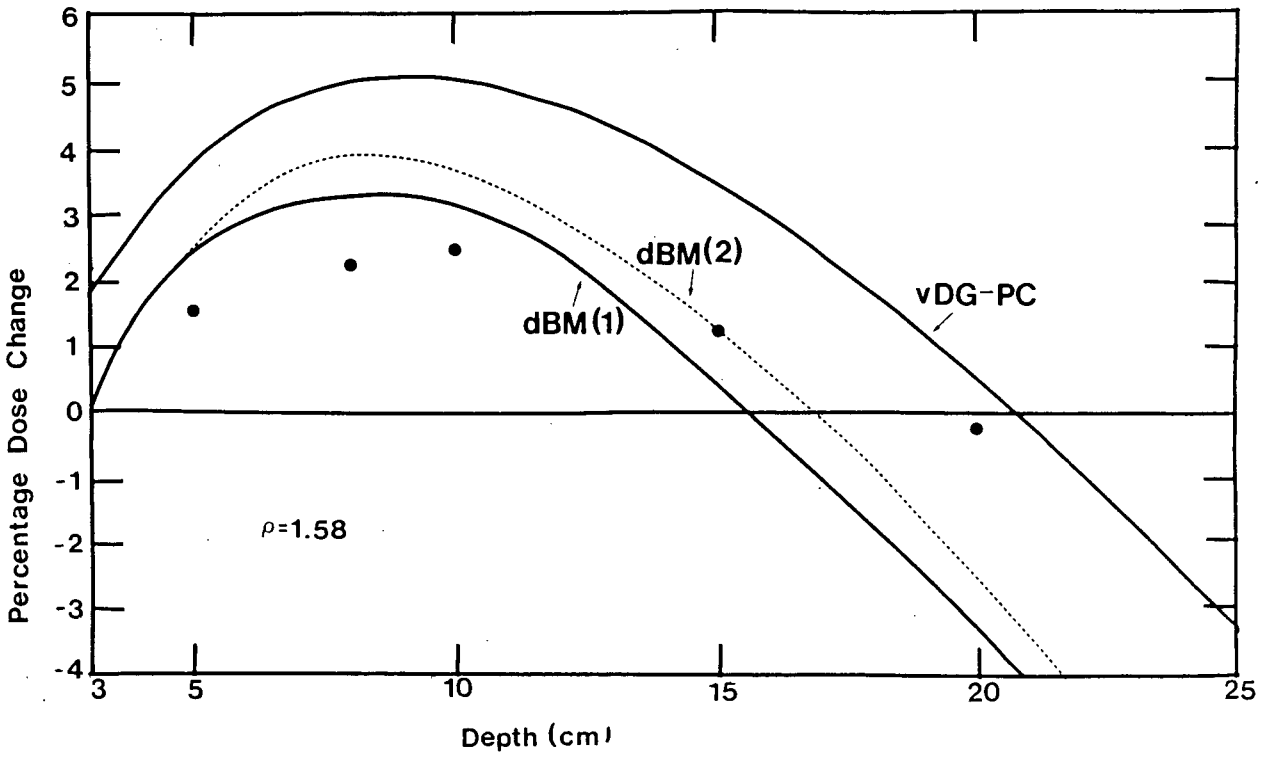

FIGURE 21b

COMPARISON OF dBM AND VAN DE GEIJN-PoCHENG CALCULATIONS WITH MEASUREMENTS FOR ρ = 1.58

4.3 Further considerations

The differential Batho method gives a reasonable account of the scatter effects due to a single conical inhomogeneity. For multiple conical inhomogeneities, the differential Batho method predicts the additivity of the effects. This was confirmed, for a wide number of cases, as given by the results in table VIII.

Unfortunately, there is no clear indication of which calculation type, dBM(1) or dBM(2), to use. We know that when the inhomogeneity extends beyond the field edge, the dBM(2) calculation offers a better representation of the scatter changes than does dBM(1). As the field increases beyond the inhomogeneity, the dBM(1) gives a better fit.

Consequently, we recommend two rules :

(1) Use dBM(1) when the inhomogeneity is completely within the field.

(2) Use dBM(2) when the outer edge of the inhomogeneity extends to the field edge or beyond.

On the basis of the findings presented in this thesis, the differential Batho method is applicable to treatment planning corrections for certain geometries found in clinical practice. In particular, if the inhomogeneity can be approximated by a single conical or annular segment, the application is straight-forward.

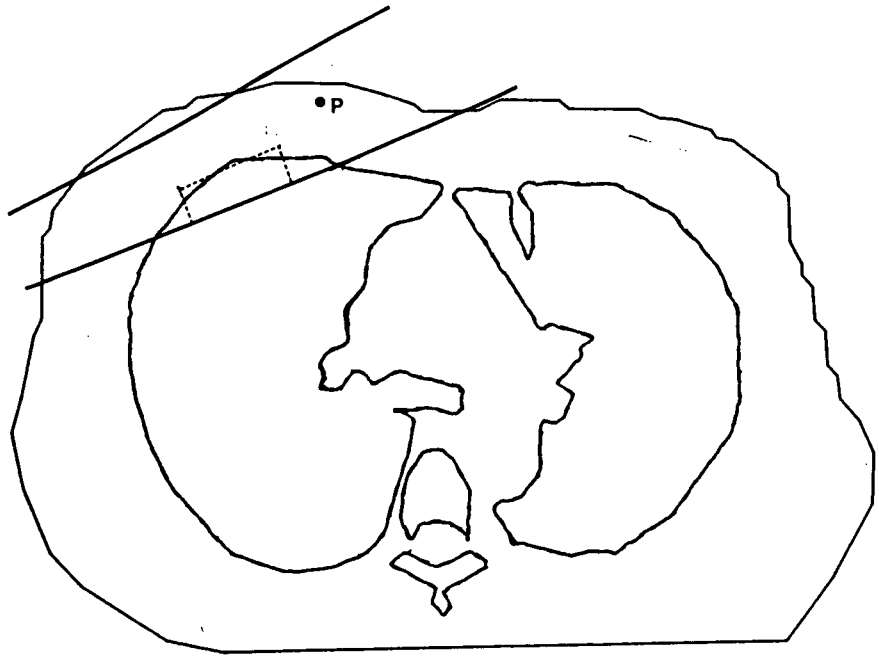

FIGURE 22

APPROXIMATION OF A LUNG INHOMOGENEITY BY A CONICAL SEGMENT

For example, consider the case of a section of lung in the beam, as in figure (22). This lung section can be approximated by the segment of a cone's frustum, shown by the dotted lines. The two shapes are considered to be equivalent provided that they have the same density, volume and centroid, and have similar elongations.

In order to extend the method to the complete treatment volume, one can consider the volume as made up of a suitable number of angular segments. For each segment, the procedure described above is carried out. The total correction factor is then evaluated by summing the effects over the angle θ,

$$CF = (2\pi)^{-1} \sum_{i=1}^{n} CF(\theta_i)\, \Delta\theta_i \qquad (8)$$

where $CF(\theta_i)$ is the correction factor for the i^{th} segment, with a width of $\Delta\theta_i$, at an angle θ_i.

A number of questions remain unanswered. It is still not known how good the differential Batho method is when applied to correct for anatomical structures. For example, two questions of clinical relevance are raised from the statements of the last two paragraphs. How good is the approximation of an anatomical inhomogeneity by a conical segment ? It would be of interest to know if inhomogeneities of certain sizes or densities may be neglected in order to simplify the calculations . Further, one would also be interested in knowing the effectiveness of representing the treatment volume by a series of

pie-shaped segments. For example, how many segments, i.e. the number n in equation (8), must be used to give a good representation ? We recommend that studies be performed with an anthropomorphic phantom (such as the RANDO phantom) in order to determine the clinical usefulness of the method. These studies would be confined to inhomogeneities with sizes and densities more representative of those encountered in practice. Consequently, one could test the goodness-of-fit between the differential Batho method and the measured data.

Another question to be answered more thoroughly is that of the effect of field size on which calculation type, dBM(1) or dBM(2), to use. Field size was not included as a variable in the original plan of this research and raised interest only during the course of the experiments. The one experiment in which field size was treated as a variable showed that the dBM(1) approximation was no longer a limit for field radii far greater than the outer radius of the inhomogeneity. Should a further modification be made to the rules on page 90 for such cases ?

5 CONCLUSIONS

In this thesis, we have shown that the effect of an inhomogeneity upon the scatter dose is a complicated function of geometry and electron density. This effect is not independent nor is it additive. Exact calculations of these effects are not feasible, so approximate methods must be used. Previous methods have provided reasonable dose corrections for the anatomical information available at the time. By the use of CT, and the increased anatomical knowledge it provides, more accurate dosimetry is possible.

We have proposed the differential Batho method, and have presented many supporting measurements. This method calculates the effects upon the central-axis scatter dose due to cone frustums or annuli symmetric about the central axis. It provides two expressions of these effects, dBM(1) and dBM(2). Both calculation types are for the same geometry, but consider differing scatter filtration conditions. Experimentally, we have shown that they essentially act as limits to the scatter perturbations, except when the field edge extends far beyond the inhomogeneity. This situation needs to be investigated further.

The differential Batho method implies the additivity of the effects of these symmetric inhomogeneities varying radially, even though we know that additivity is not a general feature of multiple inhomogeneities. Experimentally, however, we have shown that these non-linearities are minimized when the inhomogeneities vary radially.

The following further investigations are recommended :

(i) Examine, in more detail, the transition between the dBM(1) and dBM(2) calculations as a function of field size and depth to see if this phenomenon can be calculated from the theory or at least approximated empirically.

(ii) Determine if it is possible to modify the differential Batho method so as to calculate the effects when the field size is much larger than the inhomogeneity.

(iii) Although the approximate additivity and independence of the radially varying inhomogeneities have been shown for the one case when the outer surface the second cone is coincident with the field edge, further investigation is required to see how this result depends on the field size.

(iv) The major restriction of the differential Batho method in treatment planning is the requirement that anatomical inhomogeneities be approximated by sections of cones. The difficulties in representing the treatment volume in this way need to be examined further.

(v) Inhomogeneities varying with depth are difficult to correct for simply. Such configurations should be further studied.

REFERENCES

Batho, H.F., Theimer, O. and Theimer, R. : A consideration of the equivalent circle method of calculating depth doses for rectangular X-ray fields. J. Can. Assoc. Radiol. 7:51 (1956)

Batho, H.F. : Lung corrections in Cobalt 60 beam therapy. J. Can. Assoc. Radiol. 15:79 (1964)

Batho, H.F. : Relationships between exposure, kerma and absorbed dose in a medium exposed to megavoltage photons from an external source. Phys. Med. Biol. 13:355 (1968)

Battista, J.J. and Bronskill, M.J. : Compton-scatter tissue densitometry : calculation of single and multiple scatter photon fluences. Phys. Med. Biol. 23:1 (1978)

Battista, J.J., Rider, W.D. and van Dyk, J. : Computed tomography for radiotherapy planning. Int. J. Radiation Oncology Biol. Phys. 6:99 (1980)

Beaudoin, L., M.Sc. Thesis, University of Toronto, Toronto, Canada, 1968.

Bengtsson, L.G. : Dose average event size determination for ^{60}Co using precision measurements of ionization current. Proc. Third Symp. Microdosimetry, EUR 4810, 483 (1972)

Berger, M.J. and Spencer, L.V. : Some radiological applications of gamma-ray transport theory. Rad. Res. 10:552 (1959)

Brooks, R.A. and Di Chiro, G. : Principles of computer assisted tomography (CAT) in radiographic and radioisotopic imaging. Phys. Med. Biol. 21:689 (1976)

Bruce, W.R. and Johns, H.E. : The spectra of X rays scattered in low atomic number materials. Br. J. Radiol. Supp. 9 (1960)

Carlson, B. "The Monte Carlo Method Applied to a Problem in Gamma-Ray Diffusion", Los Alamos Scientific Laboratory AECU Report 2857, 1953.

Cashwell, E.D. and Everett, C.J. A Practical Manual on the Monte Carlo Method for Random Walk Problems. Pergammon Press, New York, 1959.

Clarkson, J.R. : A note on depth doses in fields of irregular shape. Br. J. Radiol. 14:265 (1941)

Cormack, A.M. : Early two-dimensional reconstruction and recent topics stemming from it. Med. Phys. 7:277 (1980)

Cunningham, J.R. : Scatter-air ratios. Phys. Med. Biol. 17:42 (1972)

Cunningham, J.R. and Beaudoin, L. : Calculations for tissue inhomogeneities with experimental verification. Proc. XIII International Congress of Radiology, Madrid, 653 (1973)

Emshoff, J.L. and Sisson, R.L. Design and Use of Computer Models. MacMillan Publishing Co., Inc., New York, 1970.

Geise, R.A. and McCullough, E.C. : The use of CT scanners in megavoltage photon-beam therapy planning. Radiology 124:133 (1977)

Goitein, M. : Computed tomography in planning radiation therapy. Int. J. Radiation Oncology Biol. Phys. 5:445 (1979)

Grodstein, G.W. "X-ray Attenuation Coefficients from 10 keV to 100 MeV", National Bureau of Standards Circular #583, Washington, D.C., 1957.

Hammersley, J.M. and Handscomb, D.C. Monte Carlo Methods. John Wiley and Sons, Co., New York, 1965.

Hounsfield, G.N. : Computed medical imaging. Med. Phys. 7:283 (1980)

ICRU Report # 18, "Specification of High-Activity Gamma-Ray Sources", International Commission on Radiation Units and Measurements, Washington, D.C., 1970.

ICRU Report # 23, "Measurement of Absorbed Dose in a Phantom Irradiated by a Single Beam of X or Gamma Rays", International Commission on Radiation Units and Measurements, Washington, D.C., 1973.

ICRU Report # 24, "Determination of Absorbed Dose in a Patient Irradiated by Beams of X or Gamma Rays in Radiotherapy Procedures", International Commission on Radiation Units and Measurements, Washington, D.C., 1976.

ICRU Report # 33, "Radiation Quantities and Units", International Commission on Radiation Units and Measurements, Washington, D.C., 1980.

Johns, H.E., Bruce, W.R. and Reid, W.B. : The dependence of depth dose on focal skin distance. Br. J. Radiol. 31:254 (1958)

McCullough, E.C. : Photon attenuation in computed tomography. Med. Phys. 2:307 (1975)

Morin, R.L., Raeside, D.E., Goin, J.E. and Widman, J.C. : Monte Carlo advice. Med. Phys. 6:305 (1979)

O'Connor, J.E. : The variations of scattered X-rays with density in an irradiated body. Phys. Med. Biol. 1:352 (1957)

Raeside, D.E. : Monte Carlo principles and applications. Phys. Med Biol. 21:181 (1976)

Roesch, W.C., "Mathematical Theory of Radiation Fields", in Radiation Dosimetry, Volume I. F.H. Attix, W.C. Roesch and E. Tochilin, eds. Academic Press, New York, 1968.

Rossi, H.H., "Microscopic Energy Distribution in Irradiated Matter", in Radiation Dosimetry, Volume I. F.H. Attix, W.C. Roesch and E. Tochilin, eds. Academic Press, New York, 1968.

Scrimger, J.W. and Cormack, D.V. : Spectrum of the radiation from a cobalt 60 teletherapy unit. Br. J. Radiol. 36:514 (1963)

Sidwell, J.M. Burlin, T.E. and Wheatley, B.M. : Calculations of the absorbed dose in a phantom from photon fluence and some applications to radiological protection. Br. J. Radiol. 42:522 (1969)

Sontag, M.R., Ph.D. Thesis, University of Toronto, Toronto, Canada, 1979.

Sontag, M.R. and Cunningham, J.R. : Clinical application of a CT based treatment planning system. Computerized Tomography 2:117 (1978a)

Sontag, M.R. and Cunningham, J.R. : The equivalent tissue-air ratio method for making absorbed dose calculations in a heterogeneous medium. Radiology 129:787 (1978b)

Soucek, B. Minicomputers in Data Processing and Simulation. John Wiley and Sons, Co., New York, 1972.

Stewart, J.R., Hicks, J.A., Boone, M.L.M. and Simpson, L.D. : Computed tomography in radiation therapy. Int. J. Radiation Oncology Biol. Phys. 4:313 (1978)

van de Geijn, J. and PoCheng, C. : Generalization of the power law method to include inhomogeneities of smaller than beam cross-section. (Abstract). Med. Phys. 7:428 (1980)

van Dyk, J., Battista, J.J. and Rider, W.D. : Half body radiotherapy : the use of computed tomography to determine the dose to lung. Int. J. Radiation Oncology Biol. Phys. 6:463 (1980)

Walpole, R.E. and Myers, R.H. Probability and Statistics for Engineers and Scientists. MacMIllan Publishing Co., Inc., New York, 1972.

Webb S. and Parker, R.P. : A Monte Carlo study of the interaction of external beam X-radiation with inhomogeneous media. Phys. Med. Biol. 23:1043 (1978)

Webb, S. and Fox, R.A. : Verification by Monte Carlo methods of a power law tissue-air ratio algorithm for inhomogeneity corrections in photon beam dose calculations. Phys. Med. Biol. 25:225 (1980)

White, D.R. : Tissue substitutes in experimental radiation physics. Med. Phys. 5:467 (1978)

Wong, J.W., Henkelman, R.M., Fenster, A. and Johns, H.E. : Second scatter contribution to dose in a Cobalt-60 beam. Med. Phys. (in press, 1981a)

Wong, J.W., Henkelman, R.M., Andrew, J.W., van Dyk, J. and Johns, H.E. : Effect of small inhomogeneities on dose in a Cobalt-60 beam. Med. Phys. (in press, 1981b)

Young, M.E.J. and Gaylord, J.D. : Experimental tests of corrections for tissue inhomogeneities in radiotherapy. Br. J. Radiol. 43:349 (1970)

Yuen, K., Cancer Control Agency of British Columbia : Personal communication (1980)

APPENDIX A MONTE CARLO SIMULATION OF PHOTON TRANSPORT

A-1 Introduction

The stochastic model (Monte Carlo) enables one to determine the components of a photon beam more effectively than any analytical technique [Berger and Spencer, 1959; Roesch, 1968]. However, the stochastic model has the disadvantage of needing large numbers of samples (photons) for a statistically valid result. This will require a correspondingly large amount of computer time. Despite this shortcoming, Monte Carlo has been successfully applied to radiological problems [Battista and Bronskill, 1978; Bruce and Johns, 1960; Sidwell, et. al., 1969; Webb and Fox, 1980; Webb and Parker, 1978].

This appendix describes the Monte Carlo technique as it was used in this thesis.

A-2 The Monte Carlo technique

The underlying principle of the Monte Carlo technique is random sampling. Each random physical process is associated with a probability density function and a cumulative density function. Both functions can either be known or approximated. By drawing random samples of these functions, one forms a statistical approximation of the process [Emshoff and Sisson, 1970; Raeside, 1976].

The probability density function is,

$$f(x) = Pr\ (X = x) \qquad (A1)$$

where X is the random variable. The cumulative density function is,

$$F(x) = Pr\ (X \leq x)$$
$$= \int_{-\infty}^{X} f(t)\ dt \qquad (A2)$$

where $F(x)\ \varepsilon\ [0,1]$.

This integral can be equated to a random number, ξ, taken from a collection uniformly distributed along the unit interval. Then the value of the random variable associated with ξ can be found by inverting equation (A2),

$$x = F^{-1}\ (\xi) \qquad (A3)$$

By applying equation (A3) to a large group of ξ's, a statistical approximation of X is obtained.

A-3 Random number generators

Using the Monte Carlo method with a computer requires a determinisitc generator to yield random numbers uniformly distributed along the unit interval. The most effective generator is that using the congruence (or residue) method [Soucek, 1972]. Here, the (i + 1)-th random number in a sequence is generated by the algorithm,

$$\xi_{i+1} = (\lambda\ \xi_i + \eta) \bmod P \qquad (A4)$$

The result of this equation is divided by (P - 1) to give a number between zero and one.

We have used the IBM RANDU subroutine which sets the parameters in equation (A4) to $\lambda = 2^{16} + 3$, $\eta = 0$ and $P = 2^{31}$. Morin, et.al. [1979], report that the sequence generated by this subroutine has a cycle period in excess of 10^7. We further tested the subroutine using a chi-square test to determine its randomness.

A sequence of one million random single digit integers (0,1,2,...9) was generated using RANDU on a Data General ECLIPSE S-200 minicomputer. A goodness-of-fit test between the observed frequency of an integer (f_i) and the expected frequency ($E = 10^6 / 10 = 10^5$) is,

$$\chi_f^2 = E^{-1} \sum_{i=0}^{9} (f_i - E)^2$$

χ_f^2 is a chi-square statistic with nine degrees of freedom and was found to be equal to 4.652. This was less than the critical value (for a 5 % level of significance) of 16.919. We thus accepted the hypothesis that the sequence was uniformly distributed.

A-4 Monte Carlo simulation of photon transport

A-4.1 Photon trajectories

If a photon within a medium undergoes Compton scattering, its trajectory length will be a function of both the photon's energy and the electron density of the medium. The cumulative density function for a photon travelling a distance x is [Hammersley and Handscomb, 1965],

$$F(x) = 1 - e^{-\mu(E)\rho x} \qquad (A5)$$

where $\mu(E)$ is the linear attenuation coefficient for a photon of energy E in water and ρ is the relative electron density of the medium. $F(x)$ can be set equal to the random number ξ. Then the distance travelled is found by inverting equation (A5),

$$\begin{aligned} x &= -(\mu(E)\ \rho)^{-1}\ \ln\ (1 - \xi) \\ &= -(\mu(E)\ \rho)^{-1}\ \ln\ (\xi) \end{aligned} \qquad (A6)$$

where the quantity $(1 - \xi)$ has been substituted by the equally random ξ. This is the trajectory length in a homogeneous medium. If the photon crosses the interface between two media with different electron densities, as in figure (A-1), equation (A6) must be modified.

The trajectory of the photon in figure (A-1) begins in medium 1 and enters medium 2, a distance L away. The length travelled in medium 1

will be given by equation (A6). If this distance is greater than L, i.e., the photon crosses into medium 2, the trajectory length is altered. Because equation (A5) is Markovian, this new distance travelled will be,

$$d = L - (\rho_1 / \rho_2) \cdot L - (\mu(e)\ \rho_2)^{-1} \ln \xi \qquad (A7)$$

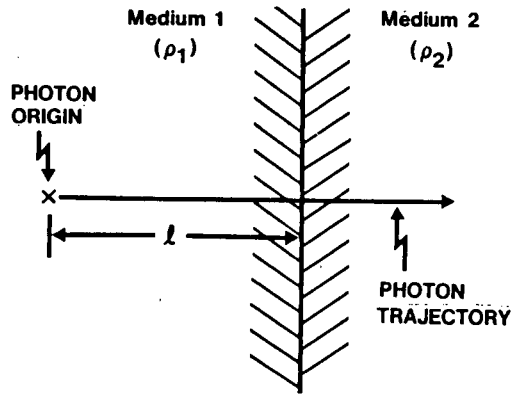

FIGURE A-1

PHOTON TRAJECTORY CROSSING THE INTERFACE BETWEEN TWO MEDIA

This equation can be applied sequentially as the photon crosses more interfaces. Now the interaction that occurs at the end of the trajectory must be considered.

A-4.2 Photon interactions

The predominant photon-electron interaction for ^{60}Co photons is Compton scattering. As the photon energy decreases, the photoelectric effect occurs with increasing probability. Pair production and photonuclear reactions require higher energy thresholds and their cross sections are negligible at ^{60}Co photon energies [Grodstein, 1957]. Classical scatter causes no ionization and is neglected for this study.

A decision is made by the Monte Carlo routine as to whether or not a photoelectric event occurs on the basis of the ratio of the photoelectric to the total cross-sections (σ_τ / σ_T) for water. For a particular energy, this ratio is determined and compared to the unit-interval random variable, ξ. If $\xi < (\sigma_\tau / \sigma_T)$, the photon is assumed to be absorbed. An electron, with a kinetic energy approximately that of the incident photon, is ejected. On the other hand, if $\xi > (\sigma_\tau / \sigma_T)$, a Compton scatter occurs.

When a photon with energy E undergoes a Compton scatter, it is deflected from its trajectory by an angle ϕ to an energy E' given by the Compton relation,

$$E' = E\,(1 + \alpha(1 - \cos\phi))^{-1} \qquad \text{(A8)}$$

where α is E normalized to the electron rest mass of 0.511 MeV. The recoil electron has a kinetic energy (E - E'). In a Monte Carlo simulation, E' is generated and the scattering angle ϕ calculated from (A8).

Cashwell and Everett [1959] outlined how E' can be generated. The probability that a photon is scattered from E to E' is,

$$Pr(E \rightarrow E') = \int_{E'}^{E} \frac{(d\sigma/dE)}{\sigma(E)}\, dE \qquad (A9)$$

where $(d\sigma/dE)$ is the differential cross section for a photon being scattered from E to E' and $\sigma(E)$ is the total Klein-Nishina cross section. This integral can be set equal to ξ and inverted to generate E'. Carlson [1953] did this numerically to yield,

$$E' = E\,(1 + s\xi + (2E - s)\,\xi^3)^{-1} \qquad (A10)$$

where,

$$s = E / (1 + 0.5625\ E)$$

and E and E' are normalized to 0.511 MeV. This approximation is good for incident photon energies below 2 MeV.

The scattered photon trajectory can be calculated [Cashwell and Everett, 1959] from the direction cosines of the incident trajectory (u,v,w), the Compton scattering angle ϕ and a random azimuthal scattering angle θ (= $2\pi\xi$). The scattered photon trajectory's direction

cosines are,

$$u' = b\,(cwu - dv)\,(1 - w^2)^{-\frac{1}{2}} + au$$
$$v' = b\,(cwv - du)\,(1 - w^2)^{-\frac{1}{2}} + av$$
$$w' = -\,bc\,(1 - w^2)^{\frac{1}{2}} + aw \qquad \text{(A11)}$$

where $a = \cos\phi$, $b = \sin\phi$, $c = \cos\theta$ and $d = \sin\theta$.

A-5 Monte Carlo simulation of a ^{60}Co beam in a water phantom

We developed a Monte Carlo routine, HMONTE, to run on a Data General ECLIPSE S-200 minicomputer. HMONTE simulates a cubic water phantom exposed to ^{60}Co gamma radiation.

A-5.1 Geometry

The medium used in the Monte Carlo model is assumed to be a water phantom (40 X 40 X 40) cc in volume irradiated by a circular ^{60}Co field.

The phantom is divided into 60,840 voxels : 39 along the two axes normal to, and 40 along, the central axis. Each voxel is 1.052 cc in volume and assumed to weigh 1.052 gm. The origin of the coordinate

system and the field are set at the middle of the phantom surface. For a photon fluence uniformly distributed over a unit area, the initial point of a photon on the surface is,

$$x_o = \xi_1^{\frac{1}{2}} R_{FS} \cos(2\pi\xi_2)$$
$$y_o = \xi_1^{\frac{1}{2}} R_{FS} \sin(2\pi\xi_2)$$
$$z_o = 0$$

where R_{FS} is the field radius at the surface and $\xi_{1,2}$ are two different random numbers. The initial direction cosines will be,

$$u_o = x_o / S \qquad v_o = y_o / S \qquad w_o = SSD / S$$

where,

$$S = (x_o^2 + y_o^2 + SSD^2)^{\frac{1}{2}}$$

and SSD is the source-surface distance.

A-5.2 Energy deposition

At each photon-electron interaction, the photon deposits energy as an electron with kinetic energy. This deposition can be described in terms of either the kerma or the absorbed dose. The dose and kerma are equal only at the build-up depth. However, at ^{60}Co energies, we can assume that the kerma and dose are equal to within 0.5 % beyond the build-up depth [Batho, 1968].

Assuming that the kerma and dose are equal simplifies the model. From the simulation of photoelectric and Compton events, the kerma is directly obtained. Determining the dose would require tracking the trajectories of the released electrons and calculating their energy losses along these paths. As the mean trajectory length of an electron set in motion by a ^{60}Co photon is 0.5 cm, the kerma and dose can be equated due to the large voxel size used.

A-5.3 Energy spectrum of the ^{60}Co source

A decaying ^{60}Co nucleus emits two photons with energies of 1.17 and 1.33 MeV, which can be averaged to 1.25 MeV. However, it is not acceptable to consider the energy spectrum of a cobalt therapy machine to be monoenergetic with this energy. Scatter from within the source, treatment head and collimator will contaminate the spectrum.

Measurements of the scatter from a therapy source have shown the scatter spectrum to be roughly uniform below 1.25 MeV with a slight peak at 0.2 MeV [ICRU, 1970; Scrimger and Cormack, 1963]. An energy spectrum of 80 % at 1.25 MeV and 20 % uniformly distributed from 0.1 to 1.25 Mev is assumed here.

A-5.2 Monte Carlo program (HMONTE)

This Monte Carlo routine's function is to generate the kerma components in each of the forty voxels along the central axis for a specified field

radius and SSD. All of the empirical data required for the program (reaction cross sections and attenuation coefficients) are stored in arrays and values determined using linear interpolation.

A set number of photons is used in each simulation with each photon history being followed sequentially. If a photoelectric event occurs in a central-axis voxel, the electron's kinetic energy is assumed to be deposited entirely within that volume and recorded. The photon history is terminated at that point. If the event occurs off axis, the energy is not recorded and the history terminated.

If a Compton scatter takes place in a central-axis voxel, the kerma due to the recoil electron is recorded and the photon followed. If the scatter does not occur on the axis, the kerma is not recorded but the photon is still tracked. Hence, a photon history is terminated only after a photoelectric event or if the photon is scattered out of the phantom.

The calculation rate for the HMONTE program was 45 photons per second.

APPENDIX B THE DIFFERENTIAL BATHO METHOD

B-1 Introduction

Yuen, of the Cancer Control Agency of British Columbia, has derived a method [1980] for calculating the change in the central-axis scatter dose due to an annulus. He has based it upon the Batho method [Batho, 1964] and has called it the differential Batho method.

B-2 Derivation

Consider a point 'P' in a water phantom, as in figure (B-1), at a depth d in a circular field of radius r_i. A slab inhomogeneity, infinite in lateral extent, is present with a relative electron density ρ. The dose at 'P', normalized to the dose at the same point in a phantom small enough to ensure maximum buildup, is given by the Batho method as,

$$D_{IP1} = TAR\ (d, r_i)\ CF\ (r_i) \qquad (B1)$$

where the correction factor is,

$$CF\ (r) = [\ TAR\ (x,r)\ /\ TAR\ (x + \Delta x, r)\ ]^{1-\rho} \qquad (B2)$$

The dose at 'P' in the homogeneous phantom, D_{HP1}, is the tissue-air ratio for 'P'. The change in the total dose caused by the slab will be the difference between these two doses,

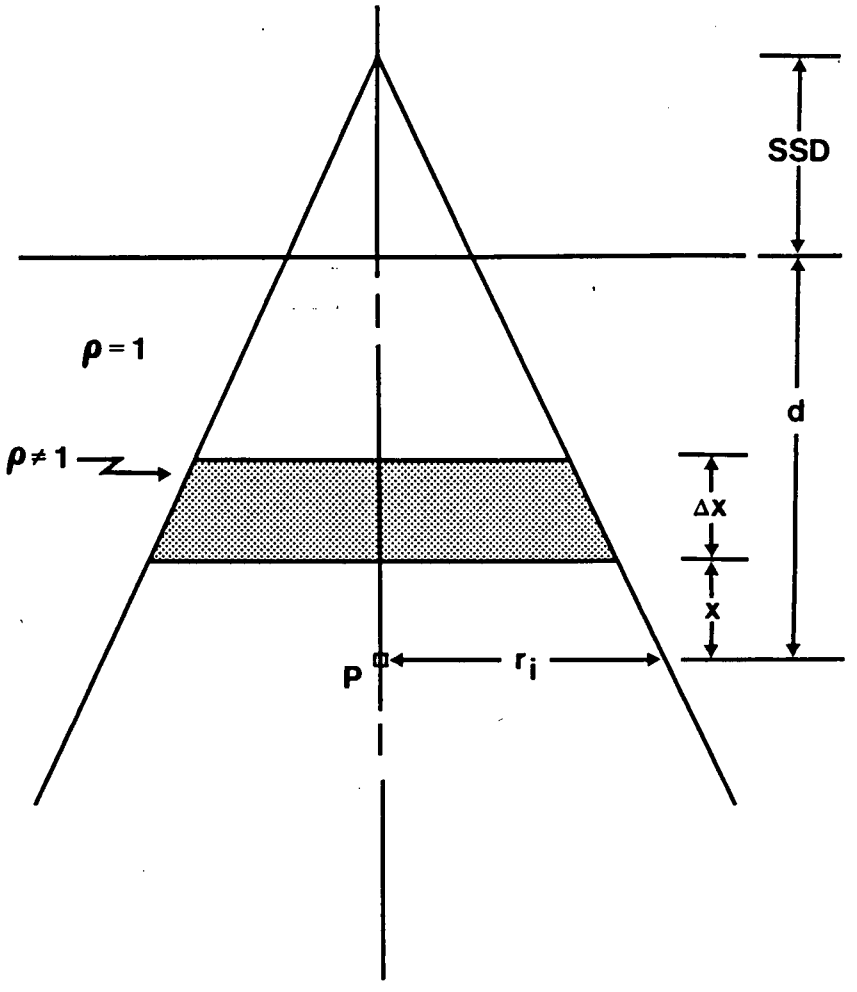

FIGURE B-1

SEMI-INFINITE SLAB INHOMOGENEITY OF WIDTH r_i

$$\Delta D_{P1} = D_{IP1} - D_{HP1}$$
$$= TAR\ (d,r_i)\ \ (CF\ (r_i) - 1)$$
$$= TAR\ (d,r_i)\ \ \Delta CF\ (r_i) \qquad (B3)$$

where the quantity $\Delta CF\ (r_i)$ has been defined. The change in the primary dose due to the slab, ΔD_{P0}, is given by equation (B3) for $r_i = 0$. The critical point to note is that $\Delta D_{P0} \neq \Delta D_{P1}$ as ΔD_{P0} does not include the slab's effect upon the scatter, which is implicitly contained within equation (B3). Thus, the difference between ΔD_{P0} and ΔD_{P1} will be the change in the scatter,

$$\delta(r_i) = TAR\ (d,r_i)\ \Delta CF\ (r_i) - TAR\ (d,0)\ \Delta CF\ (0) \qquad (B4)$$

Now, let the field size increase from r_i to r_o, as in figure (B-2). The change in scatter for this geometry is,

$$\delta(r_o) = TAR\ (d,r_o)\ \Delta CF\ (r_o) - TAR\ (d,0)\ \Delta CF\ (0) \qquad (B5)$$

The difference between equations (B4) and (B5) should yield the scatter change due to an annulus between r_i and r_o,

$$\delta_1(r_i,r_o) = \delta(r_o) - \delta(r_i)$$
$$= TAR\ (d,r_o)\ \Delta CF\ (r_o) - TAR\ (d,r_i)\ \Delta CF\ (r_i) \qquad (B6)$$

This equation is the first calculation type of the differential Batho

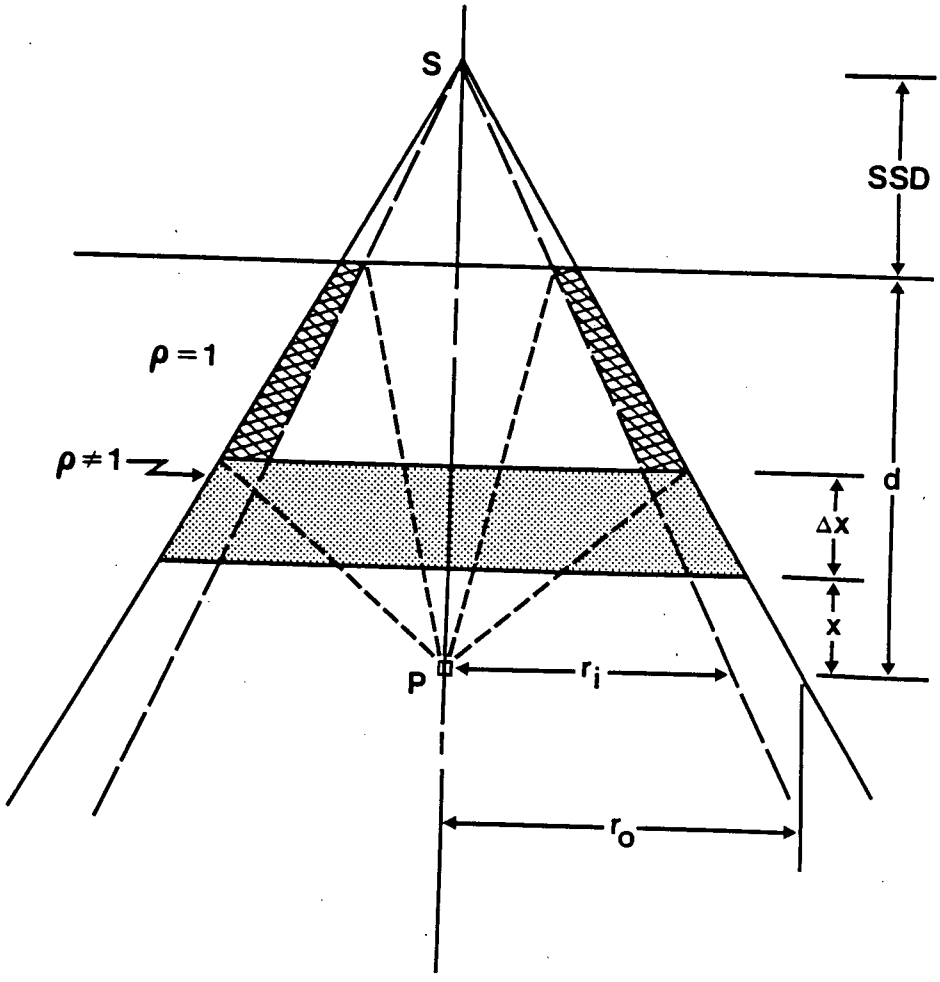

FIGURE B-2

SEMI-INFINITE SLAB INHOMOGENEITY OF WIDTH r_o

method, referred to as dBM(1). By taking this difference, all of the effects common to both geometries are subtracted out. However, equation (B6) also includes the scatter arising from the regions above the annulus which is filtered by the slab. These regions are cross-hatched in figure (B-2) and are irradiated only when the field radius is greater than r_i and, hence, are not subtracted out. To exclude this filtration effect, consider the situation where all of the water above the annulus has been removed, as in figure (B-3).

The scatter from above the annulus is zero. The primary at P has increased by the ratio, TAR $(x + \Delta x, 0)$ / TAR $(d, 0)$. The scatter change due to the annulus, strictly for this geometry, is,

$$\text{TAR}\ (x + \Delta x,\ r_o)\ \Delta\text{CF}\ (r_o) \ -\ \text{TAR}\ (x + \Delta x,\ r_i)\ \Delta\text{CF}\ (r_i)$$

But this result needs to be divided by the ratio of the primaries in order to obtain the proper scatter change,

$$\delta_2(r_i, r_o) = R\ [\ \text{TAR}\ (x + \Delta x,\ r_o)\ \Delta\text{CF}(r_o) - \text{TAR}\ (x + \Delta x,\ r_i)\ \Delta\text{CF}(r_i)\ ] \qquad \text{(B7)}$$

This is the second calculation type of the differential Batho method, dBM(2), and excludes the filtration effect.

The calculation types are dependent upon the geometry. The differential Batho method assumes that the annulus is coincident with the field boundaries. If the annulus is at the surface, the dBM(1)

and dBM(2) calculations are equal. At greater depths, with the annulus still coincident with the field, it is not possible to say which of dBM(1) and dBM(2) gives a better answer. However, for small field sizes, the amount of the cross-hatched regions in figure (B-2) is reduced. Consequently, we could expect dBM(2) to be a better representation as there is little filtration. As the field size increases, the filtration increases. This leads us to predict the dBM(1) result to be better. Thus, there should be a transition from the dBM(2) result to the dBM(1) as the field size increases.

Now consider the case of two annuli, one concentric about the other and of the same density, combining to form a single annulus. The inner annulus varies from r_1 to r_2 and the outer one from r_2 to r_3. The scatter change due to the inner annulus is given by,

$$\delta_1(r_1,r_2) = TAR\ (d,r_2)\ \Delta CF\ (r_2) - TAR\ (d,r_1)\ \Delta CF\ (r_1) \quad (B8)$$

The scatter change due to the outer annulus is,

$$\delta_1(r_2,r_3) = TAR\ (d,r_3)\ \Delta CF\ (r_3) - TAR\ (d,r_2)\ \Delta CF\ (r_2) \quad (B9)$$

The scatter change due to both annuli coalesced into one between r_1 and r_3 is,

$$\delta_1(r_1,r_3) = TAR\ (d,r_3)\ \Delta CF\ (r_3) - TAR\ (d,r_1)\ \Delta CF\ (r_1) \quad (B10)$$

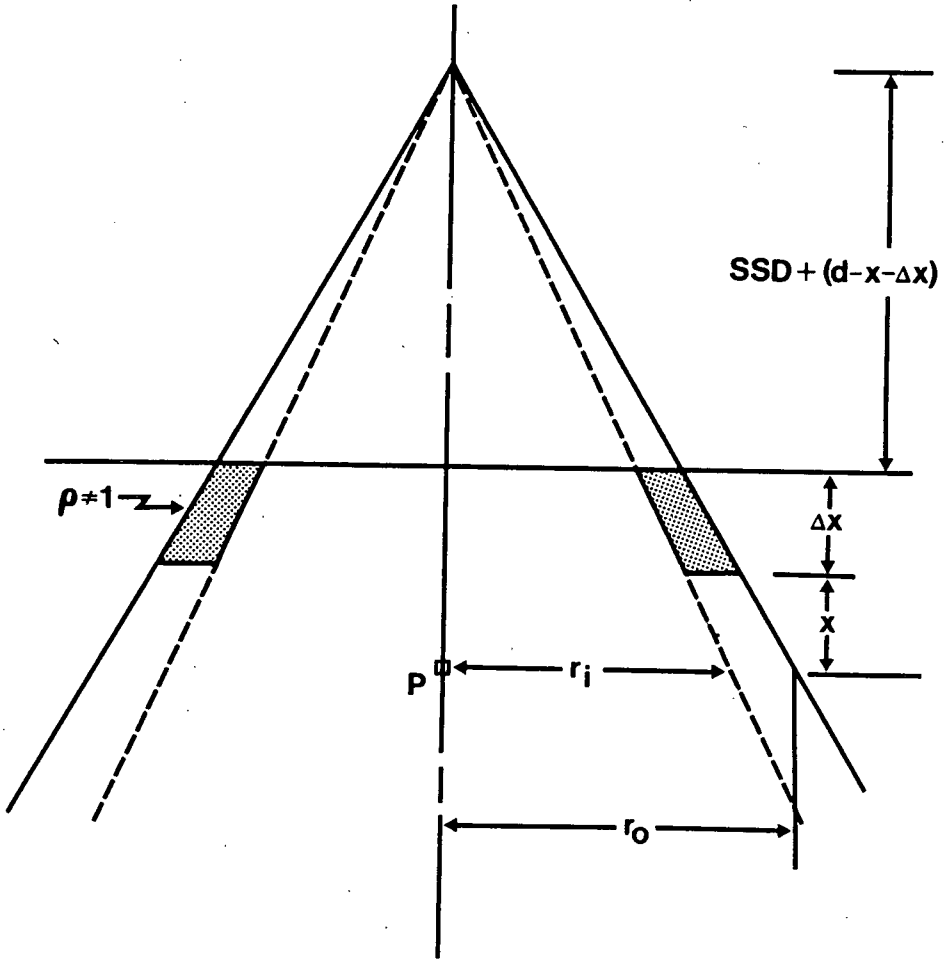

FIGURE B-3

ANNULAR INHOMOGENEITY AT PHANTOM SURFACE

From these equations, it is obvious that,

$$\delta_1(r_1,r_3) = \delta_1(r_1,r_2) + \delta_1(r_2,r_3) \qquad \text{(B11)}$$

That is, the scatter perturbations due to two radially varying annuli can be summed to give the perturbation of a single annulus composed of the two. The same result would also hold for the dBM(2) calculation.

APPENDIX C SCATTER PERTURBATIONS DUE TO CONICAL INHOMOGENEITIES

C.1 Thin cone approximation

Consider a thin inhomogeneous cone, of density ρ, extending from the surface of a unit-density phantom to infinity, and coincident with a fan line from the source, as in figure (C-1). The scatter arising from the segment dA and reaching the point 'P' on the central axis is,

$$dS_I = k \rho P_o e^{-\mu\rho x} \Phi(x,z) \, r \, dx \, d\phi \qquad (C1)$$

where $dA = r \, dx \, d\phi$, k is a constant, P_o is the primary at the surface, $P_o e^{-\mu\rho x}$ is the primary at dA and $\Phi(x,z)$ is a function describing the generation of, and the medium's effect upon, scatter. r is the distance from the source to dA, ϕ is the azimuthal angle and dx is the length of the element. Geometrically,

$$r = x + (R_F^2 + SSD^2)^{\frac{1}{2}}$$

so equation (C1) can be rewritten as,

$$dS_I = k \rho P_o e^{-\mu\rho x} \Phi(x,z) (R_F^2 + SSD^2)^{\frac{1}{2}} (1 + x \cdot (R_F^2 + SSD^2)^{-\frac{1}{2}}) \, dx \, d\phi \qquad -- (C2)$$

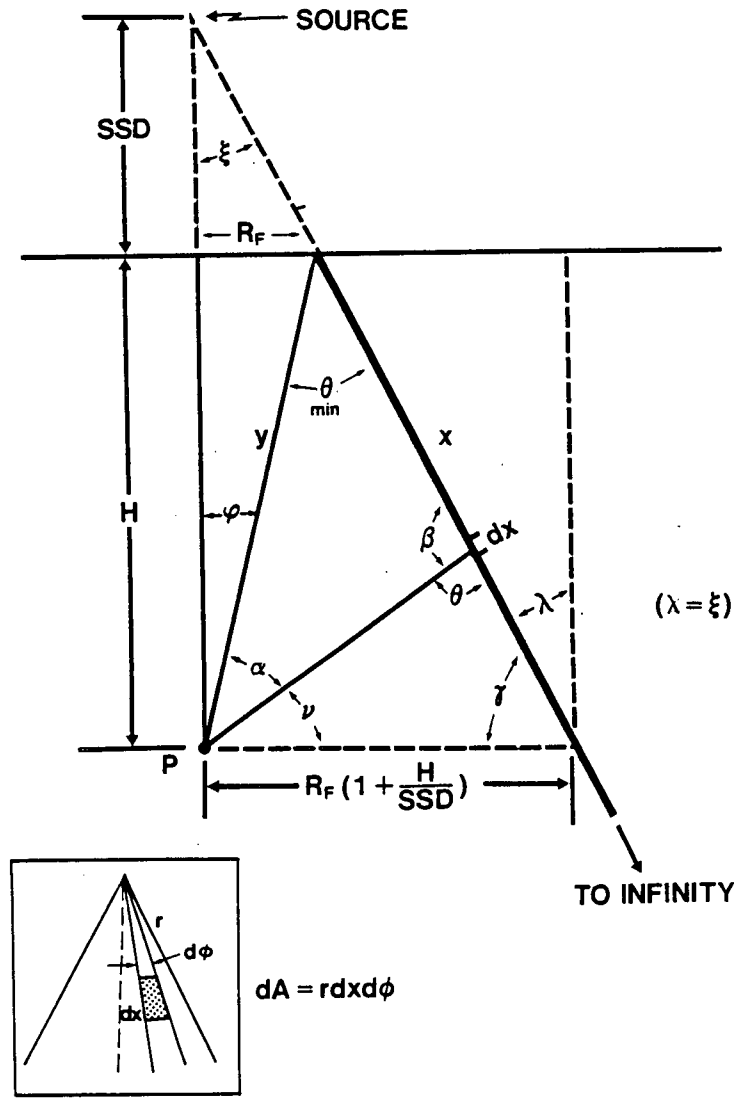

FIGURE C-1

CROSS SECTION OF A THIN CONICAL INHOMOGENEITY

Integrating the scatter from the cone reaching 'P',

$$S_I = k\,\rho\,P_o\,(R_F^2 + SSD^2)^{\frac{1}{2}} \int_{\phi=0}^{2\pi} \int_{x=0}^{\infty} e^{-\mu\rho x}\,\Phi(x,z)\cdot (1 + x\cdot(R_F^2 + SSD^2)^{-\frac{1}{2}})\,dx\,d\phi$$

$$= 2\pi k\,\rho\,P_o\,(R_F^2 + SSD^2)^{\frac{1}{2}} \int_{x=0}^{\infty} e^{-\mu\rho x}\,\Phi(x,z)\,(1 + x\cdot(R_F^2 + SSD^2)^{-\frac{1}{2}})\,dx \quad -- \quad (C3)$$

It would be convenient to integrate over the scattering angle θ rather than x. θ will vary from a minimum value (θ_{min}) to π as x goes from zero to infinity. Geometrically,

$$\begin{aligned}
\theta_{min} &= \pi - (\alpha + \nu) - \gamma \\
&= \pi - ((\pi/2) - \vartheta) - ((\pi/2) - \xi) \\
&= \vartheta + \xi \\
&= \tan^{-1}(R_F / H) + \tan^{-1}(R_F / SSD) \\
&= \tan^{-1}[\,R_F\cdot(H + SSD) / (H\cdot SSD - R_F^2)\,] \qquad (C4)
\end{aligned}$$

$x(\theta)$ can be found using the law of sines,

$$x = y \cdot \frac{\sin\alpha}{\sin\beta}$$

where $y = (R_F^2 + H^2)^{\frac{1}{2}}$, $\beta = \pi - \theta$, and $\alpha = \theta - \theta_{min}$. Then,

$$\begin{aligned}
x &= (R_F^2 + H^2)^{\frac{1}{2}} \cdot [\,\sin(\theta - \theta_{min}) / \sin(\pi - \theta)\,] \\
&= (R_F^2 + H^2)^{\frac{1}{2}} \cdot [\,\cos\theta_{min} - \cot\theta \cdot \sin\theta_{min}\,] \\
&= (R_F^2 + H^2)^{\frac{1}{2}} \cdot F(\theta) \qquad (C5a)
\end{aligned}$$

Differentiating,

$$dx = (R_F^2 + H^2)^{\frac{1}{2}} \cdot \sin \theta_{min} \cdot \csc^2 \theta \, d\theta \qquad (C5b)$$

Exchanging variables, equation (C3) becomes,

$$S_I = 2\pi k \rho P_o \sin \theta_{min} [(R_F^2 + SSD^2) \cdot (R_F^2 + H^2)]^{\frac{1}{2}} \cdot \int_{\theta min}^{\pi} \exp[-\mu\rho \cdot (R_F^2 + H^2) \cdot F(\theta)] \, G(\theta) \, \Phi(\theta) \csc^2 \theta \, d\theta \qquad (C6)$$

where,

$$G(\theta) = 1 + [(R_F^2 + H^2) / (R_F^2 + SSD^2)]^{\frac{1}{2}} \cdot F(\theta)$$

The scatter arising from the same cone in the homogeneous phantom, S_H, is given by equation (C6) for $\rho = 1$. Then the change in scatter due to the inhomogeneous cone is,

$$\Delta S = S_I - S_H$$
$$= 2\pi k P_o [(R_F^2 + SSD^2) \cdot (R_F^2 + H^2)]^{\frac{1}{2}} \cdot \int_{\theta min}^{\pi} (\rho \exp(-\mu\rho \cdot (R_F^2 + H^2) \cdot F(\theta)) - \exp(-\mu \cdot (R_F^2 + H^2) \cdot F(\theta)) \cdot \Phi(\theta) \, G(\theta) \csc^2 \theta \, d\theta \quad -- \quad (C7)$$

It is impossible to solve this integral as $\Phi(\theta)$ is an unknown function. However, it is possible to determine points along the axis where the

scatter change is zero. Neglecting the case of $\Phi(\theta) = 0$, the scatter change is zero for,

$$G(\theta) = 0 \tag{C8a}$$

$$\rho \exp(-\mu\rho\ (R_F^2 + H^2)^{\frac{1}{2}} \cdot F(\theta)) = \exp(-\mu \cdot (R_F^2 + H^2)^{\frac{1}{2}} \cdot F(\theta)) \tag{C8b}$$

From equation (C8a), we can solve for cot θ,

$$[(R_F^2 + H^2)/(R_F^2 + SSD^2)]^{\frac{1}{2}} \cdot (\cos\theta_{min} - \cot\theta \cdot \sin\theta_{min}) = -1$$

$$\cot\theta = \cot\theta_{min} + \csc_{\theta min} \cdot [(R_F^2 + SSD^2)/(R_F^2 + H^2)]^{\frac{1}{2}} \tag{C9}$$

A non-trivial solution (i.e., $\rho \neq 1$) for (C8b) is found from,

$$\ln\rho - \mu\rho \cdot (R_F^2 + H^2)^{\frac{1}{2}} \cdot F(\theta) = -\mu \cdot (R_F^2 + H^2)^{\frac{1}{2}} \cdot F(\theta)$$

Solving for cot θ,

$$\cot\theta = \cot\theta_{min} + (\ln\rho) \cdot [\mu \cdot (1-\rho) \cdot \sin\theta_{min} \cdot (R_F^2 + H^2)^{\frac{1}{2}}]^{-1} \tag{C10}$$

Both equations (C9) and (C10) should be reduced further. To do so, one must find an explicit equation relating H and θ. Consider the triangle formed from the angles β, ξ and $(\alpha + \vartheta)$. From the law of sines,

$$x + (R_F^2 + SSD^2)^{\frac{1}{2}} = (SSD + H) \cdot \frac{\sin(\alpha + \vartheta)}{\sin\beta}$$

and using $\beta = \pi - \theta$ and $(\alpha + \delta) = (\theta - \xi)$,

$$x = (SSD + H) \cdot (\cos \xi - \cot \theta \cdot \sin \theta) - (R_F^2 + SSD^2)^{\frac{1}{2}} \qquad (C11)$$

Substituting (C5a) into (C11) and solving for cot θ,

$$\cot \theta = \frac{A}{B} \qquad (C12)$$

where,

$$A = \cos \xi \cdot (SSD + H) - \cos \theta_{min} \cdot (R_F^2 + H^2)^{\frac{1}{2}} - (R_F^2 + SSD^2)^{\frac{1}{2}}$$
$$B = \sin \xi \cdot (SSD + H) - \sin \theta_{min} \cdot (R_F^2 + H^2)^{\frac{1}{2}}$$

Equating equation (C12) to (C9) and (C10) yields two transcendental equations for the depth of the zero-crossing, H. Both must be solved numerically or graphically to determine the solutions. However, as the maximum angle is π, there can only be two points where the scatter change is zero.

C.2 Modification of an extension of the Batho method to correct for a finite conical inhomogeneity

Consider figure (C-2). For this geometry, van de Geijn and PoCheng [1980] have extended the Batho correction factor to account for such an inhomogeneity,

$$CF_{VP} = 1 - R\,(1 - [TAR\,(x + \Delta x, r_i) / TAR\,(x, r_i)]^{\rho - 1}] \qquad (C13)$$

where,

$$R = TAR\,(d, r_i) / TAR\,(d, r_o)$$

We can extend this idea to correct for a thick cone of density ρ with an inner core of water. By scaling the densities and dimensions, as by O'Connor [1957], we obtain figure (C-3), which is merely an extension of figure (C-2). The correction factor for such a cone will be,

$$CF_{VP} = 1 - [(TAR\,(\rho d, \rho r_i) / TAR\,(\rho d, \rho r_o)]\,[1 - \beta^{\alpha}]$$

where

$$\beta = TAR\,(\rho d, \rho r_i) / TAR\,(0.5\ cm, \rho r_i)$$

$$\alpha = (1/\rho) - 1$$

This correction factor is inexact in that it neglects the contributions from below 0.5 cm above the point.

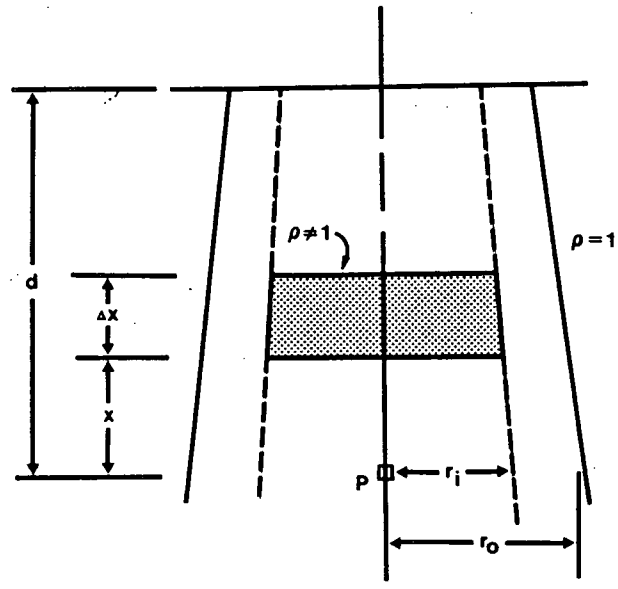

FIGURE C-2

SLAB INHOMOGENEITY COVERING PART OF THE FIELD

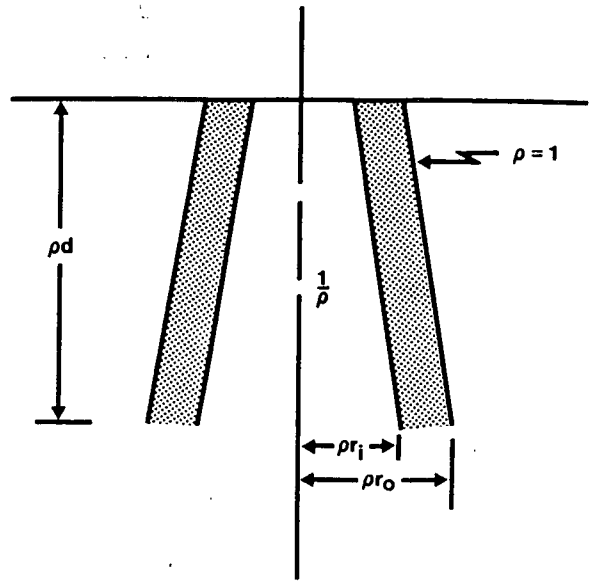

FIGURE C-3

UNIT-DENSITY CONICAL INHOMOGENEITY IN A NON-UNIT DENSITY MEDIUM